2014-07-02

Towards Stronger Coulomb Coupling in an Ultracold Neutral Plasma

Mary Elizabeth Lyon
Brigham Young University - Provo

Towards Stronger Coulomb Coupling in an Ultracold Neutral Plasma

Mary E. Lyon

A dissertation submitted to the faculty of
Brigham Young University
in partial fulfillment of the requirements for the degree of

Doctor of Philosophy

Scott D. Bergeson, Chair
Justin B. Peatross
Ross L. Spencer
Jean-Francois S. Van Huele
Michael J. Ware

Department of Physics and Astronomy

Brigham Young University

July 2014

ABSTRACT

Towards Stronger Coulomb Coupling in an Ultracold Neutral Plasma

Mary E. Lyon
Department of Physics and Astronomy, BYU
Doctor of Philosophy

Ultracold neutral plasmas are created by photoionizing laser-cooled atoms in a magneto-optical trap (MOT). Due to their large electrical potential energies and comparatively small kinetic energies, ultracold plasmas fall into a regime of plasma systems which are called "strongly coupled." A priority in the field of ultracold plasmas is to generate plasmas with higher values of the strong coupling parameter Γ, which is given as the ratio of the nearest-neighbor Coulomb potential energy to the average kinetic energy. The equilibrium strong coupling in ultracold plasmas is limited by the ultrafast relaxation of the ions due to spatial disorder in the initial system. This heating mechanism is called "disorder-induced heating" (DIH) and it limits the ion strong coupling in ultracold plasmas to order unity. This thesis describes experiments that explore ways to generate higher values of the strong coupling parameter in an ultracold neutral calcium plasma.

One way to increase Γ is to mitigate the effects of DIH using electron screening. This thesis describes an experiment in which the initial electron temperature was systematically changed to determine the effect that electron screening has on the ion thermalization. At lower initial electron temperatures, corresponding to a higher degree of electron shielding, it was found that the screening slows the ion thermalization and reduces the equilibrium ion temperature by as much as a factor of two. However, electron screening also reduces the ion interaction strength by the same amount, which has the net effect of leaving the effective Γ unchanged.

Another method for increasing the strong coupling of an ultracold plasma is to excite the plasma ions to a higher ionization state. Simulations predict that doubly ionizing the plasma ions can increase the strong coupling in an ultracold plasma by as much as a factor of 4, with the maximum value of Γ depending on the timing of the second ionization relative to the DIH process. This thesis describes an experiment designed to test these predictions in a Ca^{2+} plasma. Measurements of the change in the Ca^{+} ion temperature as a function of the timing of the second ionization pulses were made using laser-induced fluorescence. Results of these measurements show that the heating of the Ca^{+} ions due to the second ionization depends on the timing of the second ionization pulses, as predicted by MD simulations.

Keywords: ultracold plasma, atomic physics, plasma physics, laser cooling, strong coupling

ACKNOWLEDGMENTS

In my tenure as a student I have had many wonderful teachers and mentors, but none as influential as my graduate advisor, Dr. Scott Bergeson. He is a talented and knowledgeable scientist and has been an exceptional advisor, teacher, and mentor. His support and encouragement have made all the difference.

My gratitude extends to the entire BYU Physics and Astronomy Department, which includes the faculty, staff, and students. Though they are too numerous to mention by name, I hope they know how much I value them and all that they have done for me.

I express my love and thanks to my wonderful family and friends, who have been my rock and my support. In particular I want to acknowledge and thank my parents, for their constant and consistent love and support, for encouraging me to always ask questions, and for never letting me settle for anything less than my best.

I would be remiss if I did not acknowledge the funding support for this research, which has come from the National Science Foundation, the Air Force Office of Scientific Research, and the Rocky Mountain NASA Space Grant Consortium.

Renowned chemist Henry Eyring once wrote, “The universe is coordinated and regulated by influences that transcend the laws of physics now known ... [God is] running this thing. I know that because of how magnificently it runs.” Though my own understanding of the universe is so very limited compared to His, I am grateful that He lets me tinker.

Contents

List of Figures

Chapter 1

Introduction

Plasmas comprise the vast majority of the known universe and exist over a wide range of temperatures and densities. Most plasmas form from energetic collisions between particles in a hot gas which result in the liberation of one or more electrons. The ions and electrons in a plasma exhibit collective behavior, which gives rise to a wide range of interesting plasma phenomenon. The study of plasmas and plasma dynamics is an expansive field and is continually growing.

Plasmas are typically defined as being quasineutral, which means that the number of electrons is approximately equal to the number of positive ions, although non-neutral plasmas can be created and studied in laboratory settings [1, 2]. Plasmas differ from neutral gases, however, in important and distinct ways. The unbound charged particles in a plasma interact with each other and with external electric and magnetic fields through the Coulomb force. This gives rise to an important plasma parameter, called the plasma frequency, which is given as

$$\omega_{p\alpha} = \sqrt{\frac{ne^2}{m_\alpha \varepsilon_0}}, \tag{1.1}$$

where n is the plasma density, e is the fundamental charge, ε_0 is the permittivity of free space, and m_α is the electron or ion mass. Many important plasma processes occur on the time scale of the inverse plasma frequency. It is important to note that the plasma frequency for electrons

and ions is different, due to the difference between their masses. This means that, in many cases, the electron and ion systems equilibrate independently of each other. In talking about the plasma temperature, it is therefore necessary to differentiate between the electron temperature T_e and the ion temperature T_i, which in some cases can differ by orders of magnitude. It is most common in traditional plasma physics to see the plasma temperature and frequency defined as T_e and ω_{pe}. The electron temperature is usually given in Kelvin or eV and typically ranges from 1 eV to 10^4 eV (10^4 K to 10^8 K). The plasma frequency, which depends on the plasma density, can range from approximately 1×10^4 s^{-1} for interstellar gases ($n \sim 1\text{cm}^{-3}$) to 1×10^{14} s^{-1} for laser produced plasmas ($n \sim 10^{20}\text{cm}^{-3}$) [3].

The extremely high temperatures and densities of many high energy-density plasmas make it difficult to study the dynamics of these plasmas directly. Their high densities, which correspond to high plasma frequencies, mean that many important interactions happen too quickly for current diagnostic techniques to measure and those that can be measured require optical detection in the x-ray range. In 1998 a group of researchers at NIST in Maryland produced the first ultracold neutral plasma by photoionizing a gas of xenon atoms in a magneto-optical trap (MOT) [4]. This development was the birth of a new field, one which spanned both atomic and plasma physics. The controllable initial conditions and comparatively low densities of ultracold plasma make them ideal systems for conducting detailed studies of a variety of plasma dynamics, which has included non-equilibrium phenomena [5–10], three-body recombination [11–13], plasma wave phenomena [14, 15], expansion dynamics [16–18], collective behavior [19, 20], the testing of kinetic and hydrodynamic theories [21–23], and many other interesting studies.

Perhaps the most interesting property of ultracold plasmas is the unique position they occupy in phase space. At sufficiently high densities plasmas can become "strongly coupled." This is the case for certain astrophysical systems, such as the interior of some Jovian planets and white dwarf stars, and the outer crust of neutron stars [24, 25]. Strong coupling is also a property of a

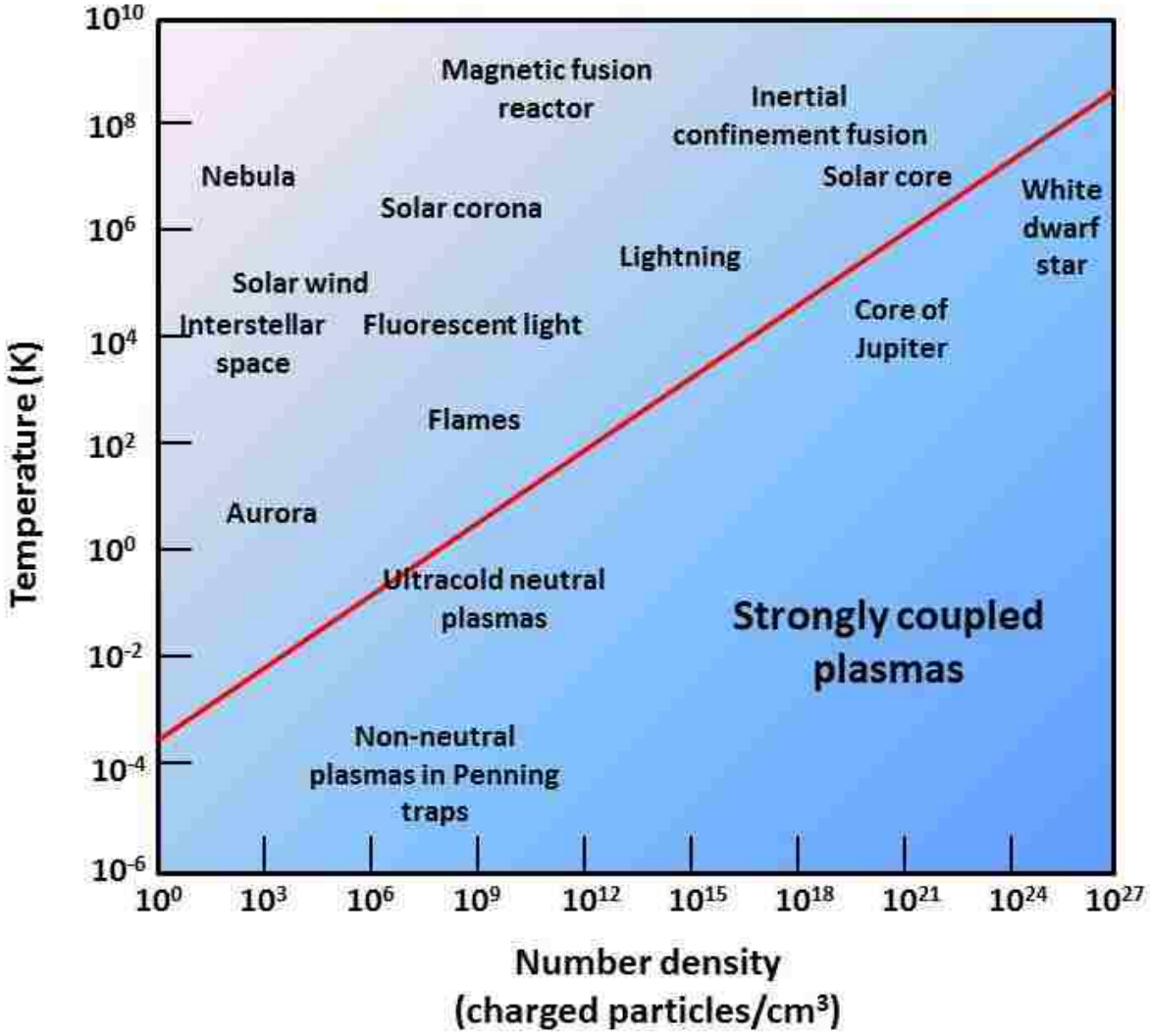

Figure 1.1 Naturally occurring and man-made plasmas plotted as a function of their temperature and density. The red line marks $\Gamma = 1$ and the boundary between weak and strong coupling. Ultracold plasmas are plotted in the low temperature, low density strongly coupled regime. The complete thermodynamic state of a system is described by the dimensionless coupling parameter Γ, which means that plasmas that fall on the same constant Γ line will share many of the same properties.

number of man-made systems, such as high density laser-produced plasmas and laser-driven fusion plasmas [26]. However it is not only at extremely high densities that plasmas can become strongly coupled, but also at very low temperatures, as in the case of ultracold neutral plasmas.

The goal of the research presented in this thesis is to study the dynamics of strongly coupled neutral systems using ultracold neutral plasmas. However, we are limited in this pursuit by a process called "disorder-induced heating" (DIH), which limits the value of the dimensionless coupling constant Γ to order unity [6, 27]. The work presented here has the primary objectives of better understanding the DIH process, mitigating its effects through electron shielding, and increasing Γ by promoting the plasma ions to the second ionization state. Chapter 1 provides motivation for this work as well as background on strongly coupled and non-ideal plasmas and specific plasma processes. Chapter 2 describes the general experimental apparatus and techniques. To improve our measurements, the data acquisition, and overall stability of the experiment, we implemented an optical frequency comb, which is characterized in Chapter 3. Since DIH is the most significant hurdle in achieving higher-Γ ultracold plasmas, Chapter 4 is a detailed characterization of DIH in terms of density and electron temperature. It also includes a discussion of an experiment designed to mitigate the effects of DIH through electron shielding and the results of that experiment. Finally, Chapter 5 describes an experiment in which the plasma ions were doubly ionized to increase the strong coupling in our ultracold plasmas.

1.1 Strongly coupled and non-ideal plasmas

The thermodynamic properties of strongly coupled plasmas depend only on the dimensionless parameter Γ [25]. This parameter, called the strong coupling parameter, is given by the ratio of the nearest-neighbor Coulomb potential energy to the average kinetic energy of the ions

$$\Gamma = \frac{Z^2 e^2}{4\pi\varepsilon_0 a_{ws}} \frac{1}{k_B T_i}, \tag{1.2}$$

where $a_{ws} \equiv (3/4\pi n)^{1/3}$ is the Wigner-Seitz radius or the average distance between ions, k_B is Boltzman's constant, and T_i is the ion temperature.

Strongly coupled plasmas are considered to be non-ideal plasmas and therefore are not well described by traditional plasma physics. Non-ideal plasmas are characterized as having a Debye length comparable to the Wigner-Seitz radius. The Debye length is given by

$$\lambda_D = \sqrt{\frac{\varepsilon_0 k_B T_e}{n e^2}}, \tag{1.3}$$

where T_e is the electron temperature. Another important plasma parameter is the classical distance of closest approach, given by

$$b = \frac{e^2}{4\pi\varepsilon_0} \frac{1}{k_B T_i}. \tag{1.4}$$

For $\Gamma = 1$, the interparticle spacing is equal to the classical distance of closest approach, which marks the onset of many-body interactions. At values of $\Gamma \geq 1$ plasmas start exhibiting correlation effects as nearest-neighbor interactions begin to dominate over the random thermal motion. As Γ increases, plasmas can exhibit liquid-like and eventually crystalline behavior [28]. This structural order, which plays a significant role in the plasma dynamics, is completely neglected by traditional plasma models. A kinetic or hydrodynamic treatment of the plasma, for example, relies on the dominance of weak, long-range interactions to describe the plasma dynamics and ignores correlation effects altogether.

1.2 Fusion and non-neutral plasmas

Studying the effects of strong coupling is of particular importance in high energy-density physics and fusion research. In dense, high temperature fusion plasmas, Salpeter predicted that the thermonuclear fusion rate is exponentially enhanced by strong coupling [29, 30]. This exponential enhancement of the thermonuclear fusion rate is a consequence of the correlations found in strongly coupled plasmas. In effect, the correlations between neighboring ions screen the repulsive Coulomb interaction between colliding ions, allowing ions of a given temperature to get closer before being repelled. This softening of the nearest-neighbor potential energy reduces the Coulomb barrier width, thus increasing the probability of close collisions due to tunneling.

Studies conducted at NIST-Boulder and UCSD discovered an analogous enhancement effect in magnetized strongly correlated non-neutral plasmas [31, 32]. The non-neutral plasmas studied at NIST fall into the strongly magnetized regime, which means that $\Omega_c \tau \geq 1$, where Ω_c is the cyclotron frequency and τ is the duration of a small impact parameter collision [32]. In strongly magnetized plasmas the kinetic energy of the cyclotron motion is an adiabatic invariant, and energy is exchanged between the perpendicular and parallel motion only through rare collisions that break this invariance [33]. This exchange of energy through close collisions in a strongly magnetized, cryogenic plasma is analogous to the energy released in nuclear reactions due to rare collisions. This is because the thermonuclear fusion rate in a fusion plasma and the equipartition rate in a strongly magnetized plasma are both dominated by close collisions. Therefore the exponential enhancement predicted by Salpeter for fusion plasmas also applies in the case of strongly magnetized, strongly correlated non-neutral plasmas [34]. The group at UCSD observed that there is a strong screening regime in a strongly magnetized non-neutral plasma in which the equipartition rate is enhanced by the same factor of e^{Γ} that Salpeter predicted for fusion plasmas [32].

Since the thermodynamic properties of strongly coupled plasmas depend only on Γ, it is believed that cryogenic, non-neutral plasmas can be used to model the behavior of fusion-class plas-

mas. This makes it possible to study the fundamental behavior of strongly coupled systems as manifested in high energy-density plasmas using a low energy table-top apparatus. The question can then be raised of whether ultracold *neutral* plasmas can be used to model high energy-density plasmas. The long-term goal of the research described in this thesis is to measure a Γ-dependent process in ultracold neutral plasmas that is analogous to the exponential rate enhancements predicted for fusion plasmas and observed in strongly correlated non-neutral plasmas.

1.3 Ultracold plasma characteristics and dynamics

Ultracold neutral plasmas are generated by photoionizing atoms in a magneto-optical trap (MOT) [4]. In our experiments, the initial temperature of the electrons is typically between 1-1000 K and the initial ion temperature is the few mK inherited from the trapped atoms. The densities of our plasmas are on the order of 10^{10} ions per cm^{-3}. The initial density profile of ultracold plasmas typically reflects the nearly Gaussian spatial density distribution of the trapped atoms in the MOT, which density is given by

$$n(r) = n_0 \exp[-r^2/2\sigma^2], \tag{1.5}$$

where r is the plasma radius and σ is the Gaussian width of the plasma.

After the atoms in the MOT are ionized, the resulting plasma is not confined. As the plasma expands, the density changes. The time-dependent density profile is given by

$$n(r,t) = n_0 \exp[-r^2/2\sigma^2(t)][\sigma_0/\sigma(t)]^3, \tag{1.6}$$

where n_0 is the peak density in the plasma, σ_0 is the initial plasma size, and $\sigma(t) = \sqrt{\sigma_0^2 + v_{\rm exp} t^2}$ is the Gaussian radius. The expansion velocity, $v_{\rm exp} \equiv \sqrt{k_B T_e/m_i}$, is the rate at which the plasma expands radially outward in a self-similar (Gaussian) manner and depends on the initial electron temperature. When the plasma is created, a few electrons have enough kinetic energy to overcome the Coulomb potential of the ions and escape. This creates a slight imbalance in the charge that

results in an attractive Coulomb potential that traps the remaining electrons. Electrons trying to escape the ion potential produce a "pressure" that drives the plasma expansion. The electrons cannot escape, however, and the plasma remains largely neutral. The neutrality of the plasma is given by the ratio of the number of free electrons to ions, which typically ranges from 90% to 99% in ultracold plasmas, and depends on the kinetic energy imparted to the electrons from the ionizing laser [4, 16, 20].

In neutral plasmas, electrons form a screening background for the ions. If the electron temperature is not too low, the ion interaction can be modeled with a Yukawa potential

$$u_{ii}^{Y} = \frac{e^2}{4\pi\varepsilon_0}\frac{e^{-r/\lambda_D}}{r}, \tag{1.7}$$

where λ_D is the Debye length given by Eq. 1.3. In plasma physics it is often convenient to conceptualize the influence of electron screening in terms of the Debye sphere, which is the volume $n\lambda_D^3$ for which particles are electrostatically influenced by all other particles within the volume. One definition for an ideal plasma is $n\lambda_D^3 \gg 1$, which means that the probability of finding many charges within the Debye sphere is large. At low electron temperatures, the number of particles per Debye sphere decreases and can reach the point where $n\lambda_D^3 \leq 1$. Using the Yukawa potential to describe interactions between ions in plasmas is not valid if we must take into consideration the strong, short-range interactions that become important when $n\lambda_D^3 \leq 1$ [22]. Electron screening can be parameterized using the inverse scaled screening length, $\kappa \equiv a_{ws}/\lambda_D$. The parameter κ exhibits a strong temperature dependence, $\kappa \sim T_e^{-1/2}$, and a weak density dependence $\kappa \sim n^{1/6}$.

1.3.1 Three-body recombination

Three-body recombination (TBR) is a collisional process that occurs in plasmas in which an electron and ion collide and recombine to form a Rydberg atom in the presence of another electron. Energy and momentum are conserved by the second electron, which carries away the energy, resulting in additional heating of the electron system. The TBR rate is found from the two-body

collision rate multiplied by the probability of the collision occurring in the presence of a third particle, given by

$$\gamma_{TBR} = (n\sigma v)(nb^3), \tag{1.8}$$

where n is the density, $\sigma = \pi b^2$ is the collision cross-section and b is the impact parameter given in Eq. 1.4, and v is the velocity. Since $b \sim T^{-1}$ and $v \sim T^{-1/2}$ the TBR rate depends strongly on the electron temperature $\gamma_{TBR} \sim T^{-9/2}$. At very early times and for low initial electron temperatures, TBR dominates the plasma dynamics. However, it also heats the electrons, which results in a slowing of the TBR rate as the electron system equilibrates ($\sim$10 ns).

Theoretical models predict that the TBR rate changes in a strongly coupled plasma [13]. Since $a_{ws} = b$ at the onset of strong coupling, the particles are essentially constantly "colliding," and the collisions must now be considered many-body collisions. The many-body nature of the process is expected to cause the TBR rate to deviate from the $T^{-9/2}$ scaling.

1.3.2 DIH and kinetic energy oscillations

One might suppose that at very early times the ion strong coupling parameter is large in ultracold plasmas, corresponding to typical initial ion temperatures on the order of 1 mK. However, ultracold plasma are created in a non-equilibrium state in which the velocity distribution of the ions is non-Maxwellian. Therefore the ion temperature T_i, and by extension the ion strong coupling, is not well defined. The equilibrium ion strong coupling is limited by the ultrafast relaxation of spatially uncorrelated ions to a more ordered state. This process is called "disorder-induced heating" because it converts the electrical potential energy that the ions have due to their disordered state into kinetic energy. DIH was predicted in Ref. [6] and is shown to increase the ion temperature to the correlation temperature T_c, which is given by

$$T_c = \frac{2}{3}\frac{e^2}{4\pi\varepsilon_0 a_{ws} k_B}\left|\frac{u}{\Gamma} + \frac{\kappa}{2}\right|, \tag{1.9}$$

where κ is the inverse scaled screening length and u is the temperature-scaled excess potential energy per particle. A detailed derivation of Eq. 1.9 is provided in Appendix A. If screening effects are small, the correlation temperature is determined by the density alone and can be written simply as

$$T_c = \frac{2}{3}\frac{e^2}{4\pi\varepsilon_0 a_{ws} k_B}. \tag{1.10}$$

The DIH process happens at early times in the plasma evolution, corresponding to time scales given by $\omega_{p\alpha}^{-1}$ (see Eq. 1.1). Both the electrons and the ions undergo DIH, but the much lower electron mass means that the electrons equilibrate within the first few nanoseconds after the plasma is created and are limited to coupling parameters of approximately $\Gamma_e \leq 0.2$ [35, 36]. In our plasmas, with densities on the order of 10^{10} cm^{-3}, DIH in the ions happens within the first 100 ns and limits the ion strong coupling to $\Gamma \approx 2$. The mass ratio of the electrons to the ions means that essentially no energy is exchanged between the electron and ion systems during their respective DIH phases. However, if the electron temperature is low enough and shielding effects cannot be neglected, electron screening modifies the ion equilibration by reducing the ion-ion interaction strength and slowing the DIH process.

Oscillations in the ion kinetic energy are a well-documented phenomenon [22]. When the plasma is created and the ion energy landscape is formed, each ion finds itself in a potential well defined by neighboring ions and electrons (see Fig. 1.2). Initially the ions move coherently within their respective potential wells, seeking to minimize their potential energy by moving down the wall of the well and increasing their kinetic energy. When they reach the lowest potential energy state, corresponding to the bottom of the well and the highest degree of spatial ordering, the ions overshoot their equilibrium positions and oscillate in their potential wells before settling at the bottom. Initially the ions all move in phase with respect to each other, and their coherent motion means that the kinetic energy oscillations can easily be seen in the data at early times, as shown in Fig. 1.3. The first oscillation in the kinetic energy occurs at $\omega_{pi}t \sim 1$. Oscillations at later

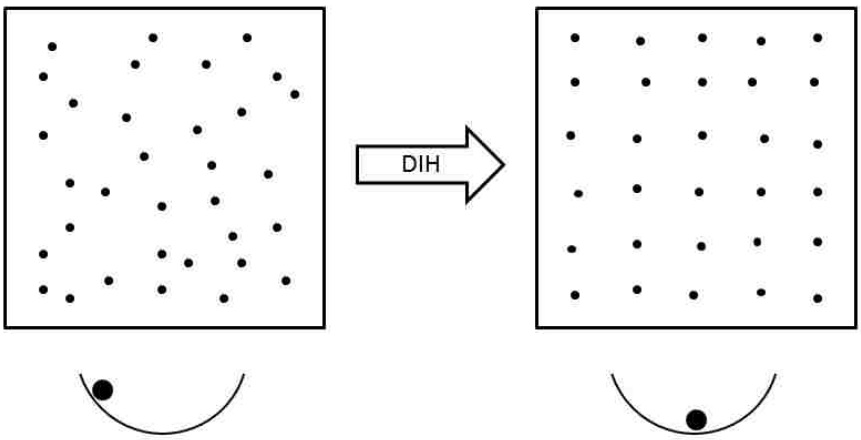

Figure 1.2 Cartoon depiction of the disorder-induced heating (DIH) process. Ultracold plasmas are formed by photoionizing laser-cooled atoms in a MOT. The neutral atoms in the MOT have a random spatial distribution, which gives rise to spatially uncorrelated ions. When the atoms are ionized, each of the ions finds itself in a potential well, defined by Coulomb interactions with neighboring charged particles. The ions move within this potential well from a disordered state (high potential energy) to a more ordered state (low potential energy), thus increasing their kinetic energy and heating the plasma ions.

times are difficult to see, however, due to variations in the density across the plasma which cause ω_{pi} to vary and results in the ion motion dephasing. The peak of the first kinetic energy oscillation is often referred to as the DIH peak and corresponds to the greatest spatial ordering of the plasma system.

1.3.3 Expansion

Laha *et al.* showed that the plasma expansion can be described by an exact solution to the Vlasov equations [18]. This expansion is self-similar and results in an adiabatic cooling of the electrons, because the electron kinetic energy is converted into the expansion energy of the plasma [28]. A more detailed treatment of the plasma expansion is given in Ref. [18], but the results are summarized here.

The velocity of the ions, as determined by the self-similar solution to the Vlasov equations, is

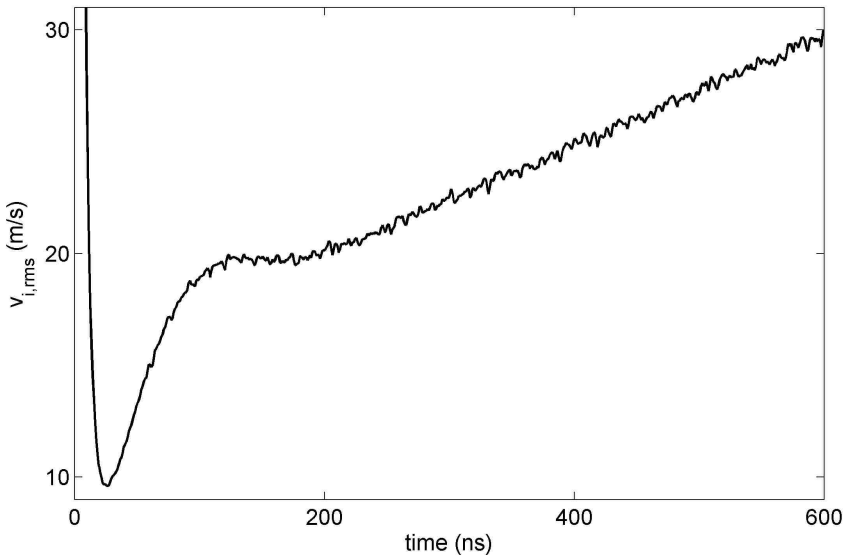

Figure 1.3 The rms velocity of the ions plotted as a function of time. The peak in the data that occurs between 100-200 ns is an oscillation in the kinetic energy, which arises from ions overshooting their equilibrium position as they move to minimize their electrical potential energy under the influence of DIH. This peak is also called the DIH peak.

given by

$$v_{i,\mathrm{rms}} = \sqrt{\frac{k_B}{m_i}\left\{\frac{t^2}{\tau_{\mathrm{exp}}^2}[T_e(t)+T_i(t)]+T_i(t)\right\}}, \tag{1.11}$$

where τ_{exp}, the characteristic expansion time, is given by $\tau_{\mathrm{exp}} = \sqrt{m_i\sigma(0)^2/k_B[T_e(0)+T_i(0)]}$ and the time evolving ion and electron temperatures are given by $T_\alpha(t) = T_\alpha(0)/(1+t^2/\tau_{\mathrm{exp}}^2)$, where the subscript $\alpha = i,e$. We can solve for the ion temperature $T_i(t)$ by rearranging Eq. 1.11

$$T_i(t) = \frac{m_i v_{i,\mathrm{rms}}^2}{k_B} - \frac{T_e(0)\frac{t^2}{\tau_{\mathrm{exp}}^2}}{1+\frac{t^2}{\tau_{\mathrm{exp}}^2}}. \tag{1.12}$$

The initial ion temperature is assumed to be negligible compared to the initial electron temperature. On the time scale of 200 - 1000 ns, the plasma has not expanded. By fitting our data to this expansion model we are able to extract the initial ion temperature and the ion temperature at later times. It is also possible to use this model to estimate the initial electron temperature T_e of the plasma, so long as T_e is not too low. This is useful for plasmas that evolve from cold Rydberg gases, for example, where the initial electron temperature is not well defined. At these small initial electron temperatures, the electron temperature extracted from the expansion model has been shown to overestimate the electron temperature at late times [37]. However, it is likely that the model is reasonably accurate at early times before the plasma has expanded.

Chapter 2

Experimental Techniques

2.1 Plasma formation

The process of plasma formation begins in a MOT, where approximately 10 million Ca atoms are laser-cooled and trapped. The trapped calcium is photoionized in a two-photon ionization process using ns-duration laser pulses. One of the advantages of using calcium, an alkaline-earth metal, is that it retains one valence electron after the first ionization. This allows us to use optical spectroscopy techniques to measure density and temperature. Additionally, the energy levels in calcium are favorable because the transitions required for trapping, ionization, and detection correspond to laser wavelengths that are readily attainable (see Fig. 2.1). A basic explanation of the processes of laser cooling and trapping, ionization, and plasma detection will be provided as well as details regarding our experimental apparatus.

2.1.1 Laser cooling and trapping

Atom trapping in a MOT uses a spatially varying magnetic field to produce a position-dependent restoring force via the Zeeman shift. A MOT consists of six orthogonal, counter-propagating

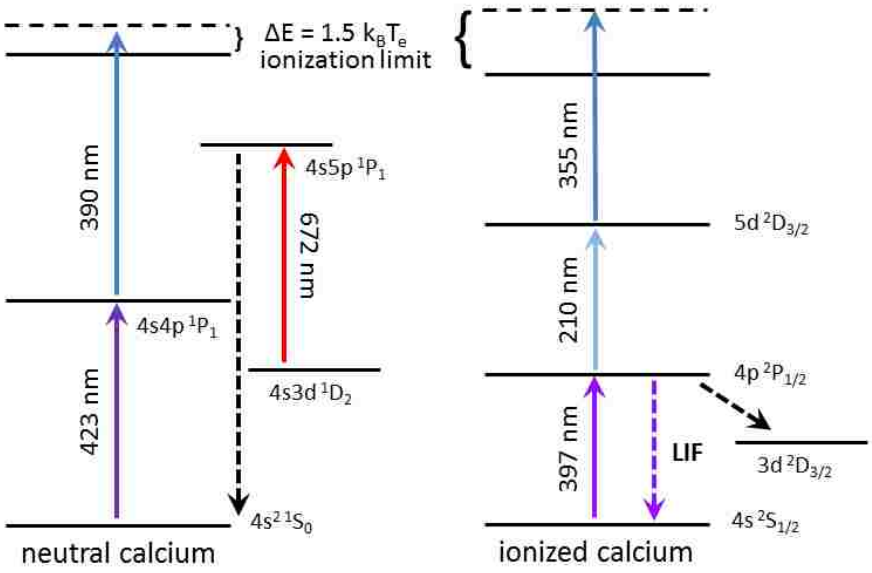

Figure 2.1 Partial energy level diagram for Ca (left) and Ca^+ (right). Atoms are cooled and trapped in the MOT using the 423 nm transition. A repump laser at 672 nm pumps atoms that fall into the metastable $4s3d\ ^1D_2$ state back to the ground state via the highly excited $4s5p\ ^1P_1$ state. The MOT atoms are ionized using a resonant two-step process at 423 and 390 nm. The electron temperature depends on the amount by which the 390 nm laser photon energy exceeds the ionization potential. Spectroscopy of the plasma ions uses the 397 nm resonance transition. Resonantly scattered photons are detected by a fast photomultiplier tube. The Ca^+ $^2P_{1/2}$ state ($\tau = 7.2$ ns) has a $\sim 7\%$ decay branch to the $^2D_{3/2}$ dark state.

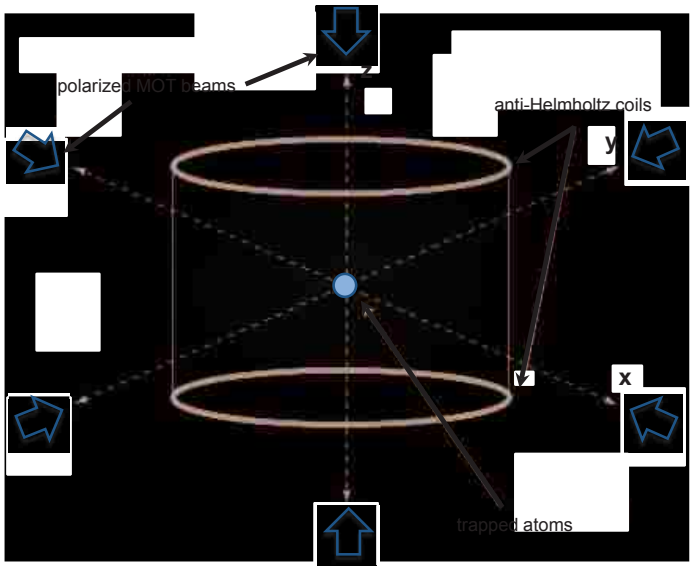

Figure 2.2 Magneto-optical trap (MOT). Six orthogonal beams, tuned to the $4s^2\ {}^1S_0 \rightarrow 4s4p\ {}^1P_1^{\mathrm{o}}$ transition in calcium at 423 nm, converge at a point at the center of the trap, where the magnetic field produced by the anti-Helmholtz coils is zero. The six beams provide a damping force in all three spatial directions.

beams that are slightly detuned below the atomic resonance frequency, as depicted in Fig. 2.2. In our experiment, the trapping laser is tuned below the $4s^2\ {}^1S_0 \rightarrow 4s4p\ {}^1P_1^{\mathrm{o}}$ transition in calcium at 423 nm by approximately 50 MHz. Atoms moving anti-parallel to the laser beam see the laser Doppler shifted into resonance. The absorption of photons causes the atoms to recoil, due to conservation of momentum, and effectively pushes the atoms back towards the center of the trap.

A pair of coils in an anti-Helmholtz configuration creates a quadrupole magnetic field that is zero at the trap's geometric center and increases linearly in magnitude in the region of the trap's center. The magnetic field Zeeman shifts the magnetic sublevels of the $4s4p\ {}^1P_1^{\mathrm{o}}$ state. Left and right circularly polarized light is used to regulate the absorption of photons via quantum mechanical selection rules (see Fig. 2.3). Our neutral calcium atom trap cools the atoms to about 1 mK and

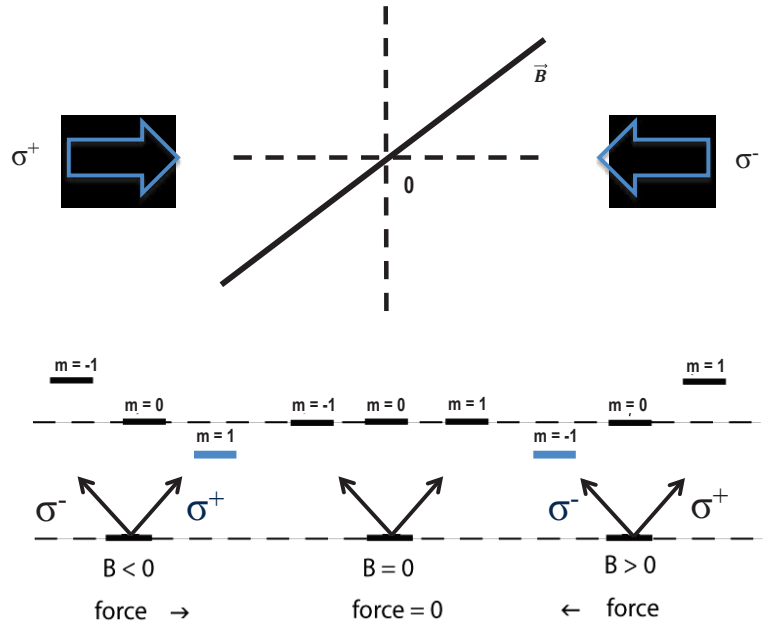

Figure 2.3 A one-dimensional representation of Zeeman shifting and quantum selection rules in a MOT for a two-level atom. To the right of the zero of the magnetic field the magnetic sublevels of the excited state are shifted so that the $m = -1$ state is on resonance with the laser beam. A transition from the ground state to the $m = -1$ excited state is induced by the left-circularly polarized photons impinging from the right. The opposite is true for atoms to the left, where the right-circularly polarized laser only excites atoms to the $m = +1$ state, which has been shifted by the magnetic field so that it is on resonance with the laser beam. Thus the photon scattering rates are regulated and the result is a position-dependent restoring force that pushes the atoms towards the center of the trap, where the magnetic field equals zero.

confines them to a roughly spherical region approximately 0.3 mm in diameter.

The calcium atoms are produced by a temperature controlled oven that heats bulk calcium into an atomic vapor. The atoms leave the oven through a nozzle that is 10 mm long and has a diameter of a few millimeters, which creates an atomic beam of neutral calcium. A laser beam directed opposite the atomic beam slows the atoms down and increases the loading rate of the MOT. We detune this "slowing" laser beam about four linewidths (145 MHz) below the 423 nm atomic resonance. A 672 nm "repump" laser pumps atoms that fall into the metastable $4s3d\ ^1D_2$ state

back into the ground state via the highly excited $4s5p\ ^1P_1$ state (see Fig. 2.1). With the slowing laser beam and repump laser this experiment typically achieves peak MOT densities on the order of 10^{10} cm^{-3}.

The 423 nm trapping laser beam is generated by amplifying and frequency doubling an 846 nm laser. The master laser is a continuous-wave (cw) extended-cavity diode laser with a 50 kHz linewidth and power output of about 15 mW. The output is optically isolated, amplified to 50 mW in a higher-power diode, and optically isolated again before entering a Ti:sapphire ring cavity. A pair of lenses outside of the cavity is used for mode matching. The cavity consists of four mirrors in a bow-tie configuration, which includes the input coupler, two curved mirrors, and a "tweeter" mirror mounted on a piezoelectric crystal. The cavity length is adjusted by applying a voltage across the piezo. This is necessary to meet the resonance condition, which is the requirement that the round-trip optical path length of the cavity must be equal to an integer of the master laser's wavelength. The output from the cavity is about 1-W when the Ti:sapphire crystal is pumped with 7-W from a solid state laser at 532 nm [38].

In our configuration, the master laser is locked to the Ti:sapphire cavity. This is accomplished by modulating the diode current to produce frequency sidebands that can be used to phase lock the laser to the cavity using the Pound-Drever-Hall technique. When the system is injection-locked, adjustments to the frequency of the laser are made by adjusting the voltage that feeds back to the piezoelectric crystal that changes the cavity length. It is important that the frequency of the master laser is precisely controlled. We have two methods for locking the wavelength to the appropriate transition. In one case we use saturated absorption spectroscopy and lock-in detection to produce an error signal that can be used in a feedback loop that controls the voltage to the piezo and thus the frequency of the laser, as described in Sec. 2.3.1. In the other case we pick off part of the output of the diode laser and mix it on a photodiode with part of the output of a 1-GHz repetition rate mode-locked femtosecond laser. An optical frequency comb is generated from the stabilized

output of the femtosecond laser. Details regarding its usage in our experiment are found in Sec. 2.3

2.1.2 Plasma creation

Once the calcium atoms are trapped, we photoionize them using a two-photon ionization process. This ionization is achieved using co-propagating 3 ns pulse lasers at 423 nm and 390 nm (see Fig. 2.1). These lasers drive the $4s^2\ ^1S_0 \rightarrow 4s4p\ ^1P_1^o$ and the $4s4p\ ^1P_1^o \rightarrow$**continuum** transitions, respectively. The 390 nm pulse is generated from a tunable dye laser, pumped by a 355 nm pulsed Nd:YAG laser. By adjusting the wavelength of the 390 nm laser (which drives the transition into the continuum), we can vary the initial energy of the electrons in the plasma, because the excess photon energy above the ionization limit is carried away by the electrons. The minimum temperature of electrons in plasmas ionized right at threshold is determined by the 0.5 cm^{-1} bandwidth of the ionizing laser to about 0.5 K.

For the experiment in Ca^{2+} a second ionization stage is required to take the singly ionized Ca to the second ionization state. Pulsed dye lasers, which overlap temporally and spatially, are used to generate the Ca^{2+} plasma. There are multiple available pathways to achieve second ionization; choosing one is a matter of wavelength convenience and laser output power. A system was designed and implemented in which a set of three laser pulses go from the $4s\ ^2S_{1/2} \rightarrow 4p\ ^2P_{1/2}^o$ states, at 397 nm, then from $4p\ ^2P_{1/2}^o \rightarrow 5d\ ^2D_{3/2}$, at 210 nm, and finally from $5d\ ^2D_{3/2} \rightarrow$**continuum** (see Fig. 2.1). We achieve narrowband excitation at 397 nm by pulse amplifying and frequency doubling a cw diode laser at 794 nm. Similarly, for the 210 nm transition, we pulse amplify and frequency double the output of a cw diode laser at 840 nm and then pulse amplify and frequency double again to reach 210 nm. Since the linewidths of the 397 nm and 210 nm transitions are narrow, those transitions do not require much power to saturate. The last step into the continuum requires more power, however. The wavelength needed to achieve ionization at threshold is 434 nm. Unfortunately, the gain for the dye we use falls off rapidly at 434 nm, and with the pump

power available to us it was not possible to achieve the necessary power to doubly ionize enough of the plasma at this wavelength. Instead we use the 355 nm output ($\sim$ 70mJ/pulse) of a Nd:YAG laser to make that last ionization step, with the obvious disadvantage that we are unable to vary the electron temperature.

We use an AOM to turn off the MOT beams about 12 μs before the first ionization so that the 355 nm pulse does not ionize excited state neutral atoms in the MOT. These neutral atoms can come from atoms that were not ionized with the 390 nm pulse, or from recombined atoms. If the MOT beams are not turned off, the ionization of neutral atoms with the 355 nm pulse produces very hot electrons that heat the plasma significantly. Additionally, the wavelength of the 390 nm laser is set above threshold, so that the initial electron temperature is approximately $T_e = 2E_e/3k_B \sim 167$ K, which greatly reduces three-body recombination.

2.2 Plasma detection and density measurements

A variety of methods have been used to measure ion dynamics in ultracold plasmas. Some of the earliest ultracold plasmas at NIST in Maryland were probed using rf techniques [16]. In this technique an rf signal of known frequency is applied to an expanding plasma. When the plasma frequency, which depends on density, matches the frequency of the rf signal, the plasma electrons begin to oscillate and are ejected from the plasma. These electrons are then measured by a channeltron. Changing the rf frequency and measuring the electron count for different times allows one to map out the average density of the plasma. This technique provides averaged measurements, but has poor temporal resolution and no spatial resolution. Later, other techniques, such as absorption imaging [7] and fluorescence spectroscopy [8], were developed which provided much better temporal and spatial resolution.

2.2.1 Optical absorption

Optical absorption detection uses a probe laser beam tuned to a resonance transition in the ions. The plasma is illuminated by the probe beam, and the laser intensity is measured by a CCD camera with and without the plasma. Absorption of the probe laser beam is given by Beer's Law, $I = I_0 \exp(OD)$, where OD is the optical depth. Taking the ratio of the measurements made with the CCD camera allows us to calculate the optical depth. The transmission signal, $T = 1 - A$, is used to calculate the optical depth:

$$\begin{aligned} OD(x,y,z) &= -\ln(T_{background}/T_{plasma}) \\ &= \alpha(\nu) \int_{-\infty}^{\infty} dz\, n_i(x,y,z), \\ &= \sqrt{2\pi}\sigma_z \alpha(\nu) n_{0i} \exp\left(-\frac{x^2+y^2}{2\sigma^2}\right), \end{aligned} \tag{2.1}$$

where n_{0i} is the peak ion density and $\alpha(\nu)$ is the absorption cross section [7]. Absorption imaging is a significant improvement over the rf techniques used to probe the first ultracold plasmas. It provides information about the spatial resolution and has much better temporal resolution, but is still limited by the time response of the CCD camera to about 25 ns.

We use optical absorption to estimate the density of atoms in the MOT. We use the same procedure described above, but instead of illuminating the plasma, we illuminate the MOT with a resonant probe laser beam at 423 nm. Using the CCD camera, we take a series of images, from which we can calculate the transmission and the optical depth using Eq. 2.1. Sample data of the calculated transmission and optical depth is shown in Fig. 2.4.

2.2.2 Density measurements

The density of the plasma is determined using a variation of the absorption imaging technique described in Sec. 2.2.1. We measure the density of the atoms in the MOT before and after ionization, and the change in the MOT density gives us the plasma density. A 423 nm probe beam, resonant

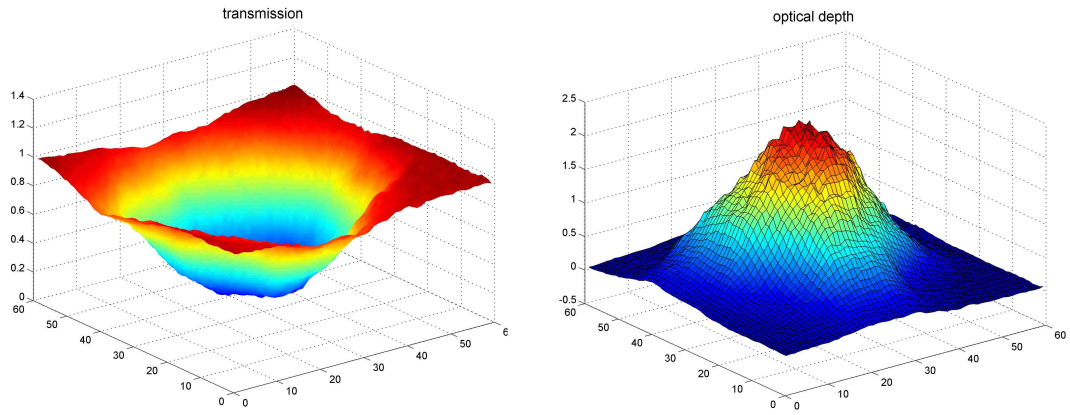

Figure 2.4 Sample data of the transmission (left) and optical depth (right). The MOT is illuminated by the probe beam at 423 nm and the laser intensity is measured by a CCD camera with and without the MOT to get the transmission. The optical depth is found using Eq. 2.1.

with the $4s^2\ {}^1S_0 \rightarrow 4s4p\ {}^1P_1^o$ transition in neutral calcium, is focused through the center of the MOT before and after ionization. The transmitted light is detected using a PMT. The transmission signal is used to calculate the optical depth, which is related to the density by Eq. 2.1. From Beer's Law and Eq. 2.1 we get

$$T = \exp\left(-\alpha(\nu)\int dz\, n(z)\right) \tag{2.2}$$

for the transmission. The optical depth is

$$-\ln(T) = \alpha(\nu)\int dz\, n(z). \tag{2.3}$$

For these measurements, the probe laser beam is directed along the z-axis through the geometric center of the plasma and focused at $x = y = 0$, which means that these equations, as well as Eq. 1.3 and Eq. 1.5, depend only on z. Additionally, since we measure the density of the neutral calcium, we can use Eq. 1.5 to find $n(z)$, which does not depend on the plasma expansion. The

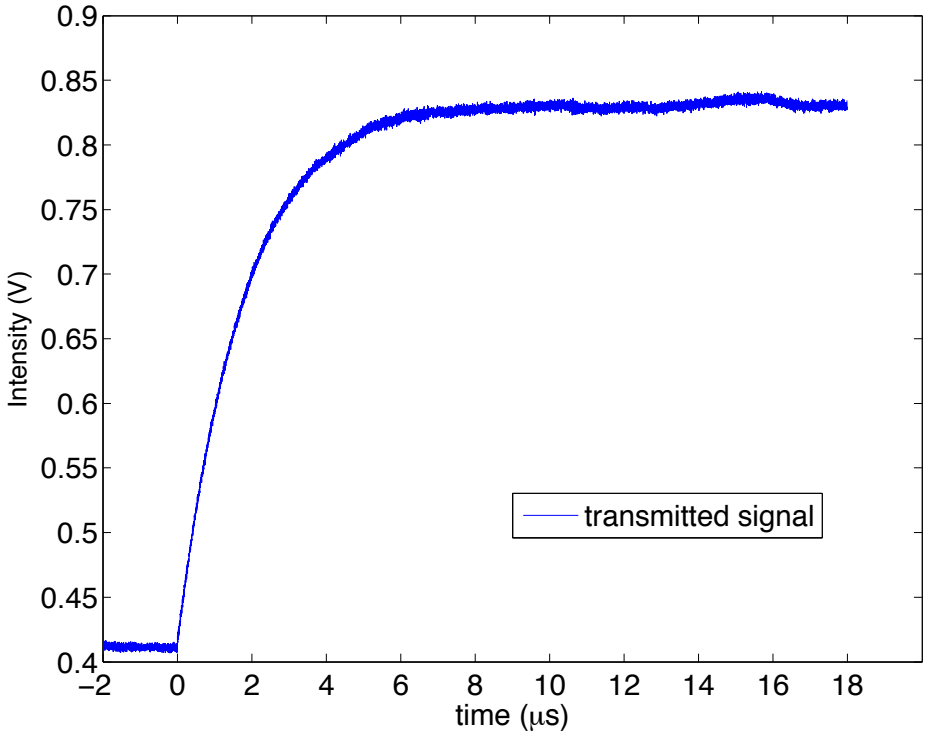

Figure 2.5 Sample absorption data. The transmission of the 423 nm probe laser beam is measured as a function of time using a PMT.

difference in optical depth is therefore

$$\begin{aligned} \ln(T_a) - \ln(T_b) &= -\alpha(\nu) \int n_{0a} \exp(-z^2/2\sigma^2) dz \; + \; \alpha(\nu) \int n_{0b} \exp(-z^2/2\sigma^2) dz \\ &= (n_{0b} - n_{0a}) \alpha(\nu) \int \exp(-z^2/2\sigma^2) dz. \end{aligned} \tag{2.4}$$

Measurements are taken before and after ionization, as denoted by the subscripts b and a, respectively. When the plasma is created, the atoms which are ionized no longer interact with the 423 nm probe beam. This accounts for the change in the measured intensity signal, shown in the sample absorption data in Fig. 2.5. Therefore the peak plasma density n_{0i} is equal to the change in the MOT density

$$n_{0i} = n_{0b} - n_{0a} = \frac{\ln(T_b/T_a)}{\alpha(\nu) \int \exp(-z^2/2\sigma^2) dz}. \tag{2.5}$$

With the 423 nm probe beam exactly on resonance, the absorption cross section is $\alpha(0) = 3\lambda^2/2\pi$. We can now simplify the denominator of Eq. 2.5 to

$$\alpha(\nu)\int \exp(-z^2/2\sigma^2)dz = \frac{3\lambda^2\sigma}{\sqrt{2\pi}}. \tag{2.6}$$

The calculated initial plasma density is therefore

$$n_{0i} = \frac{\sqrt{2\pi}\,\ln(T_b/T_a)}{3\lambda^2\sigma}. \tag{2.7}$$

2.2.3 Laser-induced fluorescence

Studies of early plasma dynamics on the nanosecond time scale require even finer temporal resolution than available through the absorption imaging techniques described in Sec. 2.2.1. This can be accomplished using fluorescence spectroscopy on the plasma ions. A cw probe laser beam, tuned to the $4s\,^2S_{1/2} \rightarrow 4p\,^2P^{\rm o}_{1/2}$ transition at 397 nm (see Fig. 2.1), is directed through the plasma and is absorbed. The ions are excited to the $^2P_{1/2}$ state, then emit photons as they spontaneously decay. Ions can also be optically pumped into the $^2D_{3/2}$ dark state, also shown in Fig. 2.1. The branching fraction into the dark state is about 7%. The intensity of the probe laser beam at the plasma is typically $s_0 = I/I_{\rm sat} \leq 1$, where the saturation intensity is $I_{\rm sat} = 46$ mW/cm^2. The natural linewidth $\gamma_{\rm N}$ of the 397 nm transition equals $1/2\pi\tau$ or 22 MHz. The laser beam is collimated, aligned to spatially overlap the plasma, and retroreflected. Fluorescence at 397 nm is collected using a lens, isolated using an optical band-pass interference filter, detected using a 1-GHz bandwidth photo-multiplier tube (PMT), and recorded using a 1-GHz bandwidth digital oscilloscope.

Fluorescence and absorption spectroscopy are effective detection tools because they are sensitive to ion motion and plasma dynamics through the Doppler shift. Ions at nearly zero velocity scatter photons from a resonant probe laser beam, producing a fluorescence signal. As the ions accelerate, their velocity (or temperature) increases and they are Doppler-shifted out of resonance with the probe beam. Ions that are no longer resonant with the probe beam are less likely to scatter

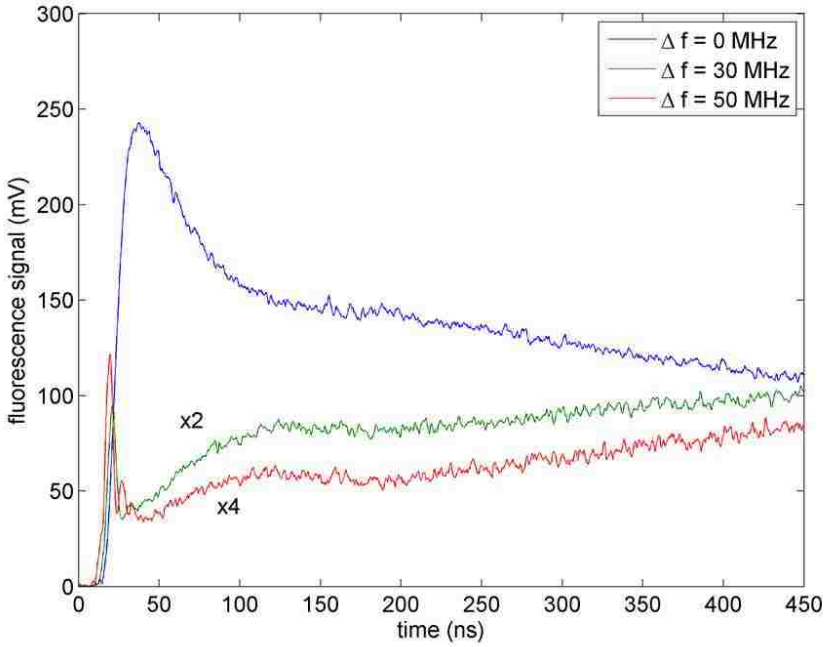

Figure 2.6 Typical fluorescence data obtained at three different detunings of the probe laser beam. As the ion velocity distribution broadens due to DIH and plasma expansion, the fluorescence signals change. The shoulder peak visible in the off-resonance plots at about 100 ns is due to DIH and it corresponds to the first kinetic energy oscillation (DIH peak) discussed in Sec. 1.3.2.

photons, corresponding to a drop in the fluorescence signal. Thus the signal is roughly proportional to the number of ions Doppler shifted into resonance with the probe. The detuning of the probe laser beam depends on the ions' motion due to DIH, the plasma expansion, and the initial detuning of the probe laser from the ion resonance frequency. Changing the initial offset of the probe laser allows us to probe ions of different velocity classes and to subsequently map out the time evolution of the (non-equilibrium) velocity distribution.

Sample fluorescence data can be seen in Fig. 2.6. At early times the fluorescence signal is dominated by the acceleration of the ions due to DIH, which broadens the velocity distribution. Depending on the probe laser beam detuning, this broadening affects the fluorescence signal differently. When the probe laser beam is on resonance (blue line in Fig. 2.6), the fluorescence signal

falls rapidly between 25 and 100 ns. The DIH process is the dominant mechanism for broadening the velocity distribution during this time. The signal level falls because fewer ions remain near zero velocity as time goes on. When the probe laser beam is detuned from resonance, DIH-broadening and plasma expansion Doppler-shift ions into resonance with the probe laser beam. Initially there are no ions on resonance with the detuned probe laser beam. However DIH broadens the distribution, causing a corresponding increase in the fluorescence signal that results in the peaks visible in the 30 MHz and 50 MHz detuned data in Fig. 2.6. This is the DIH peak discussed in Sec. 1.3.2. At this point the ions have moved under the influence of DIH to minimize their electric potential energy and have reached their most ordered state.

2.2.4 Fitting the fluorescence to a Voigt profile

We extract the time evolving ion velocity $v_{i,\mathrm{rms}}$ by fitting the fluorescence data to a Voigt profile. The Voigt profile is a mathematical representation of the absorption cross section per atom. It is the convolution of a Lorentzian and a Gaussian lineshape

$$V(\nu) = \int_{-\infty}^{\infty} L(\nu - \nu')G(\nu')d\nu' \tag{2.8}$$

with the Lorenztian and Gaussian profiles given by

$$L(\nu) = \frac{\gamma/\pi}{\nu^2 + \gamma^2} \tag{2.9}$$

and

$$G(\nu) = \frac{1}{\sqrt{2\pi}\nu_{\mathrm{rms}}} \exp[-\nu^2/2\nu_{\mathrm{rms}}^2], \tag{2.10}$$

respectively. In these equations, ν is the detuning from resonance, γ is half the natural linewidth of the atomic transition (the HWHM of the Lorentzian line shape), and ν_{rms} is the rms Gaussian width. The integral defined in Eq. 2.8 can be evaluated as

$$V(\nu) = \frac{\mathrm{Re}[w(z)]}{\sqrt{2\pi}\nu_{\mathrm{rms}}}. \tag{2.11}$$

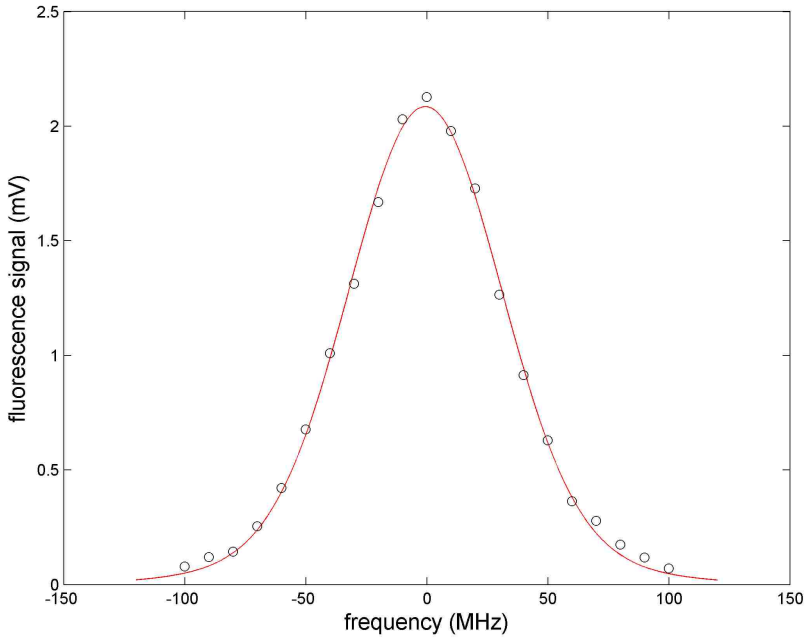

Figure 2.7 Voigt profile fit to the experimental data. The Voigt profile is the convolution of Lorentzian and Gaussian lineshapes. The Lorentzian half width is half the natural linewidth of the transition and is fixed at 11 MHz. The Gaussian width is extracted as a fit parameter and is used to find the rms velocity of the ions.

The term in the numerator is the complex error function, and it is given by $w(z) = e^{-z^2}\mathrm{erfc}\,(-iz)$, where z is $(\nu + i\gamma)/\sqrt{2}\nu_{\mathrm{rms}}$, and erfc is the complementary error function. In the analysis, the Lorentzian half width is equal to 11 MHz, half the natural linewidth of the 397 nm transition. The Gaussian width ν_{rms} is extracted as a fit parameter. It is converted to the rms width of the velocity distribution using the Doppler shift, $v_{i,\mathrm{rms}} = (k_B T_i/m_i)^{1/2} = \lambda\nu_{\mathrm{rms}}$, allowing us to map out the width of the ion velocity distribution as a function of time. Using the $v_{i,\mathrm{rms}}$ found from the Voigt fitting we are able to extract the ion temperature using the model described in Sec. 1.3.3.

2.3 Metrology

Our experiment requires the frequencies of our lasers to be stable and known. A number of techniques can be used to frequency stabilize the output of a laser, one of the most common being saturated absorption spectroscopy, which is described briefly in Sec. 2.3.1. For the first measurements in which we detuned the probe laser beam to map out the velocity distribution of the ions we used an AOM to detune the probe laser beam frequency. While functional, this method was not ideal, because each measurement required realigning the laser through the AOM, resulting in alignment shifts and intensity variations. We improved upon our measurements by using an external cavity as a reference, described in Sec. 2.3.2. While preferable to the AOM method, the cavity exhibited a slow MHz-level drift due to environmental factors that made precision measurements over an extended period of time impossible. Most recently we have implemented an optical frequency comb in our lab to address these issues and improve our metrology. Sec. 2.3.3 provides background information about optical frequency combs and Sec. 2.3.4 includes details about the experimental apparatus. A system built to automate our data acquisition is also briefly outlined.

2.3.1 Saturated absorption spectroscopy

The frequency of light as observed by a moving atom will depend on the velocity of that atom, due to the Doppler effect. To an atom traveling in a laser beam, the frequency of the photons will appear shifted. The change in frequency Δf is given by

$$\Delta f = -\frac{v}{c} f_L \tag{2.12}$$

where f_L is the frequency of the laser, v is the velocity of the atom, and c is the speed of light. Therefore an atom moving in a direction opposite to the direction of beam propagation, such that v is negative, will see a higher frequency in its frame of reference than that of the laboratory reference frame. This means that the atom will absorb photons that are at a lower frequency than

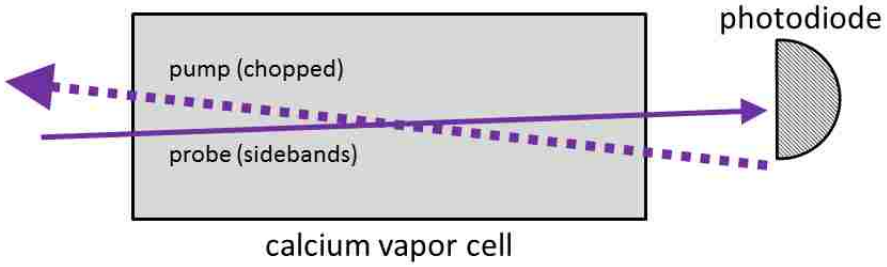

Figure 2.8 Saturated absorption spectroscopy. A pump beam and a probe beam are aligned to overlap in an atomic vapor cell. Due to the Doppler shift, the only atoms that both beams will address will be those with almost zero velocity. If one of the laser beams is detuned relative to the other, the two beams will address atoms of a particular velocity class, i.e. atoms moving with a velocity that Doppler shifts both lasers into resonance. The presence of the pump beam modifies the absorption profile of the probe beam, measured by the photodiode, by depleting the number of ground state atoms that the probe beam can interact with. Modulating and chopping the beams using an EOM and an AOM make it possible to use phase-sensitive detection techniques, as described in the text.

the resonant frequency of the atom. Conversely, an atom traveling in the opposite direction will appear to absorb photons with a higher frequency. The absorption spectrum of the atom is thus characterized by broad signals around each absorbed frequency. This "Doppler broadening" of the absorption profile makes it difficult to determine the precise transition frequency.

To overcome this challenge we use a process called saturation absorption spectroscopy, or Doppler-free spectroscopy. A system is setup whereby a fraction of the laser output is split into two beams, referred to as the pump beam and the probe beam, which enter an atomic vapor cell from opposite directions and overlap in the cell (see Fig. 2.8). A photodiode is set in the path of the probe beam to acquire a signal after it has passed through the vapor cell. In general, the pump and probe beams will interact with different atoms as a result of the Doppler effect, since they will only excite the atoms that have been Doppler shifted into resonance with the laser frequency. Because the beams are propagating in opposite directions they will interact with different atoms unless they are close to the resonant frequency, at which point both beams will interact with the atoms whose

relative velocity is zero along the axis of beam propagation, and begin inducing transitions from the ground state to the excited state. The pump beam will decrease the number of atoms in the ground state for the probe beam to interact with, allowing the probe beam to pass through the vapor cell without being depleted, even though it is on resonance. By adjusting the frequency of the laser we can map out the absorption profile, which no longer includes contributions from Doppler broadening.

In our lab we use frequency-modulated (FM) spectroscopy, which builds upon the saturated absorption scheme just described. This technique uses an electro-optic modulator (EOM) to modulate the frequency of the probe beam. The probe beam signal from the photodiode is then mixed with the signal used to drive the EOM to produce the derivative of the absorption profile, which is a dispersive lineshape that can be used as the error signal for a feedback circuit. The zero-crossing of the error signal, where the slope is steepest, corresponds to the peak of the absorption spectrum, or the atomic resonance.

We also use an AOM to chop the pump beam at about 100 kHz. The mixed down signal from the photodiode is then sent to a lock-in amplifier, which is referenced to the 100 kHz chopping signal. The lock-in detection suppresses amplitude and phase noise and subtracts off the Doppler background. In the case of 423 nm light, which for the purpose of cooling and trapping we want red-detuned, the AOM shifts the frequency of the pump beam by approximately 100 MHz. The same principle outlined in the description of saturated absorption applies, except that now the pump and probe beams interact with atoms of a particular velocity class, rather than the atoms with zero velocity. Atoms moving towards the pump beam with this velocity will see the pump beam shifted down in frequency by 50 MHz, while the probe beam will be Doppler-shifted up in frequency by 50 MHz. This gives us the 50 MHz detuning needed for Doppler cooling, described in Sec. 2.1.1.

2.3.2 External reference cavity

Using saturated absorption has the advantage of providing long term laser frequency stability at the sub-MHz-level for a fixed frequency. This works well for the 423 nm trapping frequency, which does not change. However, for the 397 nm fluorescence probe, whose frequency we would like to change, saturated absorption does not work well. We addressed this problem by using an external reference cavity. The cavity was constructed from a stainless steel cylinder, approximately 5 cm long. High reflectivity IR mirrors were fixed to the ends of the cavity and the cavity was sealed. The finesse of the cavity was $\mathscr{F} \approx 300$. The cavity was temperature controlled using a thermoelectric peltier, which was attached to a stainless steel mounting block. The cavity was also encased in thermally isolating material and placed in a sealed box.

A part of the light from a 794 nm low power cw diode laser was coupled into the TEM_{00} mode of the cavity and the transmission was measured on a photodiode. A side-lock was used to lock the laser to the reference cavity. With the diode laser locked to the cavity, a part of the light was split off and overlapped on a photodiode with light from a tunable Ti:sapphire laser at 794 nm before being frequency doubled to generate the 397 nm probe laser. The beat note measured by the photodiode was mixed down to 10 MHz using an RF signal generator, counted with a frequency counter, and sent to an interferometer. The output of the interferometer was low-pass filtered and used as the error signal for an offset lock. The Ti:sapphire laser frequency was locked to a zero-crossing in the interferometer.

By adjusting the output of the RF signal generator we could detune the frequency of the probe laser in a more controlled and systematic way than was possible using the saturated absorption and AOM scheme. With this improved metrology we were able to take the measurements described in Sec. 4.4, which were of sufficiently high quality that we could, for the first time, fit our fluorescence measurements to a Voigt profile to map out the time evolving velocity distribution. Although this was a significant improvement, the cavity still exhibited a 1.5 MHz drift on the minute time scale,

which was due to changes in the cavity length. This drift persisted despite our efforts to stabilize the cavity length and isolate the cavity from environmental influences. By monitoring the laser frequency on a wavemeter we were able to compensate for the drift to some degree, however ultimately we decided to abandon the external reference cavity in favor of an optical frequency comb.

2.3.3 Optical frequency combs

Optical frequency combs revolutionized the field of precision spectroscopy and are growing in importance in a variety of fields, with applications that range from metrology to communications to astronomy. Most frequency combs are generated using stabilized mode-locked femtosecond lasers, the most popular of these lasers being Kerr-lens mode-locked Ti:sapphire systems [39]. Such lasers take advantage of the lensing effect that arises when a short optical pulse propagates through a nonlinear medium. This Kerr self-focusing effect modulates the spatial intensity profile of the beam such that intense laser pulses are focused differently than cw light (see Fig. 2.9). The cw light exits the gain medium diverging slightly, whereas the pulsed beam has a smaller beam waist in the gain medium and diverges more strongly after the gain medium (not shown in Fig. 2.9). Operating the cavity on the edge of stability for cw-operation decreases the beam waist in the gain medium, and the self-focusing of the pulses makes it energetically favorable for the laser to operate in a pulsed mode [40]. This method for passively mode-locking a Ti:sapphire laser to generate femtosecond pulses is widely used. Additional cavity components are necessary to compensate for group-velocity dispersion, such as intracavity prism pairs or negative-dispersion mirrors [39].

A mode-locked laser produces ultrashort pulses at regular time intervals. The frequency spectrum of such a laser resembles a series of Dirac delta functions, each spectral line forming a “tooth” of the frequency “comb.” Each “tooth,” or “comb mode,” corresponds to a different frequency. The

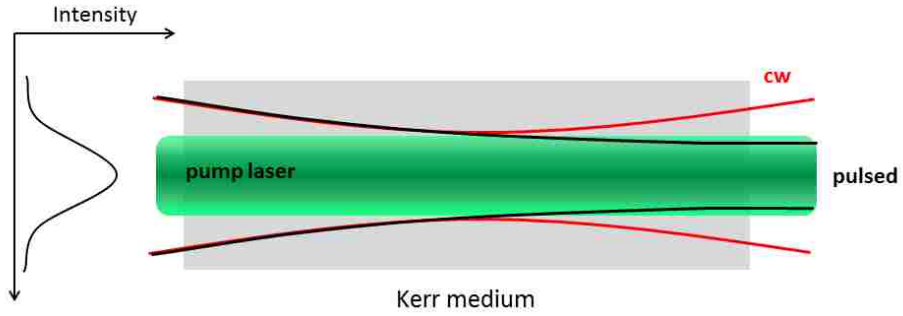

Figure 2.9 Self-focusing in a Kerr medium. The Kerr lensing effect modulates the spatial intensity profile differently for intense laser pulses and cw light. The result is a laser cavity in which pulsed operation is energetically favorable to cw-operation.

spacing between modes in frequency space is determined by the timing between individual laser pulses, which is called the repetition rate and is given by the length of the cavity. The higher the repetition rate, the larger the spacing between comb modes and the easier it is to resolve individual comb modes.

The usefulness of a frequency comb depends largely on its stability. There are two degrees of freedom with which we are concerned: the laser repetition rate f_{rep} and the carrier-envelope offset frequency f_{ceo}. The repetition rate, as previously mentioned, refers to the spacing between comb modes. The carrier-envelope offset refers to the offset of the entire comb from zero frequency. If both f_{rep} and f_{ceo} are known, then the frequency of each comb mode can be determined by the formula

$$f_n = f_{\text{ceo}} + n f_{\text{rep}} \tag{2.13}$$

where n is an integer, called the mode number. If f_{rep} and f_{ceo} are known and stabilized, then the absolute frequency of any laser whose frequency falls within the range of frequencies that make up the comb can be determined. This can be done by measuring the beat note between the laser of unknown frequency and the comb mode nearest to that frequency. Determining the repetition rate is straightforward and can be accomplished by simply measuring f_{rep} using a high-speed photodiode. Determining the carrier-envelope offset is more difficult. Typically f_{ceo} is found by broadening the

comb in a non-linear medium so that the frequencies span an entire octave. Modes from opposite ends of the comb's frequency spectrum are then compared. If $f_{\text{ceo}} = 0$ then the ratio of the two frequencies should be exactly 2. Any deviation from this ratio gives the value of the f_{ceo}. The carrier-envelope offset can be stabilized by putting an AOM into the beam path of the pump laser to vary the pump laser power. With f_{ceo} and f_{rep} both fixed, the comb is considered fully stabilized.

2.3.4 Partially stabilized frequency comb

In practice, a fully stabilized frequency comb using the self-referencing technique described above can be challenging. For some applications, where absolute accuracy is not of vital importance, it may be sufficient to operate the comb in a partially stabilized configuration. This section describes our setup for a *partially* stabilized frequency comb.

We generate a frequency comb using a 1 GHz repetition rate mode-locked fs laser. The oscillator is passively mode-locked and uses six negative dispersion mirrors. A schematic diagram of the frequency comb setup is provided in Fig. 2.10. Part of the femtosecond laser is picked off with a beam splitter and sent to a fast photodiode (PD1), which measures the repetition rate of the laser. This signal is band-pass filtered (BPF), mixed down using an RF generator (RF1) and a mixer (M) to 1.5 MHz, and counted with a frequency counter (C1), shown in Fig. 2.11. All of our counters and frequency synthesizers are referenced to a GPS disciplined 10 MHz Rb oscillator.

We offset-lock one mode of the comb to a reference laser that is stabilized to the $F = 2 \rightarrow F' = 3$ crossover transition in ^{87}Rb using saturated absorption. The output of the reference laser and part of the frequency comb are overlapped to produce a beat note that is measured on a photodiode (PD2). The signal is filtered (HPF/LPF) and split. Part of the signal goes to a spectrum analyzer, and the other part is mixed with a RF generator (RF2) and filtered. The output of the mixer is split and part of the signal goes to a frequency counter (C2) to be counted and the other part is sent to a microwave interferometer (gray box in Fig. 2.11), which consists of a power splitter, two

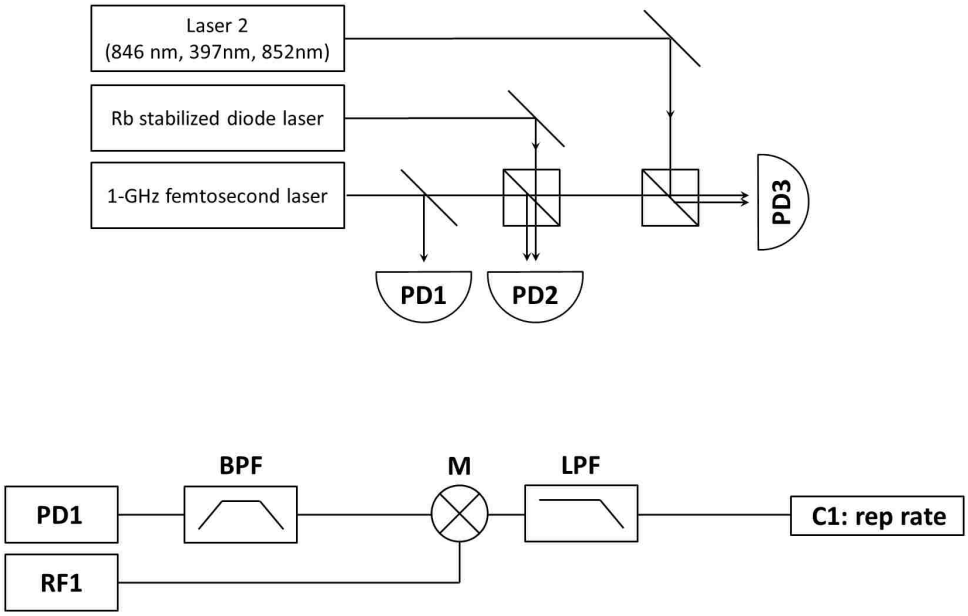

Figure 2.10 Schematic diagram of the frequency comb setup. The frequency comb is generated from the 1 GHz repetition rate femtosecond Ti:sapphire oscillator. Part of the femtosecond laser is picked off and measured on a fast photodiode (PD1). The signal is band-pass filtered (BPF) and mixed down in a mixer (M) with the output of an RF generator (RF1). The output of the mixer is then low-pass filtered (LPF) and counted on a frequency counter with mHz precision. Part of the femtosecond laser is split off and overlapped on a fast photodiode (PD2) with the output of a Rb-stabilized diode laser. One of the comb modes is offset locked to this laser (shown in top panel of Fig. 2.11). The beat note between an additional laser, Laser 2, and the comb can be measured (PD3) and its frequency can be offset locked to the comb (bottom panel of Fig. 2.11).

coaxial cables of different lengths to create a delay line (DL), and a frequency mixer [41]. The output of the interferometer is used as the error signal for an integral-gain feedback circuit that locks the beat note between the reference laser and the frequency comb to a zero-crossing of the interferometer output. The lock circuit feeds back to a fast and a slow piezoelectric transducer that adjusts the cavity length of the fs oscillator, which changes the frequency of the beat note between the diode laser and the nearest comb mode. The feedback circuit adjusts the cavity length so that the interferometer output is zero.

The microwave interferometer lock point drifts slowly. The interferometer phase is influenced primarily by temperature variations (a few kHz/°C), beat note amplitude variations, and fluctuations in the DC offset voltage due to a variety of sources, such as capacitive pickup. The frequency counter C2 is used to monitor the beat note between the diode laser and the comb when the beat note frequency is locked. The measured frequency variation is typically 1 kHz in a 1 second measurement interval, with larger variations over longer time scales.

With the comb partially stabilized we can measure or lock the frequency of other lasers in the lab, generically represented by "Laser 2" in Fig. 2.10. A part of the comb is split off and overlapped on a photodiode (PD3) with a portion of the laser whose frequency we want to measure or lock (see Fig. 2.11). The beat note is measured and locked in a way similar to the method described above. The frequency of the laser is

$$f_{\text{laser}} = f_{\text{Rb}} \pm f_{\text{b2}} + n f_{\text{rep}} \pm f_{\text{b3}} \tag{2.14}$$

where f_{Rb} is the ^{87}Rb crossover transition frequency, $f_{\text{b2}} = f_{\text{RF2}} \pm f_{\text{C2}}$ is the beat note between the reference laser and the nearest frequency comb mode, $f_{\text{b3}} = f_{\text{RF3}} \pm f_{\text{L2}}$ is the beat note between Laser 2 and the nearest frequency comb mode, and n is the mode number. By comparing the frequencies measured using the spectrum analyzers, the counters C2 and C3, and the RF synthesizers RF2 and RF3 we are able to determine the plus or minus signs in f_{b2} and f_{b3}. The plus and minus signs in Eq. 2.14 can be determined by changing the fs laser cavity length before the Rb offset-lock

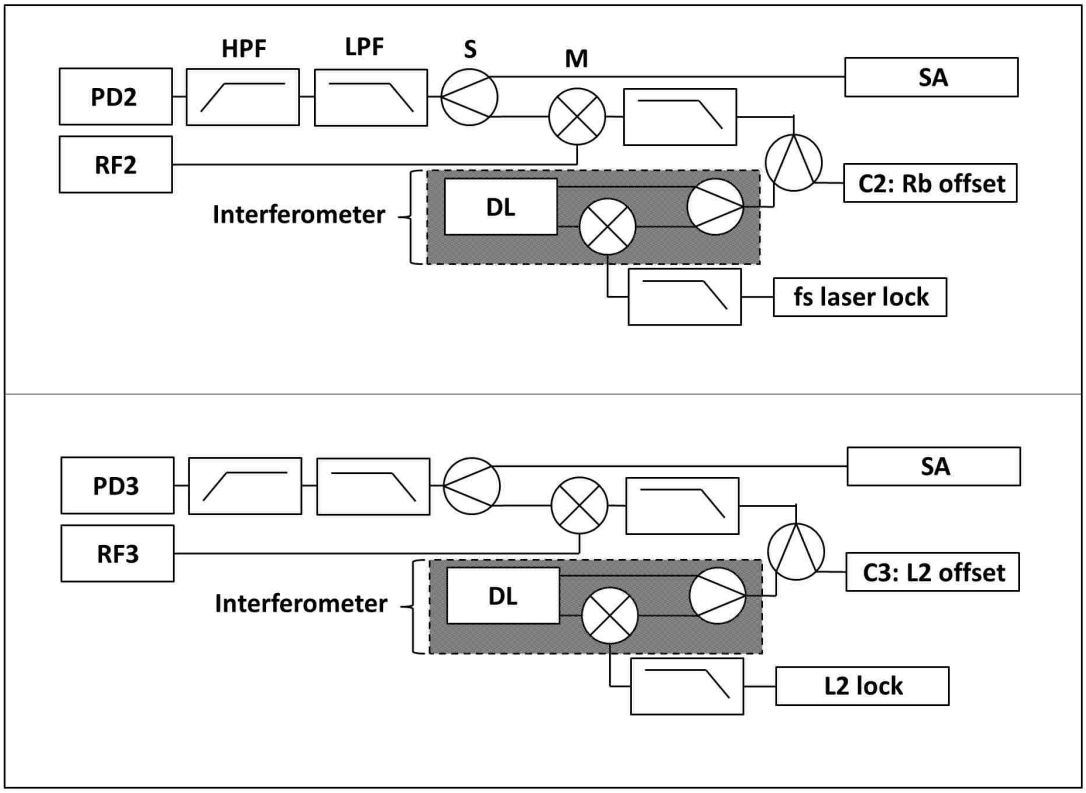

Figure 2.11 Schematic diagram of the interferometric locking technique used to stabilize the frequency comb to the Rb-stabilized diode laser and to lock other lasers to the comb. The photodiodes PD2 and PD3 are those indicated in Fig. 2.10. The top panel shows the setup for offset locking one of the comb modes to the Rb-stabilized diode laser, as described in the text. The bottom panel shows how another laser can be offset locked to one of the frequency comb modes. HPF = high-pass filter. LPF = low-pass filter. S = RF power splitter. M = RF frequency mixer. SA = RF spectrum analyzer. RF2 and RF3 are RF frequency synthesizers used to mix down the RF frequencies measured by the photodiodes to ranges that are more easily measured by the counters (C2 and C3).

is engaged and observing how the beat notes change.

The locking scheme described above is such that scanning the frequency of the RF generator allows us to scan the frequency of the laser. We lock the 397 nm probe laser in the fundamental to the frequency comb and then scan the frequency by controlling the RF output from a program in LabVIEW. The frequency counters are measured and recorded by the computer in order to find the detuning of the probe laser from the 397 nm resonance transition. This allows the data acquisition to be largely automated.

2.3.5 Fully stabilized frequency comb

If an accuracy on the order of 10 kHz is sufficient, the partially stabilized comb described in Sec. 2.3.4 can be very convenient, as it can operate unattended for several hours. Inserting an AOM into the fs laser's pump beam makes it possible to lock the repetition rate by adjusting the pump power [42]. When the repetition rate is locked and one of the comb modes is offset-locked to the Rb diode laser, the frequency comb is fully stabilized. In its fully stabilized configuration, the frequency comb exhibits improved accuracy, at the expense of some convenience. Modulating the pump power introduces intensity-related spectral shifts, like those described in Ref. [39], that are still not well understood in our system. The transfer function between the pump power and f_{rep} is not monotonic. This means that over some ranges of the pump power it increases with pump power and over others it decreases. There are also "fixed points" in the comb where changing the pump power has no effect on f_{rep}.

To stabilize the repetition rate by adjusting the pump power we use the setup shown in Fig. 2.12. We use an ultra low noise crystal oscillator at 5 MHz as our reference. The signal from the photodiode that measures the repetition rate (PD1 in Fig. 2.10) is mixed down with a RF synthesizer to 640 MHz. The signal out of the mixer is high-pass and low-pass filtered and then divided down to 10 MHz using a divide-by-64 to reduce phase noise. Alternatively, the repetition rate can be mixed

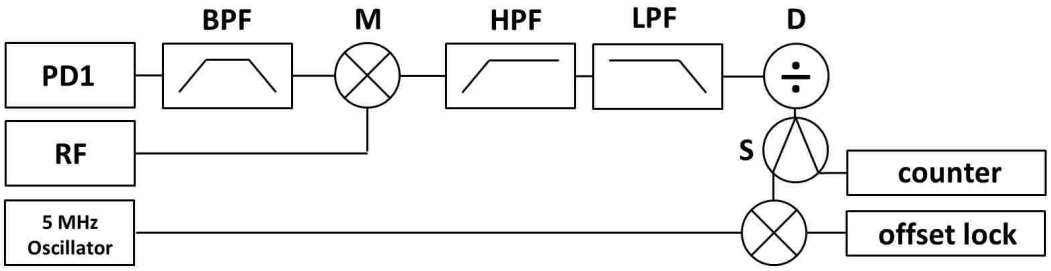

Figure 2.12 Schematic diagram of the repetition rate lock. A photodiode (PD1) measures the repetition rate of the fs laser. The signal is band-pass filtered (BPF) and mixed (M) with an RF signal. The mixed down signal is high-pass (HPF) and low-pass (LPF) filtered and divided down (D) to reduce phase noise. The signal is split and part is sent to a frequency counter and the other is mixed with the output of an ultra low noise crystal oscillator. The output of the mixer is used as the error signal for an offset lock that adjusts the pump power to stabilize the repetition rate.

down to 40 MHz and divided down to 5 MHz using a divide-by-8. In the latter configuration the comb has better absolute accuracy, but is more sensitive to noise, such as noise in the pump laser. After the signal has been divided down it is split, and part of the signal goes to a frequency counter and the other part is mixed with the crystal oscillator reference. The mixed signal is filtered and used as the error signal for an offset lock that adjusts the pump power.

Chapter 3

Characterization of optical frequency comb

In our lab we have implemented an optical frequency comb that we can operate in a partially or fully stabilized mode, as described in Sec. 2.3.3. To characterize the comb's performance we measured frequency intervals between the Rb-stabilized diode laser and three other transitions: the Cs D2 $F = 3 \rightarrow F' = 3/4$ crossover transition at 852 nm, the ^{85}Rb D1 $F = 3 \rightarrow F' = 2$ transition at 794 nm and the ^{40}Ca $4s^2\ ^1S_0 \rightarrow 4s4p\ ^1P_1^{\mathrm{o}}$ transition at 423 nm.

3.1 Cesium measurement

We locked a laser to the Cs D2 $F = 3 \rightarrow F' = 3/4$ crossover transition at 852 nm using saturated absorption and looked at the drift in the measured frequency, shown in Fig. 3.1. For the first 650 seconds of the measured signal, the fs laser repetition rate was locked, i.e. the comb was fully stabilized (see Sec. 2.3.5). After 650 seconds, we unlocked the repetition rate. As expected, the noise in the measured frequency interval increased, as seen in the bottom panel of Fig. 3.1.

In some sense, this data represent a "worst-case" scenario for our mode-locked laser because of the 70 nm interval between the lasers locked to saturated absorption in Rb and Cs. Small variations in the repetition rate are multiplied by a large mode number n (see Eq. 2.14).

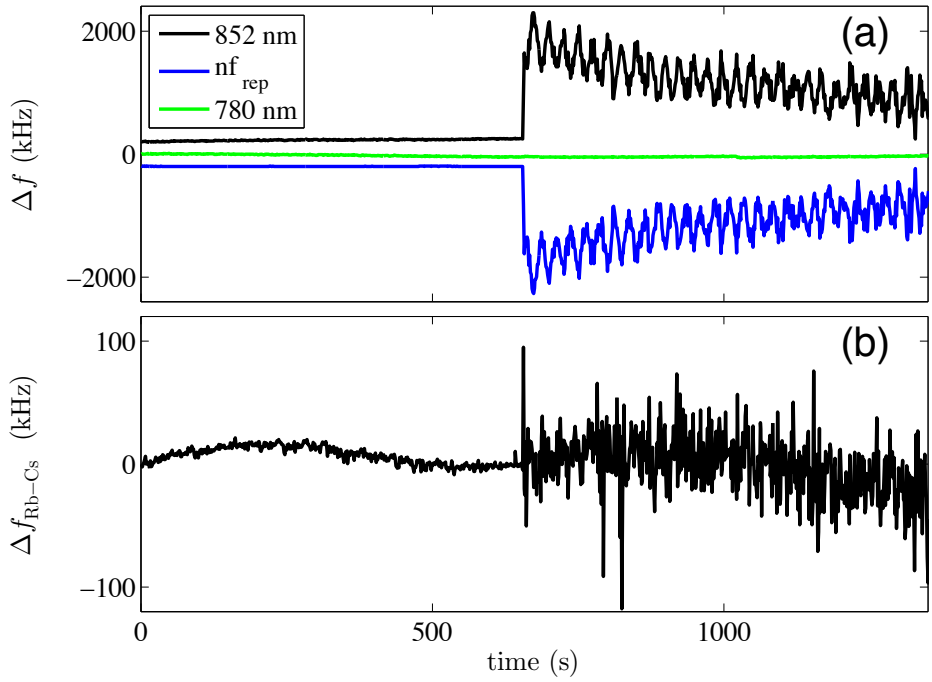

Figure 3.1 (a) Changes in the measured beat notes and scaled repetition rate nf_{rep} and (b) changes in the calculated frequency interval between the Cs D2 $F = 3 \rightarrow F' = 3/4$ crossover transition at 852 nm and the Rb D2 $F = 2 \rightarrow F' = 2/3$ crossover transition at 780 nm. A laser is locked to the Cs transition using saturated absorption. The repetition rate lock is turned off at $t = 650$ s, leaving the comb partially stabilized with only one comb mode actively locked to the Rb-stabilized diode laser. The slow drift in the $\Delta f_{\text{Rb-Cs}}$ is due to a drift in the saturated absorption lock point.

When the repetition rate is not locked, high frequency noise in our frequency comb around 2.5 kHz increases the variability in the counted repetition rate. In addition, a somewhat large frequency excursion with an approximately 30 second period is displayed. This corresponds to the time constant of the temperature feedback loop in the water chiller used to control the fs laser baseplate temperature. We see the effect of the baseplate temperature fluctuations from time to time, depending on the environmental conditions in our lab. However, this variation is slow enough that the frequency counting removes it from our measurement of the Rb-Cs frequency interval. Due to this thermal fluctuation, the repetition rate itself is changing by roughly $\pm$ 12 Hz ($df/f \sim 10^{-8}$) on a 30 second time scale. When this variation is multiplied by the mode number, $n \approx 33000$ for the Rb-Cs frequency interval, the repetition rate instability amounts to $\pm$400 kHz at 852 nm. Still, this large variation is accurately accounted for in the measured beat notes when the repetition rate is not locked. The fractional Allan deviation of the first 650 second of data in Fig. 3.1 falls below 4×10^{-12} at about 5 seconds of integration. For the unlocked data, the fractional Allan deviation falls below 20×10^{-12} at about 20 seconds.

3.2 Rubidium measurement

We locked a cw Ti:sapphire laser to the ^{85}Rb D1 $F = 3 \rightarrow F' = 2$ transition at 794 nm using saturated absorption. The drift in the measured frequency is shown in Fig. 3.2. For these measurements, the repetition rate was not locked. The thermal loading visible in Fig. 3.1 is not present. Even if it were, the much smaller mode number corresponding to the Rb D1 to Rb D2 frequency interval ($n \approx 7000$) would make it insignificant. The variation in the repetition rate counting does not contribute appreciably to the uncertainty budget in the measured interval.

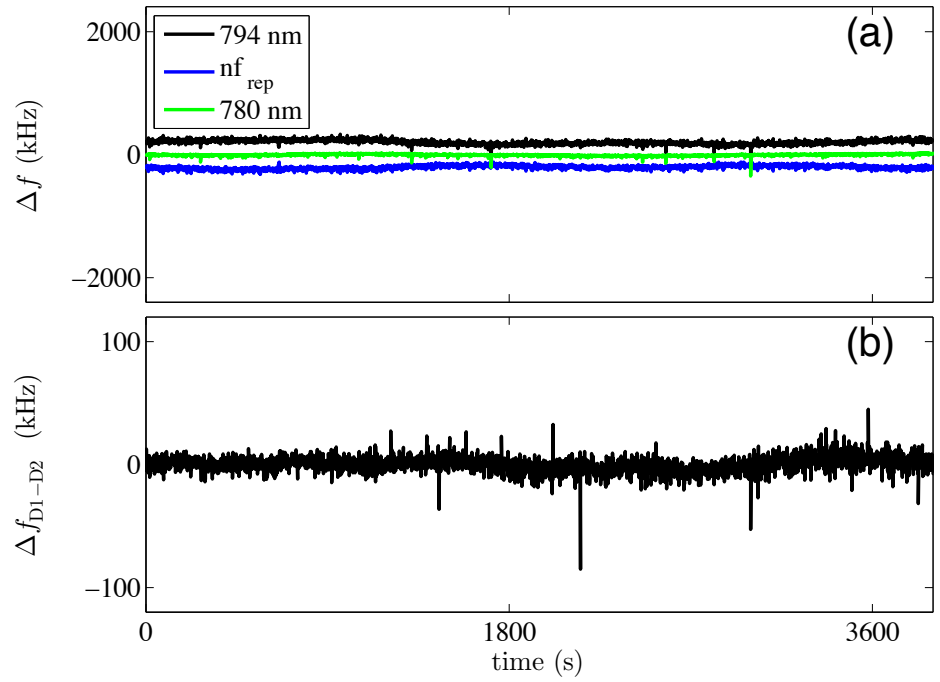

Figure 3.2 (a) Changes in the measured beat notes and scaled repetition rate nf_{rep} and (b) changes in the calculated frequency interval between the ^{85}Rb D1 $F = 3 \rightarrow F' = 2$ transition at 794 nm and the ^{87}Rb D2 $F = 2 \rightarrow F' = 2/3$ crossover transition at 780 nm. For this data, only the offset lock between one comb mode and the Rb-stabilized diode laser is engaged (partially stabilized configuration).

3.3 Calcium measurement

For these measurements we used the laser described in Sec. 2.1.1 at 846 nm, frequency doubled to 423 nm. The 423 nm beam was attenuated and aligned to be perpendicular to a collimated Ca atomic beam. The laser beam was retro-reflected back onto itself to minimize the Doppler shift of the transition frequency. Fluorescence from the atomic bean was collected as the laser frequency was scanned across the resonance. The laser was offset-locked to the frequency comb in the fundamental, as described in Sec. 2.3.4, and the frequency of the RF synthesizer was changed in order to scan the laser frequency. The frequency of the RF signal generator was changed over a $\pm$50 MHz interval, shifting the frequency of the 423 nm laser by $\pm$100 MHz. This method of scanning the frequency of the 423 nm laser is facilitated by the 1 GHz-wide mode spacing of the frequency comb, since the mode spacing is wide enough that the laser remains locked to the same comb mode during the laser frequency scan. Each data point in Fig. 3.3 corresponds to a measurement time of 30 seconds. At each frequency, the fluorescence from the atomic beam was measured. In order to minimize the influence due to systematic drifts in either laser beam or atomic beam intensity, the offset frequencies at which the fluorescence is measured are chosen at random from a pre-determined list of frequencies.

Also shown in Fig. 3.3 is a fit to a Voigt lineshape. The fitted Lorentzian width is 35.3 MHz, in good agreement with the experimental value of the 35.2 MHz [43]. The fitted Gaussian width is 7.1 MHz, in good agreement with the measured divergence of the atomic beam (less than 0.01 radians).

Comparing our measured value of the ^{40}Ca $4s^2\ ^1S_0 \rightarrow 4s4p\ ^1P_1^o$ transition frequency to the value of 709 078 373.01(35) MHz from Ref. [44] shows good agreement, with our value 0.82 MHz higher. Our measurement cannot be considered definitive because the laboratory magnetic fields are not canceled. This could lead to a frequency error as large as 0.4 MHz. In addition, errors related to the lock point offset in our Rb diode laser are on the 0.2 MHz level.

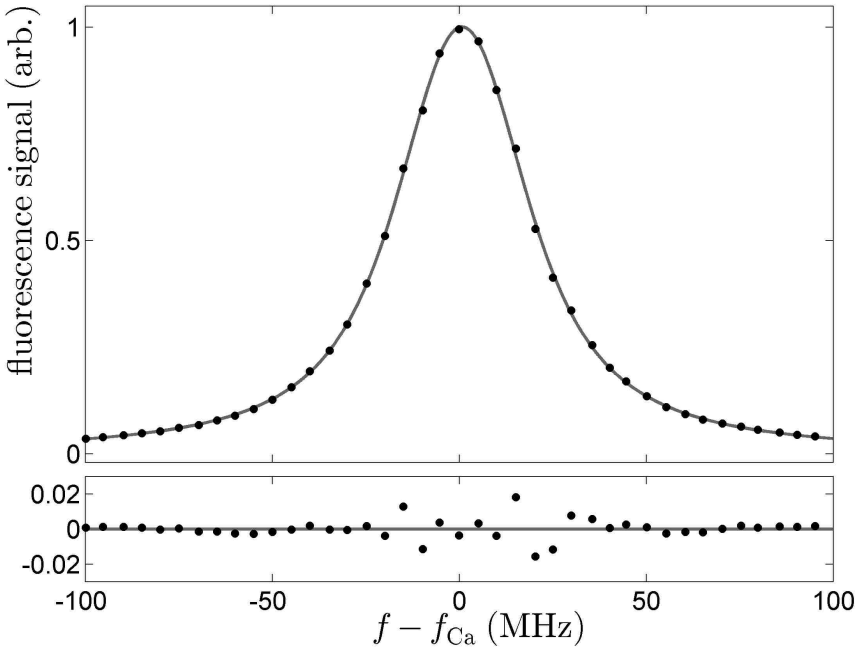

Figure 3.3 Fluorescence signal collected from a collimated atomic calcium beam (top panel). A laser at 846 nm is offset-locked to the frequency comb. It is frequency doubled to 423 nm and used to excited the ^{40}Ca $4s^2\ ^1S_0 \rightarrow 4s4p\ ^1P_1^{\mathrm{o}}$ transition. The black dots are the data and the solid line is a Voigt profile fit. The Lorentzian FWHM is 35.3 MHz, the Gaussian RMS width is 7.1 MHz. The bottom panel shows the residuals of the fit.

Chapter 4

Electron shielding in ultracold neutral plasmas

Motivation for investigating the influence of electron screening on the DIH process came from previous work with ultracold plasma simulations that showed that the ion motion during the DIH phase appeared to be more or less unchanged with increased electron screening [45]. This past work showed that the nominal ion plasma frequency set the time scale for DIH and that this time scale was essentially unaffected by electron screening. Given that DIH is fueled by the excess potential energy that the ions have due to their spatial disorder, it seemed counterintuitive that electron screening, which modifies the ion-ion interaction strength, would have no effect on the DIH time scale or the equilibrium ion temperature.

The following sections provide a theoretical background for understanding the relationship between electron screening and the ion plasma frequency, which sets the time scale for DIH.

4.1 Theoretical models

4.1.1 Nearest-neighbor model

If the screening length is λ_D, the one-dimensional screened (Yukawa) potential between ions i and j can be written as

$$U_{ij} = \frac{e^2}{4\pi\varepsilon_0}\frac{e^{-x_{ij}/\lambda_D}}{x_{ij}}, \tag{4.1}$$

where x_{ij} is the distance between ions i and j. Taking the derivative of Eq. 4.1 with respect to x gives us the force

$$\begin{aligned} F &= -\frac{e^2}{4\pi\varepsilon_0}\left(-\frac{e^{-x/\lambda_D}}{x^2} - \frac{e^{-x/\lambda_D}}{x\lambda_D}\right) \\ &= \frac{e^2}{4\pi\varepsilon_0 x^2}\left(\frac{x}{\lambda_D}+1\right)e^{-x/\lambda_D}, \end{aligned} \tag{4.2}$$

where the subscripts have been dropped for simplicity's sake.

One can imagine two ions fixed on the $x-$axis at a distance $\pm a_{ws}$ from the origin (see Fig. 4.1). If a third ion, a test particle, constrained to move only along the x-axis, is placed a small distance x from the origin and released, it will execute an oscillatory motion. For the case with screening, the force on the test particle can be written as

$$F = \frac{e^2}{4\pi\varepsilon_0(a_{ws}+x)^2}\left(\frac{a_{ws}+x}{\lambda_D}+1\right)e^{-(a_{ws}+x)/\lambda_D} - \frac{e^2}{4\pi\varepsilon_0(a_{ws}-x)^2}\left(\frac{a_{ws}-x}{\lambda_D}+1\right)e^{-(a_{ws}-x)/\lambda_D}. \tag{4.3}$$

We can expand Eq. 4.3 for $x \ll a_{ws}$. The leading non-vanishing term is linear in x, similar to a harmonic oscillator. The force on the test particle is therefore

$$F = -\frac{e^2}{2\pi\varepsilon_0 a_{ws}^3}\left(1+\kappa+\frac{\kappa^2}{2}\right)\exp(-\kappa)\,x, \tag{4.4}$$

where $\kappa = a_{ws}/\lambda_D$ and κ is the inverse scaled screening length. If we recognize this as a simple harmonic oscillator, we can write the ion oscillation frequency as

$$\omega = \omega_p f(\kappa), \tag{4.5}$$

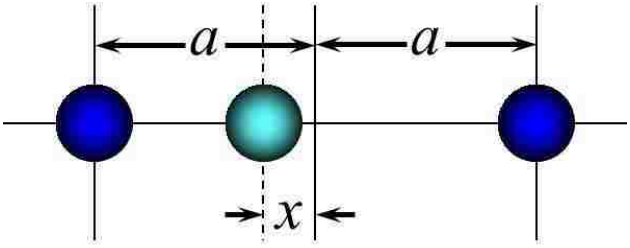

Figure 4.1 A one dimensional representation of the nearest neighbor model. The displaced test particle will oscillate about the origin. If the displacement is much smaller than a_{ws}, the force on the test particle is linear in x, and can be modeled as a harmonic oscillator.

where $f^2(\kappa) = (2/3)(1+\kappa+\kappa^2/2)\exp(-\kappa)$ and $\omega_p = (ne^2/4\pi\varepsilon_0)^{1/2}$. Expanding this expression to the first non-vanishing correction in κ gives

$$\omega \approx 0.82\omega_p\left(1-\frac{\kappa^3}{12}\right), \tag{4.6}$$

showing that the oscillation frequency in this overly simple one-dimensional model goes down as κ increases, but that this dependence is very weak.

4.1.2 Molecular dynamics model

A detailed treatment of the initial ion motion in ultracold plasmas is given in Ref. [45]. The early-time evolution of the velocity distribution is described by Eq. (3) in that paper,

$$T(t) = T(0) + (t/\tau_2)^2 + (t/\tau_4)^4 + \cdots, \tag{4.7}$$

where T is the effective ion temperature in units of $e^2/4\pi\varepsilon_0 a_{ws}k_B$ and t is the time in units of the plasma period. If we write the effective ion temperature in SI units as $T = m_i v_{\rm rms}^2/2k_B$ and take the initial ion temperature $T(0) = 0$, then this equation can be rewritten as

$$v_{\rm rms}^2 = \left(\frac{e^2}{4\pi\varepsilon_0 m_i a_{ws}}\right)\left(\frac{ne^2}{m_i\varepsilon_0}\right)\left(\frac{t^2}{\tau_2^2}\right), \tag{4.8}$$

where we have kept only the leading term in the series. From the simulation, the parameter $\tau_2 = 3/(33-4\kappa+0.1\kappa^2)^{1/2}$. We solve Eq. 4.8 for v_{rms} and find

$$\begin{aligned} v_{\text{rms}} &= 1.1055 a_{ws}\omega_p^2 \left(1-0.1212\kappa+0.0030\kappa^2\right)^{1/2} t \\ &\approx 1.1055 a_{ws}\omega_p^2 (1-0.0606\kappa-0.0003\kappa^2) t. \end{aligned} \tag{4.9}$$

The inverse scaled screening length scales with electron temperature and density as $\kappa \propto T_e^{-1/2} n_0^{1/6}$.

In the context of this discussion, the important result of these two models is that the initial acceleration due to DIH has an extremely weak dependence on κ, meaning that the density dependence of the DIH process is predicted to be extremely weak, since $\kappa \propto n_0^{1/6}$.

4.2 Density and temperature scaling of DIH

In order to better understand the dependence of the DIH process on density and the initial electron temperature, fluorescence measurements were made during the DIH phase to determine the time scale over which DIH occurred for a range of plasma densities and initial electron temperatures. Only the results of these measurements are summarized here, but further details regarding the experiment and its results can be found in Ref. [9], which has been included in Appendix C.

Using methods described in Ref. [9], we found the time at which the DIH peak occurs, which we refer to as the characteristic DIH time t_0. These measurements used a probe laser beam at a fixed frequency using saturated absorption, described in Sec. 2.3.1, and detuned to 90 MHz using an AOM. Data showing the temperature and density dependence of t_0 is plotted in Fig. 4.2. In the absence of electron screening, the DIH time is expected to scale as $t_0 \propto n^{-1/2}$, which is plotted as the gray dashed line in the top panel of Fig. 4.2. We see that at low densities and electron temperatures much greater than the correlation temperature T_c (see Eq. 1.10) that the $t_0 \propto n^{-1/2}$ relationship holds. However, as we decrease the screening length λ_D by increasing the density and bringing the electron temperature closer to T_c, we see that the time t_0 departs from the expected

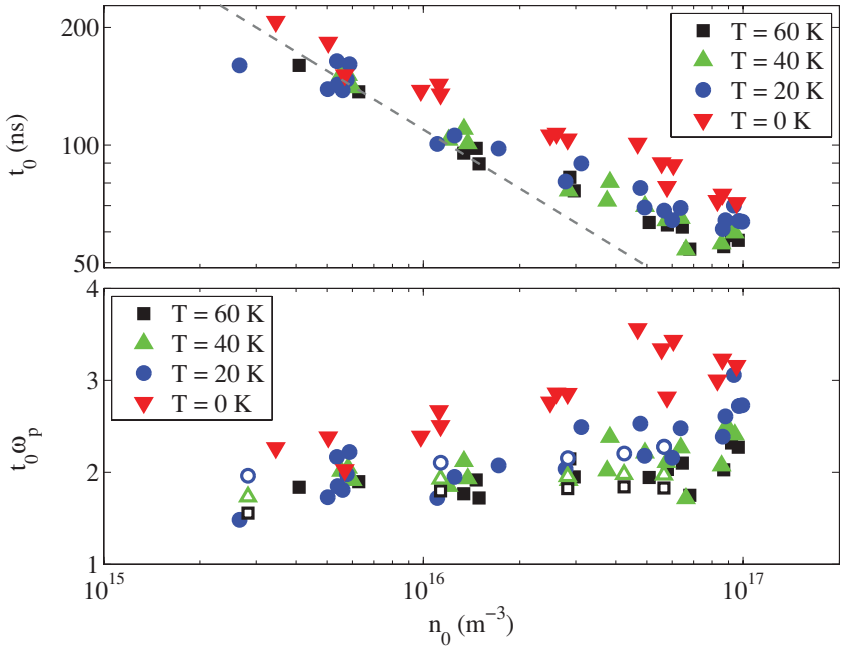

Figure 4.2 Experimental data. (Top) The time at which the DIH fluorescence peak occurs. The gray dashed line shows the expected time in the absence of screening effects. (Bottom) Scaled DIH peak time (data from the top panel) with t_0 corrected by Δt. Open symbols are from the simulation. This data would all fall on a flat line if there was no screening.

$n^{-1/2}$ scaling. The bottom panel of Fig. 4.2 shows the same effect more clearly, where the time has been scaled by the plasma frequency ω_p. In the absence of screening, we would expect all of the data to fall on the same horizontal line.

4.2.1 Comparison of simulated and experimental fluorescence data

To test our data analysis and better understand our experimental results, we used a computer simulation that solves the optical Bloch equations to give us a simulated fluorescence signal. The computer simulation, which was carried out by our colleague F. Robicheaux, allowed us to find the velocity distribution and ion temperature at early times. This MD simulation of Yukawa-shielded calcium ions started with the ions at rest, randomly positioned in a cell. The ions were allowed to

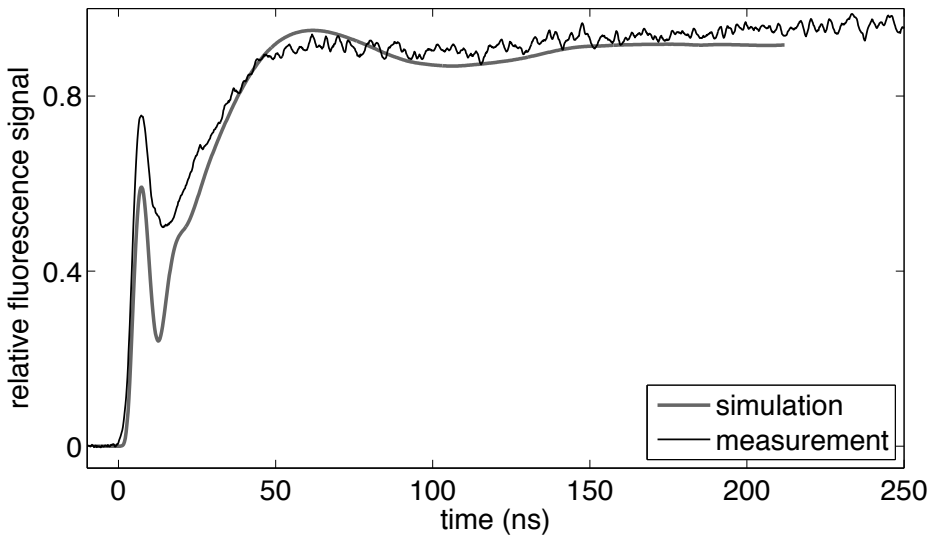

Figure 4.3 A comparison of the simulated fluorescence data (thick gray line) and the experimentally measured fluorescence (thin black line). Similar features are seen in both data sets, such as a heavily damped Rabi oscillation at early times, the DIH shoulder peak, and the broad background due to the plasma expansion. The density for these plots is $n_0 = 5(3) \times 10^{10}$ cm^{-3}.

move in the field generated by all of the other shielded ions in the cell (with wrapped boundary conditions). After several ω_{pi}^{-1}, the average ion kinetic energy was calculated and from this the ion temperature was determined. The result is given in Eq. (6) in Ref. [9]. Further details regarding the simulation can be found in Appendix B.

Comparing the results of the simulation for a range of densities with experimental data shows good agreement, as seen in Fig. 4.3. Similar features in both signals are clearly distinguishable, such as a heavily damped Rabi oscillation at early times and the DIH peak. Differences in the height of the signal can be attributed to inhomogeneities in the experimental setup.

Since the simulated and experimental data agree well, comparing the experimental data with the simulation allows us to connect the DIH time found from our fluorescence measurements to the velocity distribution. We would expect t_0 to occur at the same time that the rms velocity distribution reaches its first maximum. We find, however, that there is a small difference, Δt, that depends most

strongly on density. We have applied this correction, which is $\leq 15\%$, in the bottom panel of Fig. 4.2. The data clearly shows in both panels that the DIH time deviates from the expected $n^{-1/2}$ dependence as the temperature decreases and the density increases. Further research was needed to determine whether this deviation was an effect of electron screening on the ion motion during DIH, or whether it was related to Δt. We also found a factor of 2 discrepancy between the experimental and simulated densities, which may have to do with how we measure the density experimentally. In the comparisons between experimental and simulated data, the densities of the experimental data have been multiplied by this factor of 2.

4.3 Measuring the influence of electron screening on DIH

The models described in Sec. 4.1 suggest that the time scale for DIH is insensitive to electron screening, however the results summarized in Sec 4.2 indicate that the acceleration of the ions due to DIH depends more strongly on the density and temperature than predicted by the models. By going to colder electron temperatures and higher densities, which gives a smaller Debye length and thus greater electron screening, we were able to more carefully characterize the influence of electron screening on DIH for a wider range of κ than previously studied.

As explained in Sec. 2.2.3, changing the frequency of the probe laser beam allows us to map out the velocity distribution of the ions. The studies described in Sec. 4.2 relied on computer simulations to determine the ion velocity. For the measurements described in this section, we varied the frequency of our probe laser beam using an AOM, as described in Ref. [10]. We made measurements of the fluorescence signal at different electron temperatures and at different probe laser beam detunings in order to find the rms velocity of the ions and to determine the influence of electron screening on DIH. Sample data which shows the ion fluorescence at different probe laser beam detunings is shown in Fig. 4.4.

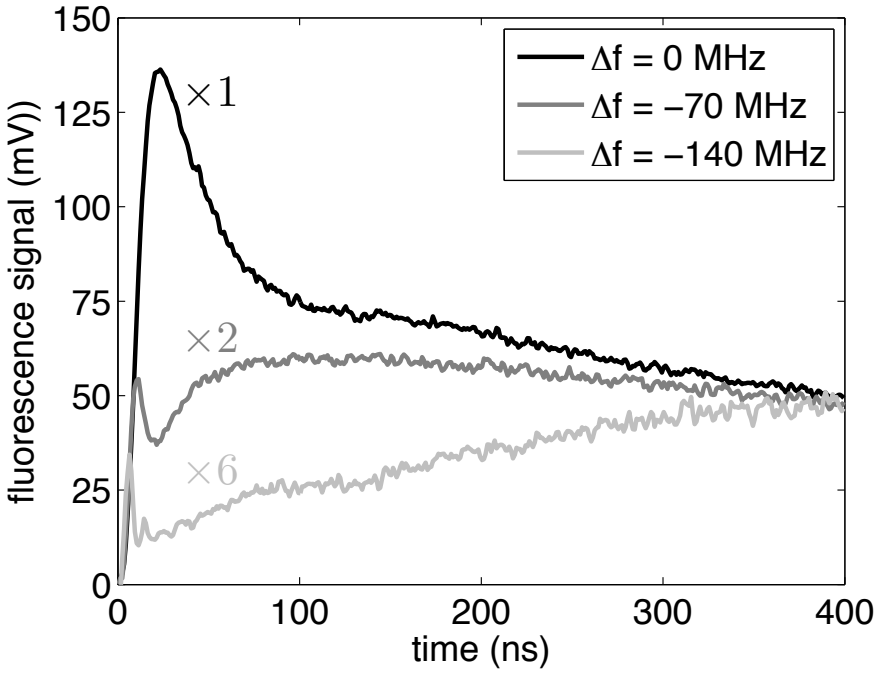

Figure 4.4 Fluorescence signals from an ultracold neutral calcium plasma. The density is $n_0 = 1 \times 10^{10}$ cm^{-3}, the intensity is $s_0 = 1.4$, and the probe laser beam frequency detunings are 0, -70, and -140 MHz. The -70 and -140 MHz data have been multiplied by 2 and 6 for clarity. Ground state ions begin to scatter light from the 397 nm probe laser beam and the signal rapidly increases during the first few ns. At non-zero probe laser beam detunings, a heavily damped Rabi oscillation appears in the signal. As the ion velocity distribution broadens due to DIH and plasma expansion, the fluorescence signals change. The fluorescence signal is a measure of the number of ions in the plasma that are Doppler shifted into resonance with the probe laser beam.

From fluorescence signals like the one shown in Fig. 4.4 we extracted the rms width of the velocity distribution as a function of time. As discussed in Ref. [22] the fluorescence lineshape is a Voigt profile. However, when the Gaussian width significantly exceeds the Lorentzian width, the lineshape is almost perfectly Gaussian. When the ion temperature equals T_c, the thermal velocity is $\sqrt{k_{\mathrm{B}}T_c/m_{\mathrm{i}}} = 28$ m/s. The natural width of the Ca^+ transition is 22 MHz. The ion velocity that produces a Doppler shift equal to this width is 8.7 m/s. Fitting the velocity distribution to a Gaussian instead of a Voigt profile somewhat overestimates the real ion temperature, however the data quality for these measurements did not allow us to use a Voigt profile fit. Nonetheless, even though the Gaussian fit overestimates the ion temperature, changes in the width of the distribution are easily measured, which was the primary objective of these measurements. The fluorescence data obtained was analyzed using the methods described in Ref. [10] and which, for the sake of brevity, are not reproduced here. The results of our analysis are shown in Fig. 4.5.

During the first 15 ns of the fluorescence signals, Rabi oscillations made it difficult to extract a meaningful velocity width. After these oscillations damp out, the rms velocity appeared to be more reliable. We can verify that the minimum width of the distribution corresponds to the correlation temperature, Eq. 1.10. The rms velocity at the correlation temperature is 28 m/s at our density of $n_0 = 1.0\times10^{10}\,\mathrm{cm}^{-3}$. The minimum width of our extracted velocity distribution of approximately 20 m/s agrees with this number.

At late times in the plasma expansion, the radial acceleration approaches zero and the expansion velocity approaches a constant value. In our measurements of the $T_e = 60$ K plasma, the width of the velocity distribution asymptotically approaches the value of 115 m/s. This is a close match to the expected value of $\sqrt{k_B T_e/m_i} = 111$ m/s. The velocity distribution shows a small oscillation at early times, which is the kinetic energy oscillation discussed in Sec. 1.3.2. This oscillation is shown in Fig. 4.6.

The top panel of Fig. 4.6 shows the width of the velocity distribution at early times. The dotted

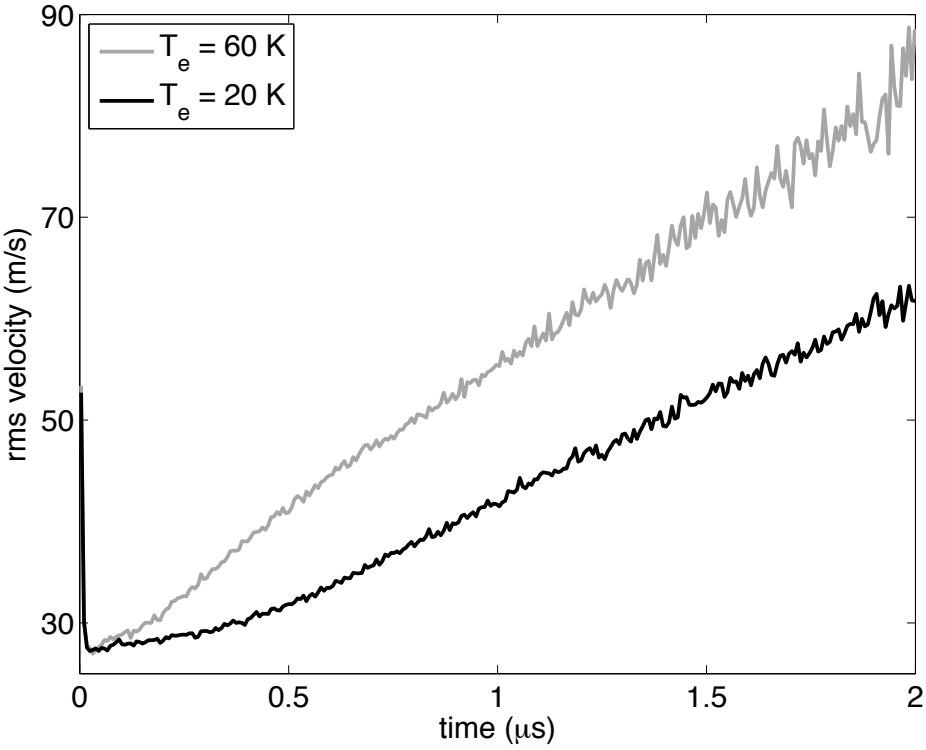

Figure 4.5 The rms width of the ion velocity distribution as a function of time in an ultracold calcium plasma. This data is extracted using a Gaussian fit. At early times this fit overestimates the width, however it reproduces changes in the distribution and that is the main objective in this graph.

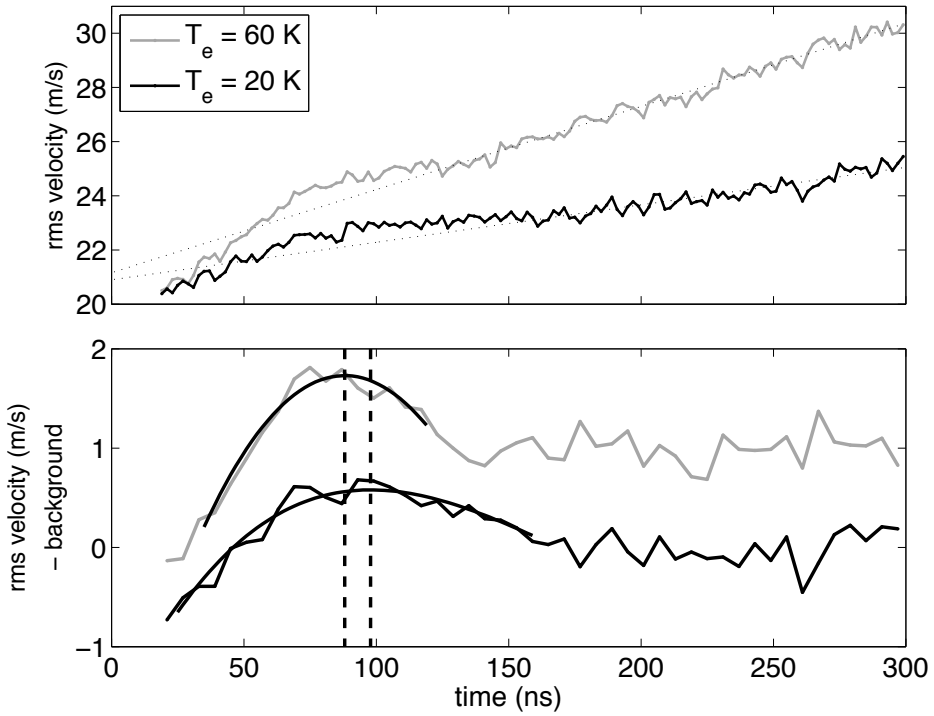

Figure 4.6 Top (panel): Velocity distribution at early times. Data for this plot was extracted from a subset of the fluorescence data, with probe laser detunings of 140 MHz and smaller, for initial electron temperatures $T_e = 20$ K and $T_e = 60$ K, and an initial plasma density of $n_0 = 1.0 \times 10^{10}$ cm^{-3}. An oscillation in the velocity distribution is visible above the background expansion, represented by the dotted line. Bottom (panel): The data in the top panel with the background expansion subtracted off. A third-order polynomial fit to the early time data is shown by the smooth solid black line. The maxima of these polynomial fits are shown by the vertical dashed lines. The $T_e = 60$ K data is offset vertically for clarity. As the electron temperature decreases, the DIH peak broadens and moves to later times.

line in the top panel of Fig. 4.6 is a fit that represents the plasma expansion. The bottom panel of Fig. 4.6 shows the width of the velocity distribution with the background expansion subtracted off. A vertical offset is included to distinguish between the data sets at the two different initial electron temperatures. A third-order polynomial is fit to the data near 100 ns. From the fits we were able to extract the time at which the DIH process broadens the distribution to its maximum value, which is equivalent to what we have called the DIH peak. The times at which the DIH peaks occurred are indicated by the dashed vertical lines. For an initial electron temperature of $T_e = 60$ K this DIH peak occurred at 88 ns. For an initial electron temperature of $T_e = 20$ K the peak occurred at 98 ns. For the lower temperature plasma the DIH peak was also broader, indicating that the equilibration rate was slower. These two effects are due to electron screening.

The effects of electron screening described by Eq. 4.9 should appear in the data plotted in the bottom panel of Fig. 4.6. As the initial electron temperature decreases from 60 K to 20 K, the value of κ increases from 0.54 to 0.93. This reduces the initial acceleration in Eq. 4.9 by 2.5%. In the bottom panel of Fig. 4.6 the characteristic DIH time, the time at which v_{rms} reaches its local maximum due to DIH, increases by $[(98\,\mathrm{ns}/88\,\mathrm{ns}) - 1] \times 100 = 11\%$. This indicates a reduction in the average acceleration by approximately the same amount.

4.4 The limit of ion strong coupling due to electron shielding

Improvements made to the metrology of our experiment that included using an external reference cavity, as described in Sec. 2.3.2, allowed us to take better fluorescence measurements of our ultracold plasmas. From our measurements we extracted the time evolving rms width of the velocity distribution by fitting the data to a Voigt profile. Using an expansion model, we found the electron and ion temperature as a function of time. By varying the initial electron temperature we generated plasmas with varying degrees of electron shielding and showed that we can generate plasmas

with very cold ions by mitigating the effects of DIH through electron shielding. We compared our experimental results to two molecular dynamics simulations, which showed good agreement with each other and with our data. We used theoretical considerations to extract the screened ion-ion potential energy in the plasma, the results of which suggest that although electron screening reduces heating due to DIH, it also reduces the nearest-neighbor potential energy in such a way that the ratio of potential energy to kinetic energy is independent of the electron temperature.

4.4.1 Mitigating the effects of DIH

Using the methods described in Chap. 2 we generated an ultracold plasma in a MOT and used laser-induced fluorescence to measure the ion fluorescence as a function of time for a range of probe laser beam offset frequencies from 0 to about ± 250 MHz. The data was fit to a Voigt profile, as described in Sec. 2.2.4, which allowed us to map out the ion velocity distribution as a function of time. Using the $v_{i,\mathrm{rms}}$ found from the Voigt fitting we were able to extract the ion temperature using the expansion model described in Sec. 1.3.3. This process was repeated for plasmas with different values of the electron temperature, which we varied by changing the wavelength of the ionizing laser. The experimental $v_{i,\mathrm{rms}}$ for a plasma with an electron temperature of $T_e = 50$ K and the expansion model are plotted in Fig. 4.7. It is clear from Fig. 4.7 that there is good agreement between the data and the model.

As the initial electron temperature decreases, the plasma expansion rate and ion thermalization rate changes. In Fig. 4.8 we plot the average $T_i = m_i v_{i,\mathrm{rms}}^2/k_B$ after the DIH process has completed. We also plot the characteristic DIH time for a range of electron temperatures. This characteristic time is taken to be the time when the ion temperature oscillation due to DIH is at its maximum. This can be seen in Fig. 4.7 at approximately 110 ns, where the measured $v_{i,\mathrm{rms}}$ (black line) passes slightly above the model (red dashed line). The electron and ion temperatures are both extracted from the expansion model given by Eq. 1.11. Plasmas with smaller T_e have smaller values of

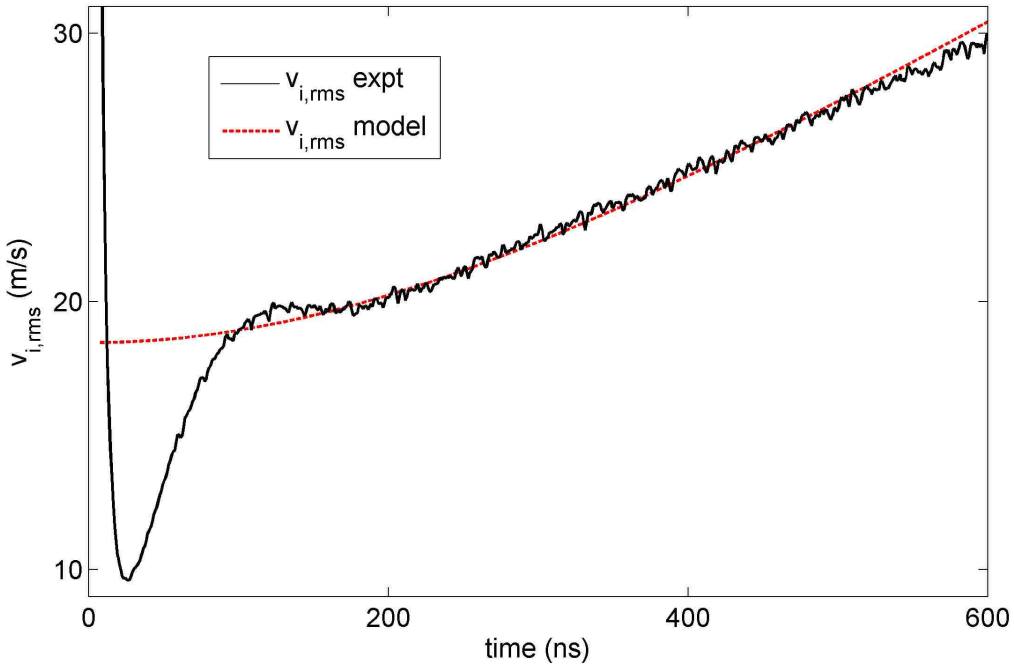

Figure 4.7 The time-evolving rms width of the ion velocity distribution for an ultracold calcium plasma at a density of approximately 0.9×10^{10} cm^{-3} and electron temperature of $T_e = 50$ K. The rms velocity width is found using a fit to a Voigt profile, where the Gaussian frequency width is extracted as a fit parameter and converted to the velocity width through the Doppler shift. The model described by Eq. 1.11 is plotted as the red dashed line. During the first 15 ns of the fluorescence signal, Rabi oscillations make it difficult to extract a meaningful velocity width. After these oscillations damp out, the rms velocity appears to be more reliable.

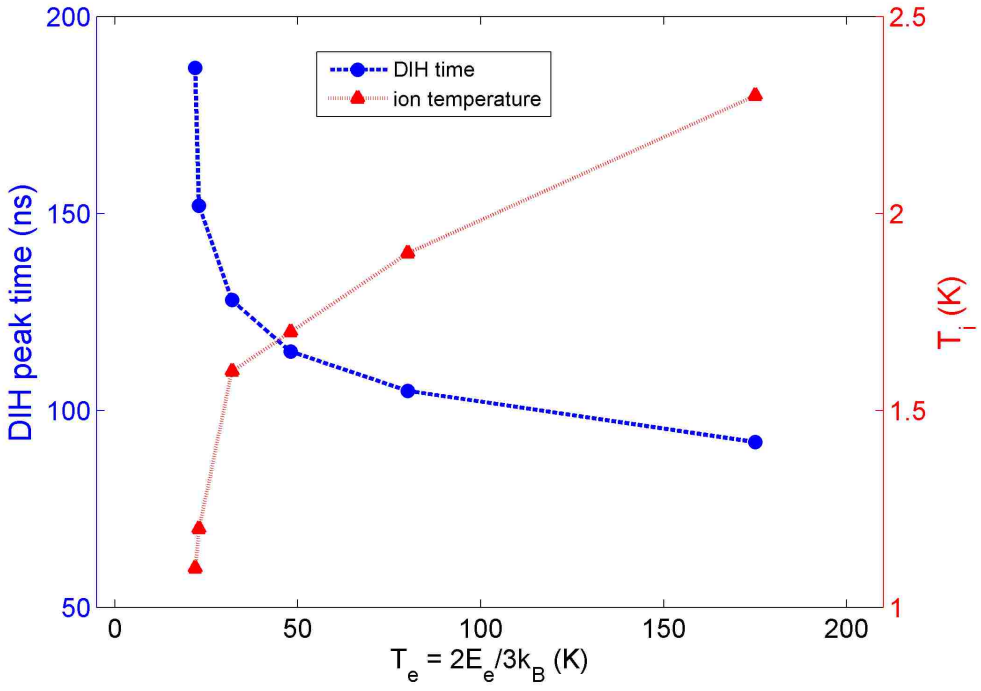

Figure 4.8 The equilibrium ion temperature after DIH (red triangles) and the characteristic DIH time (blue circles) plotted as a function of the electron temperature extracted from the expansion model. It is evident from this plot that electron screening reduces the ion temperature and extends the DIH time. The density for all these plasmas is approximately 0.9×10^{10} cm^{-3} and the inverse scaled screening length κ ranges from about 0.4 to 1.0.

T_i. The electron shielding length deceases with decreasing T_e, softening the ion-ion Coulomb interaction. As the ions move under the influence of the screened Coulomb force of the neighboring ions, they acquire less kinetic energy compared to the unscreened case.

As T_e decreases, the time scale for DIH increases. This confirms observations in Refs. [9, 10]. The low-temperature electrons more effectively shield ions from their nearest neighbors. The Coulomb force is reduced, and the ions take longer to reach their "equilibrium" positions. The data in Fig. 4.8 show that the DIH time is extended by as much as a factor of 2.

4.4.2 Comparison with models

Molecular dynamics simulations of complex neutral plasmas were published in the 1990's by Farouki, Hamaguchi, and Dubin [46–49]. Those simulations showed that electron shielding and correlation effects reduce the average electrical potential energy of the plasma ions. Murillo showed that these simulations can be applied to ultracold neutral plasmas [6]. A discussion of how that is done is given below.

Using Eq. 1.9 and the MD results of Hamaguchi et al. [46–49], we can predict the ion temperature after the DIH process has completed. This determination requires an iterative process because the ion temperature appears in the RHS of Eq. 1.9 in the u/Γ term [22]. One begins by choosing an initial ion temperature, density, and electron κ. From this the ion Γ can be calculated. The tables in Refs. [46–49] then give the value of u/Γ. This can be inserted into Eq. 1.9 which gives a new ion temperature. The process is repeated until the ion temperature and Γ converge to a self-consistent limit. The resulting Γ as a function of κ is plotted in red in Fig. 4.9. As κ increases, the Debye length λ_D becomes smaller. The electrons more effectively shield the neighboring ions from one another and the final DIH temperature decreases. The Γ vs. κ plot is a plot of $1/T_i$ vs. $1/\sqrt{T_e}$.

The MD simulations described in Sec. 4.2.1 and Appendix B are plotted as the blue dashed line in Fig. 4.9. The κ domain of this calculation is somewhat limited because the plasma becomes

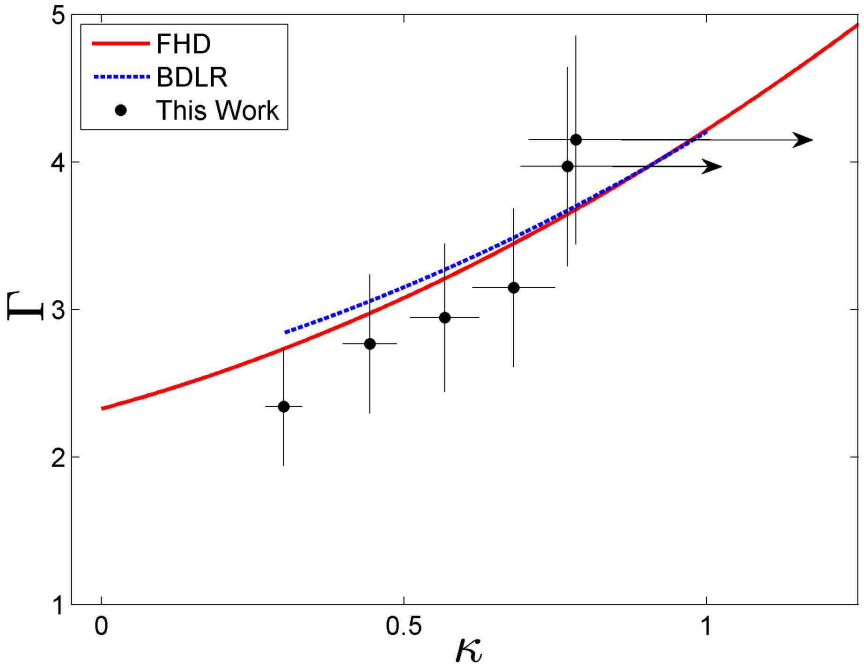

Figure 4.9 Theoretical and experimental plots of the coupling parameter Γ as a function of the electron screening κ. The red line is derived from MD simulations [46–49]. The dotted blue line is from the simulation described in Sec. 4.2.1 and Appendix B. The results of this work are also plotted as black circles with estimated error bars. The two rightmost experimental data points correspond to plasmas with low initial electron temperatures, as described in the text. Under these conditions, the model of Eq (1.12) tends to overestimate the electron temperature, as suggested by the arrows.

non-ideal when $\kappa > 1$ in the singly-ionized plasma used in the study, and under those conditions for that plasma it is not clear that the Yukawa approximation is valid. The excellent agreement between this result and the predictions based on Eq. 1.9 is readily apparent.

In Fig. 4.9 we also plot our experimental results. The experimental determination of the electron and ion temperatures is described in Sec. 1.3.3. There is excellent agreement between the experimental data and the two simulations described above. The rightmost experimental data point is measured in a plasma evolving from a Rydberg gas excited ≈ 10 cm^{-1} below the ionization potential. The second rightmost point corresponds to a plasma excited right at threshold. The expansion model we used to find the electron and ion temperatures for these two plasmas tends to overestimate the electron temperature at the very early times [37]. Thus we would expect the actual electron temperature to be lower, corresponding to larger values of κ, as suggested by the arrows in the plot.

The data in Fig. 4.9 demonstrate the validity of the assumptions used in deriving Eq. 1.9. The data show that electron screening substantially reduces the ion temperature, resulting in increased values of Γ_{ii}. Electron screening significantly mitigates the effects of DIH, which is the source of ion heating at these early times.

4.4.3 Screened potential energy vs. screened ion temperature

In non-neutral plasmas, the parameter Γ_{ii} completely defines the ion-ion interactions. However, in *neutral* plasmas, an ion-ion interaction necessarily includes contributions from the electrons. When the shielding length becomes comparable to the distance between ions, when $\kappa \to 1$, the relevance of Γ_{ii} is questionable.

One might be tempted to look at Eq. 1.7 and assume that the "effective" coupling constant is $\hat{\Gamma} = \Gamma_{ii}\exp(-\kappa)$. However, that would overestimate the influence of screening. For small κ, corresponding to the limit of weak screening, the first-order correction in that model would be

linear in κ. This is clearly not the case, as MD simulations show. For example, the ion temperature and density at the liquid-solid phase transition clearly has no linear term (see Fig. 1 in Ref. [48]).

The idea of calculating Γ_{ii} is somewhat problematic in neutral plasmas. The Γ parameter is supposed to represent the ion-ion nearest-neighbor potential energy divided by the ion temperature. The problem arises because the ions and electrons are also correlated, and Γ_{ei} becomes important. There is a potential energy associated with Γ_{ei} that is shared by both the electrons and the ions. Similarly, because the electrons follow the ions, there is also a Γ_{ee} term that becomes important and that will mimic the Γ_{ii} behavior. When trying to calculate the screened ion coupling parameter $\hat{\Gamma}$ it is not immediately clear which potential energy is appropriate to include in the calculation. They are all important and they all are connected to the ion density and temperature.

This distinction is important to make. The thermodynamic properties of non-neutral plasmas depend on Γ_{ii}. These properties can be translated into the realm of neutral plasmas with the idea that weak electron screening modifies them only slightly. However in ultracold neutral plasmas where $\kappa = 1$ is achievable, the Γ_{ii} scaling of these properties is not immediately clear. This is particularly the case when the Γ_{ii} is determined by κ, such as we show in Fig. 4.8.

In light of the fact that all of the electron and ion coupling parameters are important and interconnected, we can simply define $\hat{\Gamma}$ to be the total potential energy of the system divided by the kinetic energy of the ions. Taking U as the total potential energy and K to be kinetic energy of the ions, we write

$$\hat{\Gamma} = \frac{U_F}{K_F} = \frac{U_F}{U_I - U_F + K_I}, \tag{4.10}$$

where the conservation of energy is, trivially, $U_I + K_I = U_F + K_F$ and we have assumed that the electron temperature does not change from the initial to final state. Because the ions start out with mK temperatures, we can set $K_I = 0$. Summing up the contributions of the electrons and ions to the total initial potential energy gives $U_I = 0$. This can be seen in two ways. One is that the initial state is completely uncorrelated and neutral and therefore the total potential energy must be zero. The

other is to argue that the electron-ion potential energy terms are negative and exactly cancel the electron-electron and ion-ion potential energy terms. Either way, we end up with the conclusion that the magnitude of the screened coupling parameter is

$$\hat{\Gamma} = 1. \tag{4.11}$$

Even though electron screening reduces the ion temperature (see Fig. 4.8), it reduces the potential energy by exactly the same amount so that the ratio of potential energy to kinetic energy is always 1.

This result, Eq. 4.11, is true for all neutral systems in which there is no external source of heat for the electrons and when there is no correlation in the initial state. The agreement between the experimental data and MD simulations in Fig. 4.8 suggest that three-body recombination and electron-Rydberg scattering have not significantly increased the electron temperature at these early times, because those heating terms are not included in the MD simulation. If the electrons are heated, then the potential energy U_F in Eq. 4.10 goes down and $\hat{\Gamma}$ will increase.

We note that the final state of the plasma cannot be completely determined by energy conservation alone because of the two-temperature nature of the ultracold neutral plasma. For a given initial energy, there are many possible values of the final temperatures T_e and T_i that correspond to a correct final energy, at least in principle. Of course, if a true equilibrium state could be reached, the plasma would have $T_i = T_e$ and the final state would be deterministic. This suggests that more work on the quasithermodynamics of two-temperature plasmas is warranted [50, 51].

Chapter 5

Increasing the strong coupling in a Ca^{2+} plasma

Disorder-induced heating is an ultrafast, nonequilibrium dynamical process that results from a sudden shift in the energy landscape of the system. In Ref. [52] Murillo suggests that inducing such a shift in the energy landscape can produce interesting ultrafast processes in a variety of systems, ranging from biological systems to intrinsically quantum systems. An example of such a process is the rapid photoionization of atoms in a MOT to produce an ultracold neutral plasma, which very nearly approximates the instantaneous transition of an ideal gas into a strongly coupled state. Ref. [52] uses MD simulations to investigate the ultrafast dynamics that occur at early times in the plasma evolution that give rise to processes such as DIH and oscillations in the kinetic energy. Murillo suggests that shifting the energy landscape of the plasma ions again could be used to probe the conditions of the plasma at different times in its evolution. One way to dramatically and nearly instantaneously alter the energy landscape of the ions is to promote them to higher ionization states using a second set of laser pulses. The MD simulations show that if the second ionization is timed to coincide with the peak of the kinetic energy oscillation that minimal additional heating of the

plasma ions will occur. Thus it should be possible to increase the strong coupling of an ultracold plasma by exciting the ions to higher ionization states.

The following section provides a theoretical framework for an experiment in calcium that was designed and implemented to increase the strong coupling of an ultracold plasma by doubly ionizing the plasma ions. Also included is a summary of the MD simulations found in Ref. [52]. A description of basic modeling using rate equations is included in Sec. 5.2. Our experimental methods are described in Sec. 5.3 and an explanation of our analysis is given in Sec. 5.4. Our experimental results are described in Sec. 5.5.

5.1 Theoretical background

Interactions in complex many-body systems can be described by the multidimensional potential energy function U [53]. Different configurations of the system correspond to local minima in U, or, in other words, the "topology" of the energy landscape. For ultracold neutral plasmas, the initial state is the neutral atom system, which has a "topologically flat" energy landscape corresponding to $U = 0$ [52]. After the atoms are ionized, the energy landscape of the plasma can be very complex, with the excess potential energy now governing the dynamics of the system. A model Hamiltonian for the ions can be constructed of the form

$$\mathscr{H} = \sum_{j=1}^{N} \frac{p_j^2}{2M} + U(\mathbf{r}_1, ..., \mathbf{r}_N), \tag{5.1}$$

which is Eq. (1) in Ref. [52].

The MD simulations which motivate this work solve the equations of motion associated with Eq. 5.1, where U is modeled as a Yukawa potential. The simulations model the plasma dynamics on short time scales using an expansion of the Liouville equation that conserves energy to $\mathscr{O}(t^2)$. The details regarding this procedure can be found in Ref. [52], but are not relevant here. The important result in the context of this thesis is that at early times the plasma dynamics are dominated by

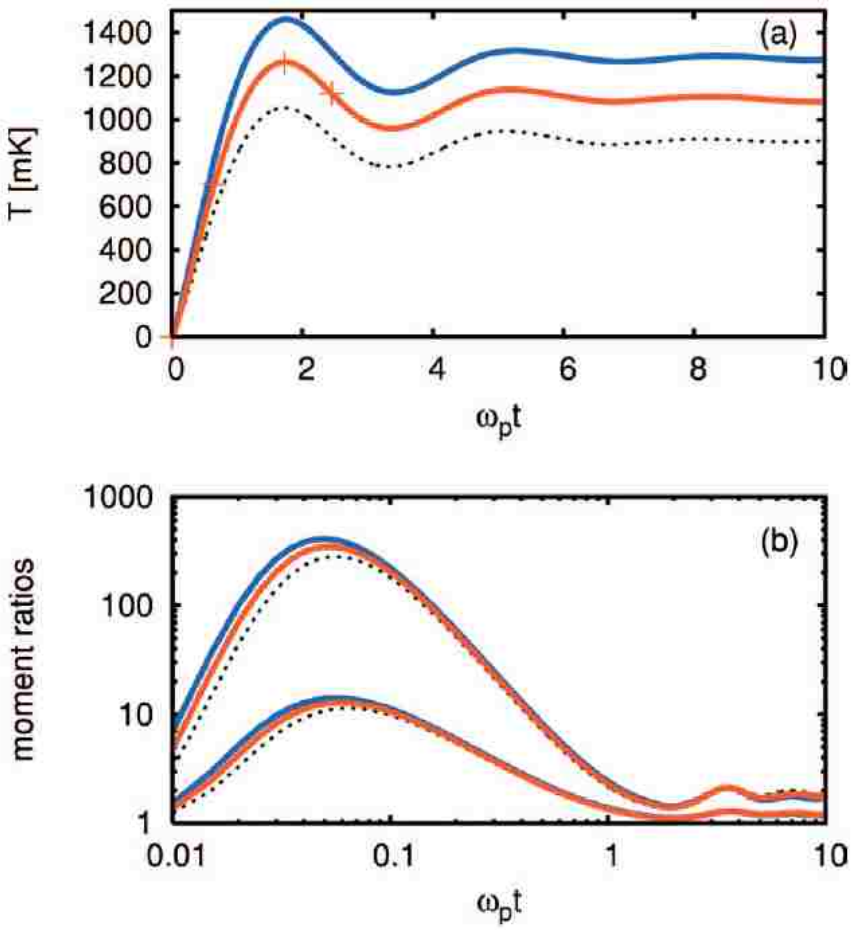

Figure 5.1 Top panel: Simulated ion temperature as a function of time for the intermediate-time dynamics of an ultracold neutral plasma for different values of κ. Oscillations in the kinetic energy, like those discussed in Sec. 1.3.2, are clearly visible. Bottom panel: Ratios of the moments of the velocity distribution. The strong deviation of the ratios from unity during the first plasma period (ω_{pi}^{-1}) indicate that the distribution is non-Maxwellian. The ratios quickly approach unity after the conclusion of the DIH phase [52].

nearest-neighbor interactions and that the dominant forces are almost entirely Coulomb forces.

Simulations that model the intermediate-time dynamics are shown in Fig. 5.1. The top panel shows how the ion temperature changes in time for different values of the inverse scaled screening length κ. The kinetic energy oscillations discussed in Sec. 1.3.2 are clearly visible in the sim-

ulations. As previously mentioned, these oscillations arise because ions, under the influence of DIH, initially move coherently to minimize their potential energy. However the inertia of the ions causes them to overshoot their equilibrium positions before reversing directions. The visibility of the first kinetic energy oscillation over those that occur later in time is due to coherence. All the ions undergo this motion on the same time scale, which is approximately equal to $\omega_{pi}t = 1$. The oscillations appear damped at later times because the random spatial distribution of the ions in the initial state breaks perfect coherence. This is also the reason that the temperature does not return to its initial value after one oscillation.

The MD simulation also provides information about the moments of the velocity distribution. The bottom panel of Fig. 5.1 shows two different moment ratios for plasmas with different values of κ. For a purely Maxwellian distribution the moment ratios would be unity. The significant deviation from unity of the plots in the bottom panel of Fig. 5.1 clearly indicate that the velocity distribution during the DIH phase of the plasma is non-Maxwellian. However the plasma, having undergone DIH, quickly approaches a quasiequilibrium state on the time scale of the plasma period ($\sim \omega_{pi}^{-1}$), which is indicated in the bottom panel of Fig. 5.1 by the moment ratios approaching unity after one $\omega_{pi}t$.

It is also interesting to consider the pair correlation function $g(r,t)$ at different times in the early evolution of the plasma. The MD simulations of Ref. [52] also calculate $g(r,t)$ for the times marked by crosses in the top panel of Fig. 5.1, which occur when the plasma is formed, during the DIH phase, at the peak of the kinetic energy oscillation, and after the ions have overshot their equilibrium positions. The calculated pair correlation function for these different times is plotted in Fig. 5.2 as a function of the ratio of the distance to the Wigner-Seitz radius. The early times are plotted in red and blue, and the latest time is plotted in magenta. The most interesting plot in the context of this discussion, however, is the $g(r,t)$ plotted for the time corresponding to the peak of the kinetic energy oscillation (black dotted line). The pair correlation function has an equilibrium-

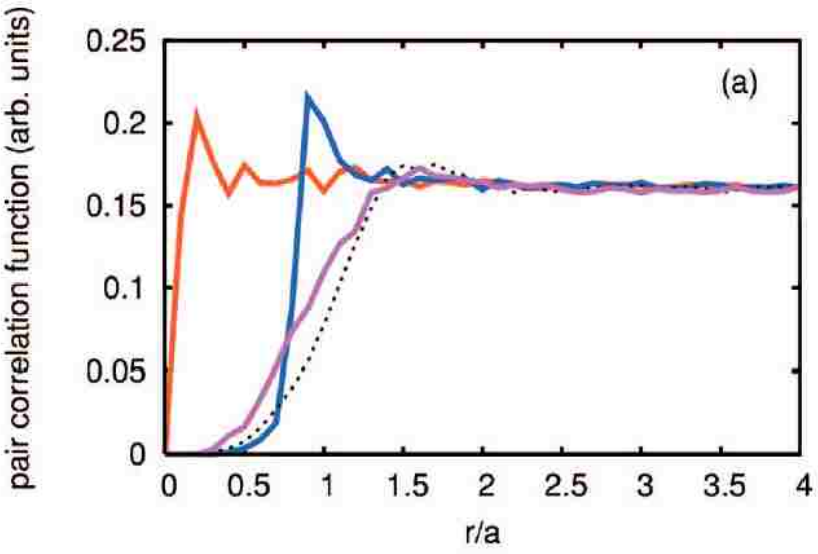

Figure 5.2 The pair correlation function $g(r,t)$ as a a function of r/a_{ws}. The red and blue plots show the pair correlation function at times earlier than the oscillation in the kinetic energy, indicated by the first two markers in the top panel of Fig. 5.1. The magenta plot corresponds to $g(r,t)$ at times after the kinetic energy oscillation. The pair correlation function for the system at the peak of the kinetic energy oscillation is plotted as the dotted black line. It has an equilibrium-like form, indicating that the system is more spatially ordered at this time than at other times in the plasma evolution [52].

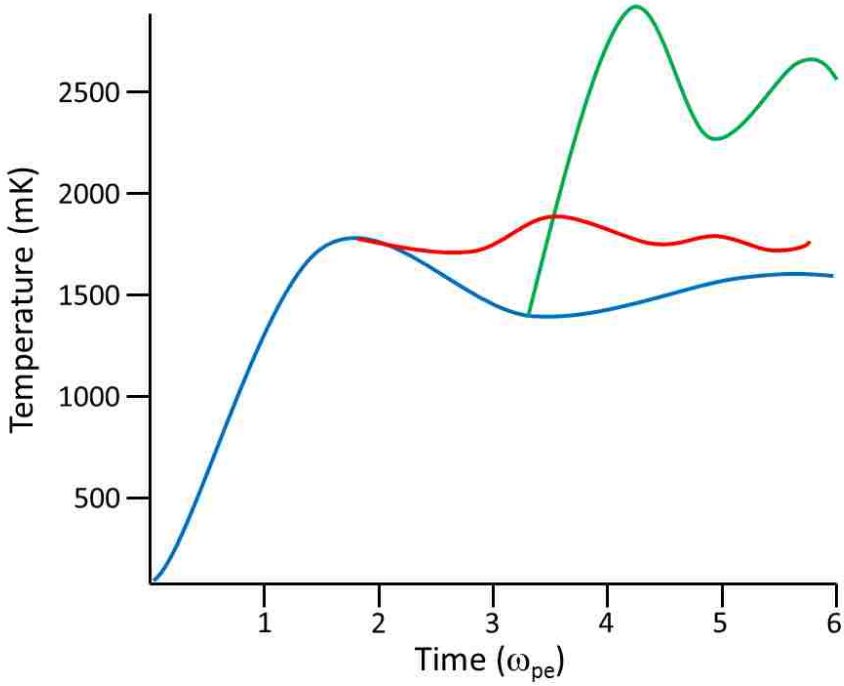

Figure 5.3 The simulated ion temperature versus the timing of the second ionization. After the plasma is created, the ion temperature rises as the ions undergo DIH and move to minimize their potential energy. The blue plot simulates the ion temperature if the system is not ionized again. The red plot shows that ionizing the plasma again at the height of the kinetic energy oscillation peak does not change the ion temperature. The green plot illustrates that if the plasma is ionized again at some later time, the ions will undergo a second DIH phase and the ion temperature will increase [52].

like form, which tells us something about the spatial ordering of the system, namely that the peak of the kinetic energy oscillation corresponds to the highest degree of spatial ordering.

Perhaps the most important plot from Ref. [52], at least in the context of this thesis, is the one reproduced in Fig. 5.3. This plot shows the simulated ion temperature as a function of time for a doubly ionized plasma. It is suggested in Ref. [52] that an experimental diagnostic of certain properties, such as the pair correlation function, during the early evolution of the plasma would be to induce a second sudden modification to the energy landscape. Such a shift can be achieved by promoting the plasma ions to a higher ionization state. The plot in Fig. 5.3 shows three curves that correspond to no second ionization (blue), ionization at the peak of the kinetic energy oscillation

(red), and ionization after the kinetic energy oscillation (green). If the plasma is doubly ionized after the kinetic energy oscillation, when the ions have reached a local minimum in their kinetic energy, corresponding to the local maximum in their potential energy, the plasma will undergo a second DIH phase. However, if the plasma is ionized again at the height of the kinetic energy oscillation, which corresponds to a minimum in the potential energy and the greatest spatial ordering, the system will not undergo additional heating due to DIH. Doubling the ion charge ($Z = 2$) quadruples the nearest-neighbor potential energy. Recalling from Eq. 1.2 that strong coupling is defined as the ratio of the nearest-neighbor potential energy to the average kinetic energy, quadrupling the potential energy while leaving the kinetic energy unchanged would increase the strong coupling of the system by a factor of four.

5.2 Modeling the second ionization

Rate equation models can be used to describe the dynamics of energy level populations in a system influenced by incident light fields. The rate equations are a set of differential equations that describe the evolution of the system in time. We used rate equations to help us understand how the energy level populations of the ions changed over a range of initial conditions in the Ca^{2+} experiment, with the specific goal of determining the conditions necessary to achieve 100% double ionization of the plasma. This is important, because the ability to quadruple Γ depends on being able to completely doubly ionize our system.

The following rate equations were used in the model:

$$\begin{aligned}
\frac{dN_1}{dt} &= -P_1N_1 + \Gamma_{10}N_2 + P_1N_2 \\
\frac{dN_2}{dt} &= P_1N_1 - \Gamma_{10}N_2 - P_1N_2 - P_2N_2 + \Gamma_{21}N_3 + P_2N_3 \\
\frac{dN_3}{dt} &= P_2N_2 - \Gamma_{21}N_3 - P_2N_3 - P_3N_3 \\
\frac{dN_4}{dt} &= P_3N_3. \qquad (5.2)
\end{aligned}$$

The term N_1 refers to the population in the first energy state, i.e., the Ca^+ ion ground state. The second and third energy states are N_2 and N_3, respectively, and the term N_4 refers to the final state of the ion, i.e., the Ca^{2+} ground state. We consider transitions between levels only through radiative processes: absorption, spontaneous emission, and stimulated emission. A detailed explanation of these processes can be found in almost any book that deals with fundamental principles of laser science or atomic spectroscopy and will not be reproduced here. It is sufficient to say that the spontaneous emission rate, indicated in the above equations by Γ_{10} and Γ_{21}, is the reciprocal of the radiative lifetime of the excited state τ (in the absence of any other decay branches) and that the spontaneous emission rates for the relevant transitions in the Ca^+ ion were obtained from Ref. [54]. The terms P_1,P_2, and P_3 refer to the pumping rate, which is the rate at which we excite the ions to a higher energy level with the laser pulses. The pumping rate is equal to the stimulated emission rate. The time dependence of these equations is embedded in the pumping rate, since we assume a Gaussian form for the laser pulses.

The coupled differential equations in Eq. 5.2 are solved for a set of initial conditions. The timing of the second ionization pulses, relative to each other and to the first ionization, can be set, as well as $s_0 = I/I_{\text{sat}}$. The pulses are Gaussian in time, and the pulse duration is 3 ns full width at half maximum (FWHM). Initially all the ions are in N_1. The Γ_{10} and Γ_{21} depend on the energy levels that are being excited. In our case, these correspond to the $4s\,^2S_{1/2} \rightarrow 4p\,^2P^{\text{o}}_{1/2}$ transition at 397 nm and the $4p\,^2P^{\text{o}}_{1/2} \rightarrow 5d\,^2D_{3/2}$ transition at 210 nm (see Fig. 2.1).

Results from the model are shown in Fig. 5.4 for $s_0 = I/I_{\text{sat}} = 50$ for all three laser pulses, with all the pulses overlapped in time. Without taking into consideration other non-radiative processes that may effect the level populations, the model shows that it should be possible to completely doubly ionize the plasma. It also indicates that the complete conversion to Ca^{2+} depends strongly on the timing of the pulses and on the intensity, which needs to be several times the saturation intensity.

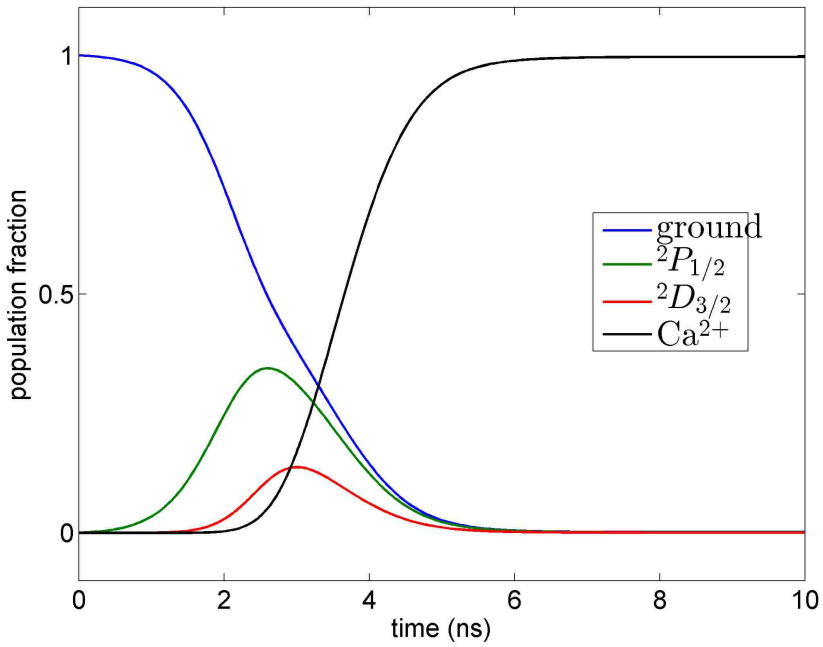

Figure 5.4 Changes in the level populations as a function of time for the Ca^+ ground state (blue), $4p\,^2P^o_{1/2}$ state (green), $5d\,^2D_{3/2}$ state (red), and the Ca^{2+} ground state (black). The system evolves in time according to the coupled differential equation found in Eq. 5.2. This simple model suggests that under the right conditions we can achieve 100% second ionization efficiency.

A very simple calculation can be used to find the power needed to saturate the transition. The saturation intensity is given by

$$I_{\text{sat}} = \frac{\pi hc}{3\lambda^3 \tau}, \tag{5.3}$$

where h is Plank's constant, c is the speed of light, λ is the wavelength of the transition, and τ is the lifetime of the excited state. For the 397 nm transition, $I_{sat} = 46$ mW/cm^2, and for the 210 nm transition $I_{sat} = 690$ mW/cm^2 (because the 210 nm is only a 50% branch). We can find the energy per pulse at the saturation intensity by multiplying I_{sat} by the pulse duration, which is 3 ns. If, for simplicity's sake, we assume that the cross-sectional area is 1 cm^2, then the pulse energy required to saturate the 397 nm transition is 0.14 nJ and the 210 nm transition is 2.0 nJ. In reality the required pulse energy is even less, because our pulses are focused down to an area much smaller than 1 cm^2. Based on these simple calculations, we should have no problem saturating the bound transitions.

5.3 Methods

A brief description of the Ca^{2+} experiment is included in Sec. 2.1.2. This section will describe the development of the Ca^{2+} experiment in greater detail and will include additional information about our experimental methods.

5.3.1 Timing and spatial alignment of ionizing pulses

The model described in Sec. 5.2 reveals that the second ionization efficiency also depends on the timing of the five ionizing laser pulses. We use a pulse generator to externally trigger the Nd:YAG lasers that pump the dye cells. A combination of electronic delays (from the pulse generator) and mechanical delays (from changing the physical path length of the laser pulses) allows us to overlap the first ionization pulses (423 nm and 390 nm) in time relative to each other and overlap the second ionization pulses (397 nm, 210 nm, and 355 nm) relative to each other to within 1 ns.

All five ionizing pulses overlap spatially in the region of the MOT. The 423 nm and 390 nm pulses are co-propagating and enter the MOT chamber through a window set at Brewster's angle. The 397 nm, 210 nm, and 355 nm pulses enter the vacuum chamber also through a Brewster window, but counter-propagating the first ionization pulses. The alignment is optimized by maximizing the depletion of the measured 397 nm probe laser fluorescence after the second ionization pulses arrive. We see depletion in the fluorescence signal because doubly ionizing some of the ions reduces the number of Ca^+ ions that interact with the probe laser beam. The fluorescence also drops because the 355 nm ionizing pulse imparts enough kinetic energy to the electrons to heat the plasma, which causes the plasma to expand radially more quickly and drives the ions out of resonance with the probe laser beam, due to the Doppler shift.

5.3.2 Ca^{2+} detection and measuring the second ionization fraction

Our first measurements of the Ca^{2+} ions were with a channeltron detector. A channeltron is used to detect charged particles and amplify the charged particle signal by means of an electron avalanche process. A single charged particle strikes an electrode, which results in one or more electrons being emitted. The electrons are accelerated by an electric potential between the first metal plate and a second, which results in the emission of additional electrons from the second metal plate. This process is repeated several times until the resulting current can be measured. Channeltron detectors make it possible to measure signals even when there are very few incident charged particles. Unlike a microchannel plate detector (MCP), however, charged particle detection using a channeltron detector does not provide spatial resolution.

In our experimental apparatus, mesh grids are situated above and below the region of the trap center. Voltages can be applied to these grids to create an electric field that accelerates the ions upwards, towards a conducting metal plate called the "pusher." A large positive voltage is applied to the pusher, which repels the ions and redirects them towards the channeltron detector. The first

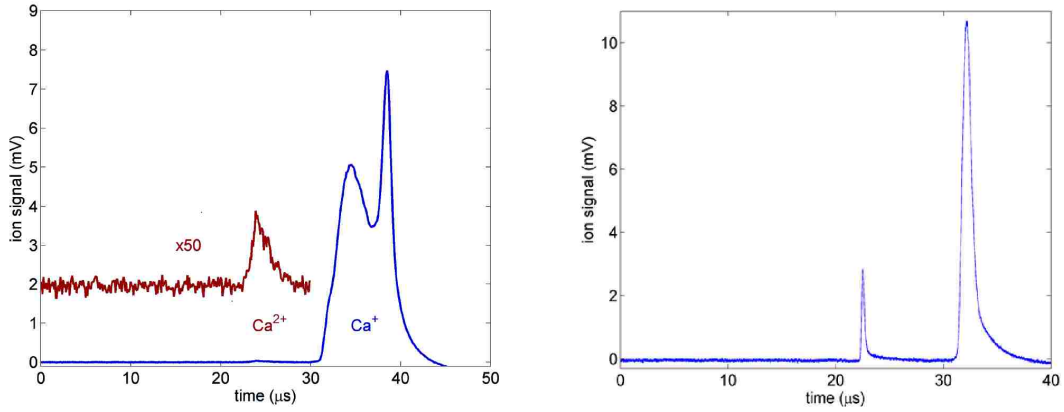

Figure 5.5 Early measurements of Ca^{2+} ions. Due to the difference in their charge state, the Ca^{2+} ions will arrive sooner than the Ca^{+} ions by a factor of $\sqrt{2}$. Improvements to the experimental apparatus allowed us to improve the second ionization efficiency, as can be seen by comparing the Ca^{2+} signals in the left and right plots. The channeltron detector proved able to detect the presence of Ca^{+} and Ca^{2+} ions, but could not provide an accurate measure of the second ionization fraction.

measurements of Ca^{2+} ions are shown in Fig. 5.5 (left). For a given potential difference across the voltage grids, it can be shown that the Ca^{2+} ions, due to their charge state, will arrive at the channeltron sooner than the Ca^{+} ions by a factor of $\sqrt{2}$. Thus the first signal in both plots in Fig. 5.5 is the signal due to the Ca^{2+} ions.

The appearance of what seems to be a double peak in Ca^{+} ion signal in the left plot in Fig. 5.5 is attributed to density effects. The difference between the second ionization fraction in the left plot as compared to that of the right plot is apparent. As we continued to improve the second ionization efficiency, however, it became clear that while the channeltron is a good measure of the presence of Ca^{+} and Ca^{2+} ions, it is not a good measure of the second ionization fraction. The reasons for this are still not well understood.

In order to estimate the second ionization fraction, we use the integrated ion signal. When we fit the fluorescence data to a Voigt profile, as described in Sec. 2.2.3, we fit for the amplitude of the distribution in addition to the Gaussian width. This amplitude depends on properties inherent

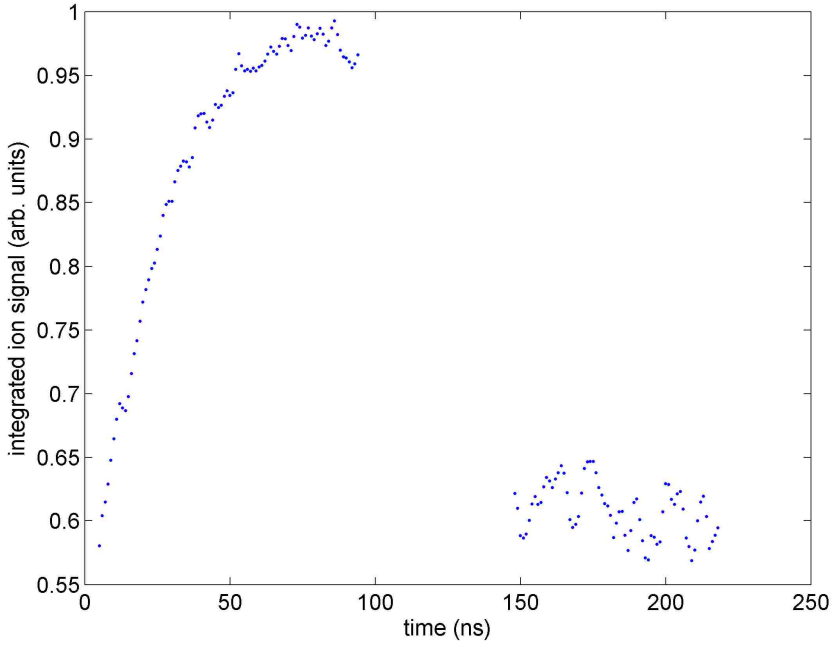

Figure 5.6 Sample data of the integrated ion signal, obtained from fitting the amplitude of the Voigt profile to fluorescence measurements. In this plot the data has been normalized to 1. The drop in the signal around 100 ns corresponds to the timing of the second ionization laser pulses. The drop occurs because the second ionization depletes the number of ions able to interact with the fluorescence probe laser beam.

to the PMT (counting efficiency, quantum efficiency, gain, etc.), the time interval over which data is collected, probe laser power, and the first excited state fraction. Only the excitation efficiency is expected to change, since converting some of the Ca^{+} ions into Ca^{2+} depletes the excited state and therefore reduces the amplitude of the signal. Thus using the integrated ion signal we are able to estimate the second ionization fraction, which ranges from 15-50%. The experiment typically operates at approximately 30% second ionization.

We can change the second ionization fraction by adjusting the power of the 355 nm laser pulse, up to a maximum of 50% conversion from Ca^{+} to Ca^{2+}. At 50% conversion, however, the heating of the electrons due to the ionizing pulse is too significant to allow for an accurate extraction of ion temperature using the Voigt fitting. In this laser configuration our second ionization fraction is

probably limited by the AC Stark shift.

5.3.3 Measuring Ca^+ ion fluorescence

We probe the Ca^+ velocity distribution using laser-induced fluorescence at 397 nm, as described in Sec. 2.2.3. The frequency is fixed by locking the laser to a partially stabilized frequency comb in the fundamental (see Sec. 2.3.4). The doubled light is then collimated to a diameter of 4 mm, attenuated to .5 mW, aligned to spatially overlap the plasma, and retroreflected. Fluorescence photons at this same wavelength are collected as a function of time after the plasma is generated using a 1 GHz bandwidth photo-multiplier tube and digital oscilloscope. The probe laser frequency can be smoothly and systematically scanned in 20 MHz intervals for $\pm$200 MHz from line center.

5.4 Analysis

To extract the time evolving ion velocity $v_{i,\mathrm{rms}}$, we use the same method described in detail in Sec. 2.2.3, which is to fit the fluorescence data to a Voigt profile. Assuming that the probe laser beam intensity is well below the saturation intensity of the transition and pressure broadening can be neglected, the Lorentzian contribution is given by the natural linewidth of the transition and is fixed at 22 MHz. Broadening of the lineshape is therefore due to Doppler broadening. The Gaussian width can be extracted as a fit parameter and is connected to the velocity of the ions through the Doppler shift. This allows us to map out the width of the ion velocity distribution as a function of time.

Figure 5.7 shows the experimental $v_{i,\mathrm{rms}}$, found by fitting the fluorescence to a Voigt profile, for a singly ionized plasma (solid gray line) and for a set of partially doubly ionized plasmas. The black data is for a plasma that was doubly ionized 20 ns after plasma creation, the blue data for a plasma doubly ionized 40 ns after creation, and so forth. The gaps that appear in the data occur at

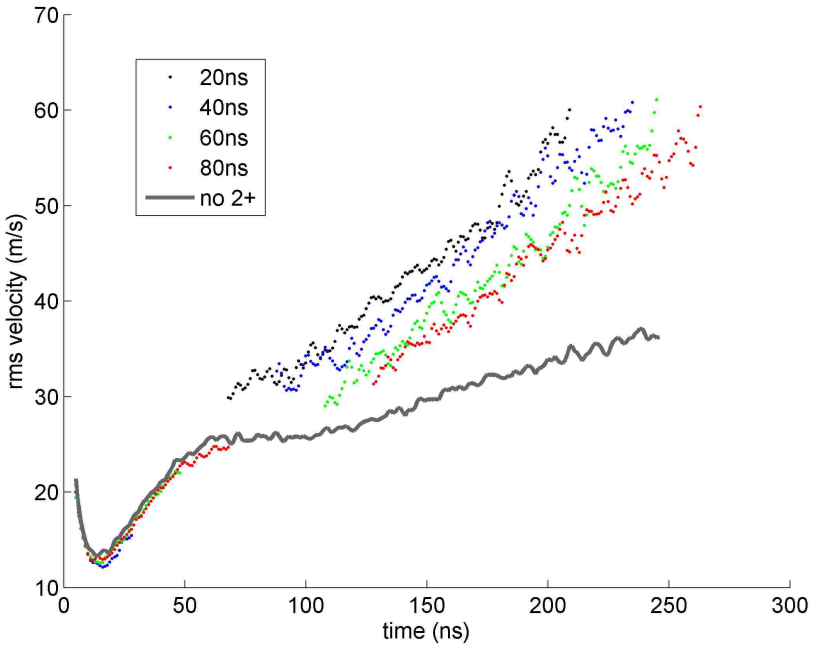

Figure 5.7 The rms velocity of ions in a singly ionized plasma (solid gray line) and of the Ca^+ ions in plasmas that have been partially doubly ionized. The four different plots correspond to different timings of the second ionization laser pulses. The gaps in the data for the partially doubly ionized plasmas occur at the time in which the second ionization pulse arrives. Scattered light and fluorescence from the 397 nm pulse make it impossible to do the Voigt fitting and extract a meaningful velocity width.

the time in which the second ionization pulses arrive, when fluorescence from the 397 nm pulse and scattered light make it difficult to extract a meaningful velocity width from the fluorescence measurements.

After some fraction of the Ca^+ ions are converted to Ca^{2+}, the combined ion system will equilibrate again. The ion velocity distribution is then comprised of contributions from the expansion of the original ion system as well as that of the Ca^{2+} system. We isolate the contribution to the ion velocity that arises from the second ionization by subtracting off the expansion of the original Ca^+ system that we obtain from the model (red dashed line in the lower plot in Fig. 5.8). We identify the time at which the second ionization laser pulses arrive as the new "zero" of time. We use the expansion model described by Eq. 1.12 and fit it to the data to find the initial ion and electron temperatures. The initial T_i calculated in this way is the additional heating from the second ionization. We can verify that the fits are good by adding back in the expansion of the Ca^+ plasma to the fit obtained for the partially doubly ionized plasma. This fit is given by the red dashed line in the upper plot in Fig. 5.8.

5.5 Results

The change in the ion temperature due to the second ionization is shown in Fig. 5.9, plotted as a function of $\omega_p t$. The black dotted line is a guide for the eye. The data shows that the change in the ion temperature is minimized near $\omega_p t \sim 2$, where the first kinetic energy oscillation peak occurs in the simulation shown in Fig. 5.3.

The uncertainty in our measurements is plotted as well. The biggest source of error is uncertainty in the timing of the second ionization pulses relative to the first ionization. Other sources of uncertainty are variability in laser power, density, and electron temperature.

The data shows that minimal heating occurs when the plasma is doubly ionized at the peak of

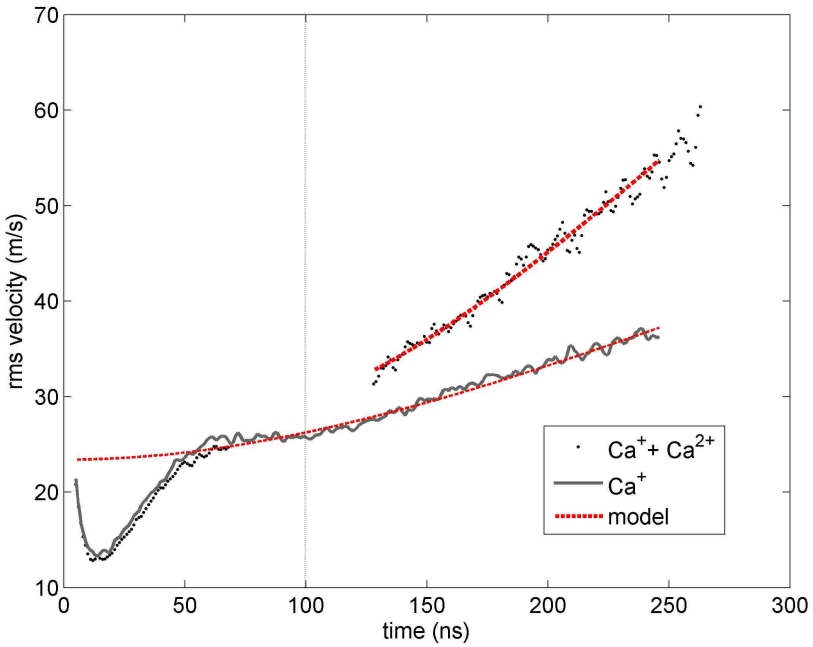

Figure 5.8 The rms velocity width of Ca^+ ions in a singly ionized plasma (solid gray line) and a partially doubly ionized plasma (dotted black line). The second ionization pulses arrive 100 ns after the plasma is formed (vertical line), and the density is approximately 2.4×10^{10} cm^{-3}. Fluorescence measurements are fit to a Voigt profile, where the Gaussian frequency width is extracted as a fit parameter and converted to the velocity width through the Doppler shift. The model described by Eq. (1.11) is plotted as the red dashed line.

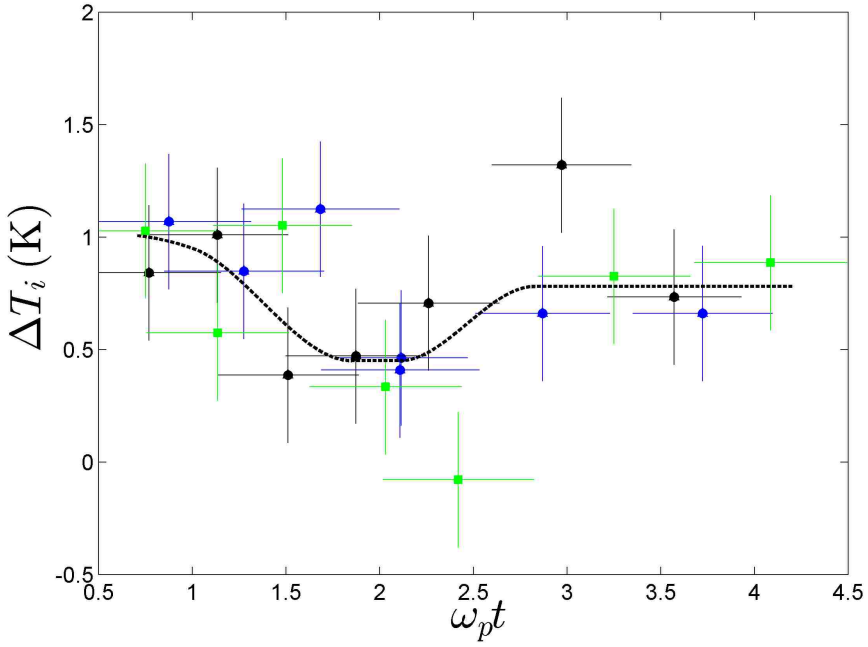

Figure 5.9 The change in the ion temperature due to the second ionization plotted as a function of the scaled time for three different plasmas. Each point corresponds to a different timing of the second ionization pulses. The dotted black line is a guide for the eye. This figure shows that the heating of the ions due to the second ionization depends on the timing of the second ionization. The heating is minimized when the second ionization pulses arrive at the peak of the kinetic energy oscillation, which confirms predictions made by MD simulations, as described in Sec. 5.1.

the kinetic energy oscillation and that, within the error bars, this heating is in fact zero, as predicted by simulations. Given that the second ionization fraction is typically only 30%, we would expect there to be some heating due to the equilibration of the Ca^{+} ions with the Ca^{2+} ions. The fact that we do not see this heating suggests that we are achieving 100% conversion from Ca^{+} to Ca^{2+} in 30% of the plasma, rather than 30% conversion over the whole plasma.

Chapter 6

Conclusion

In this thesis I have presented experimental measurements of laser-induced fluorescence from the ions in an ultracold neutral plasma. Fluorescence measurements were made when the probe laser frequency was scanned over the emission lineshape. From these fluorescence data we extracted the rms velocity distribution as a function of time by fitting the data to a Voigt profile. An expansion model was used to find the electron and ion temperatures. We have improved our data measurement and acquisition capabilities by implementing an optical frequency comb. The comb can operate in either a partially or fully stabilized configuration, with an accuracy of approximately 10 kHz, as determined by locking to transitions in ^{85}Rb and Cs using saturated absorption and scanning over the $4s^2\ ^1S_0 \rightarrow 4s4p\ ^1P_1^o$ transition in ^{40}Ca.

We studied the effect of electron shielding on ion equilibration at early times by varying the initial electron temperatures. Information about the ion and electron temperatures was used to calculate the strong coupling parameter Γ_{ii} and the electron shielding κ. We compared our experimental results with molecular dynamics simulations and theoretical calculations for the ion strong coupling in ultracold plasmas as a function of the electron shielding. We found that our experimental data showed good agreement with MD results. We generated plasmas with very cold ions because electron screening mitigates the effects of DIH. However we also found that elec-

tron shielding softens the ion interaction strength, which has the net effect of keeping the ratio of potential energy to kinetic energy constant for all values of κ.

Our results indicate that it may be possible to use electron screening to generate a strongly coupled plasma with $\Gamma_{ii} > 4$. This could be done by ionizing a low-density atom cloud with very low initial electron temperature. The low density will reduce the time scale for electron heating due to three-body recombination. The plasma electrons could be heated so that the ions are adiabatically shifted into their equilibrium positions in an unscreened plasma as κ is reduced to zero. A large initial size for the plasma would also reduce the time scale for the plasma to expand.

We have also built an experiment in laser-cooled calcium designed to test the prediction that higher values of the strong coupling parameter in ultracold neutral plasmas can be realized if the plasma ions are excited to higher ionization states. We mapped out the ion velocity distribution of the singly ionized Ca in order to measure the effect that the timing of second ionization pulses has on the temperature of the Ca^+ ions. By fitting the ion velocity distribution to an expansion model, we were able to determine the increase in heating due to the second ionization. Our measurements verified the prediction that heating due to the second ionization is minimized when the second ionization pulses are timed to arrive at the peak of the first oscillation in the kinetic energy.

Increasing the charge state of the plasma increases the nearest-neighbor potential energy. If the plasma could be 100% doubly ionized, the potential energy would quadruple. With the second ionization pulses timed to arrive at the peak of the first kinetic energy oscillation, where heating due to the second ionization is minimized, Γ would increase by a factor of 4. Since we are not doubly ionizing 100% of the plasma, it is not immediately clear what the increase in Γ is. Determining the change in Γ will require MD simulations that take into consideration the percentage of the plasma that is ionized. It will also be necessary to simulate different geometric configurations, i.e. producing a column of Ca^{2+} ions within the Ca^+ plasma versus a random distribution of Ca^{2+} ions within the Ca^+ plasma.

Improvements to the experiment will address some of the potential issues that exist in the present system. For example, increasing the power and improving the beam quality of the ionizing pulses will allow us to address the possibility that we are not homogeneously ionizing the plasma, which can result in density variations across the plasma and additional heating. With more power we can also increase the size of the pulses, which addresses the concern that our second ionization fraction is limited by geometry.

Ultimately, we are interested in making measurements of the effect that strong coupling in ultracold plasmas has on the plasma dynamics and processes such as the three-body recombination rate and the plasma expansion. This may require the ability to tune the wavelength of the last step in the second ionization process. Additionally, if 100% of the plasma is doubly ionized, we will need to employ other diagnostic techniques for making our measurements, which might include looking at the laser-induced fluorescence of the recombined ions, or using RF detection techniques [11,20].

In spite of the many challenges that an experiment of this complexity presents, it is also rich in potential for gaining insight into the dynamics of strongly coupled plasmas. Exciting the plasma to the second ionization state can push Γ into a regime that has not been achieved in an ultracold neutral system of photoionized laser-cooled atoms and provides fertile ground for future experiments in an strongly coupled neutral system.

Appendix A

Deriving the DIH ion temperature

The energy density per particle of the ultracold plasma can be generically written as

$$\mathscr{E} = \frac{3}{2} n k_B (T_e + T_i) + \frac{n^2}{2} \sum_{a,b} \int d^3 r \, u_{ab}(r) \, g_{ab}(r), \tag{A.1}$$

where the summation indexes represent electrons e or ions i. The Coulomb potential is written as $u_{ab} = (q_a q_b / 4\pi\varepsilon_0)(1/r)$ and the radial distribution function between species a and b is $g_{ab}(r)$. This expression assumes a uniform plasma density, n. While the potential energy terms in Eq. A.1 are general, the kinetic energy is written in terms of the temperatures T_e and T_i.

In order to quantify the ion heating during the DIH process, we will examine Eq. A.1 at two important instances in the plasma evolution. The first instance is just after the plasma is formed, after the electrons have thermalized with each other but before the ions have moved ($1/\omega_e \sim 1$ ns). Compared to the other energy scales in the system at this moment, the ions have essentially zero kinetic energy and we will therefore set the T_i to zero. We will call this instance the initial time.

The second instance is after the ions have thermalized with each other but before the plasma has expanded ($1/\omega_i \sim 100 - 500$ ns). The ions will have moved primarily due to the Coulomb force of their nearest neighbors. Collisional transfer of energy from the electrons to the ions is much slower than the ion-ion collision rate. Consequently the electrons and ions maintain separate

temperatures. The kinetic energy gained by the ions to this point will have come from the electrical potential energy of their screened neighboring ions. We will call this instance the final time.

Conserving energy, $\mathscr{E}_I = \mathscr{E}_F$, allows us to write,

$$\begin{aligned}\left[\frac{3}{2}nT_e + \frac{n^2}{2}\int d^3r\,(u_{ii}g_{ii} + u_{ee}g_{ee} + 2u_{ei}g_{ei})\right]_I \\ = \left[\frac{3}{2}n\,(T_e + T_i)\right]_F \\ + \left[\frac{n^2}{2}\int d^3r\,(u_{ii}g_{ii} + u_{ee}g_{ee} + 2u_{ei}g_{ei})\right]_F,\end{aligned} \tag{A.2}$$

where $\mathscr{E}_I$ and $\mathscr{E}_F$ are the initial and final energy densities and the explicit r-dependence of the potentials and distribution functions has been suppressed.

We can solve this equation if we assume that the electron temperature remains constant. In this case we can also ignore the term $u_{ee}g_{ee}$ on both sides of the equation because it remains unchanged from the initial to final time. We can also ignore the term $u_{ei}g_{ei}$ because the constant T_e approximation doesn't change the coupling between the electrons and ions when the ions move. The dominant change occurs in the ion-ion interaction.

With these approximations, Eq. A.2 becomes

$$\left[\frac{3}{2}nT_i\right]_F = \left[\frac{n^2}{2}\int d^3r\,u_{ii}\right]_I - \left[\frac{n^2}{2}\int d^3r\,u_{ii}g_{ii}\right]_F, \tag{A.3}$$

Note that the term g_{ii} in the initial state has been dropped because the initial state is completely disordered and $[g_{ii}]_I = 1$. We can make a connection with the Yukawa-MD simulations of Refs. [46–49] by introducing the Yukawa potential. The final state ion-ion potential can be trivially written as

$$u_{ii} = u_{ii}^Y + \left[u_{ii} - u_{ii}^Y\right]. \tag{A.4}$$

Similarly, we can express the radial distribution function as

$$g_{ii}(r) = [g_{ii}(r) - 1] + 1 = h_{ii}(r) + 1, \tag{A.5}$$

where $h_{ii}(r)$ is the pair correlation function. Inserting these definitions into Eq. A.3 and simplifying gives

$$\begin{aligned}\frac{3}{2}nT_i = &-\frac{n^2}{2}\int d^3r\, u_{ii}^Y(h_{ii}+1) \\ &-\frac{n^2}{2}\int d^3r\,\left(u_{ii}-u_{ii}^Y\right)h_{ii}+\frac{n^2}{2}\int d^3r\,u_{ii}^Y\end{aligned} \tag{A.6}$$

where all quantities are evaluated in the final state. The second term on the RHS is small and can be neglected. At small r, the quantity $u_{ii}-u_{ii}^Y$ is small and at large r the pair correlation function $h_{ii}(r)$ tends to zero. The last term on the RHS can be evaluated directly and is equal to $-(3/2)n\Gamma k_B T_i/\kappa^2$. The first term on the RHS has been tabulated using molecular dynamics (MD) simulations [46–49]. It is the potential energy of the Yukawa ions after the DIH process has completed. In order to compare directly with the MD simulations, we need to convert from energy density to energy per particle. This is done by multiplying by the volume and dividing by the number of ions. We find the final ion temperature to be

$$\frac{3}{2}k_B T_i = -\frac{n}{2}\int d^3r\, u_{ii}^Y(h_{ii}+1) - \frac{3\Gamma}{2\kappa^2}k_B T_i. \tag{A.7}$$

While this expression could be simplified further, we will leave it in this form in order to more easily compare with the results of previously published MD simulations.

The MD simulations by Hamaguchi tabulate the temperature-scaled "excess energy" per particle, $u \equiv \hat{U}/NkT$, which is written as [48]

$$\begin{aligned}u = \Gamma\Bigg[&\frac{1}{N}\sum_{j=1}^{N-1}\sum_{k=j+1}^{N}\hat{\Phi}(|\vec{\xi}_k-\vec{\xi}_j|)-\frac{3}{2\kappa^2}-\frac{\kappa}{2} \\ &+\frac{1}{2}\sum_{n\neq 0}\frac{\exp\left(-\kappa|n|\Lambda\right)}{|n|\Lambda}\Bigg]\end{aligned} \tag{A.8}$$

We recognize the first term on the RHS of Eq. A.8 as the integral in Eq. A.7 divided by $k_B T_i$. The last term on the RHS of Eq. A.8 explicitly accounts for the periodic boundary conditions, which we will neglect because we are considering an infinite-sized plasma. Equation A.8 includes the

energy of the Debye sheath, $-\kappa/2$. To get the "true" potential energy per particle, we add this back in and multiply by $k_B T_i$,

$$\left(\frac{u}{\Gamma}+\frac{\kappa}{2}\right) k_B T_i \Gamma = \frac{\Gamma k_B T_i}{N} \sum_{j=1}^{N-1} \sum_{k=j+1}^{N} \hat{\Phi}(|\vec{\xi}_k - \vec{\xi}_j|) - \frac{3\Gamma}{2\kappa^2} k_B T_i \tag{A.9}$$

Comparing this with Eq. A.7 gives

$$T_i = \frac{2}{3} \frac{q^2}{4\pi\varepsilon_0 a_{ws} k_B} \left(\frac{u}{\Gamma}+\frac{\kappa}{2}\right). \tag{A.10}$$

This derivation is complementary to the one presented in [6].

Appendix B

Simulating ion motion by solving the optical Bloch equations

B.1 Ion motion and the Yukawa potential

In neutral plasmas, electrons shield ion interactions. If the electron temperature is not too low, the ion-ion potential can be modeled as a Yukawa potential [6]

$$V(r) = \frac{e^2}{4\pi\varepsilon_0}\frac{e^{-r/\lambda_D}}{r}. \tag{B.1}$$

In the computer simulation we use, ions interact via the Yukawa potential. We assume an isothermal electron distribution, where $\Gamma_e < 1$. Plasma ions are randomly distributed over a cubic cell of approximate dimensions $L = w/10$. The cell dimensions are smaller than the rms size of the plasma but larger than the Debye screening length. The density is constant across the cell, and we use wrapped boundary conditions to maintain a constant number of ions in the cell. We find the x, y, and z components of the force on each ion due to the screened interactions of all the other ions by taking the gradient of Eq. 1.7. From the calculated force we find the acceleration of each ion. We move the ions in time using a fourth-order Runge-Kutta stepper.

Ions move within the cell and experience a Doppler shift of the probe laser beam frequency, given by

$$\Delta\omega = \frac{2\pi f}{c} v \tag{B.2}$$

where f is the atomic resonance frequency in the rest frame of the atom, c is the speed of light, and v is the component of the atomic velocity along the direction of the laser beam propagation. Another shift of the probe beam frequency comes from the radial acceleration of the plasma as the plasma expands. At early times, the plasma expansion can be approximated as

$$v_{\exp}(r,t) = r\frac{2k_B T_e}{m_i w} t \tag{B.3}$$

where r is the radial coordinate and t is the time. This model also assumes an isothermal electron distribution. The temperature of the electrons changes in time due to plasma expansion, evaporation, electron-ion recombination, and electron-Rydberg collisions, however these changes in the electron temperature can be neglected at early enough times. Similarly, at these early times the plasma ions accelerate, but the density profile of the plasma does not change. Thus we can say that this model is valid for early times, when the electron temperature is not too low.

Using the components of the force derived from the Yukawa potential, we calculate the position and velocity of each ion for every time step. Information about the ion velocity, which includes the contribution of the overall plasma expansion, is used to find the ion's frequency shift $\omega = \omega_o - \omega_{laser}$. This detuning is necessary for solving the optical Bloch equations to find the evolution of the Bloch vector and the excited-state fraction, which gives the simulated fluorescence signal.

B.2 Optical Bloch equations

Since the fluorescence signal is proportional to the excited-state fraction, care must be taken to simulate the evolution of the internal state of the ions. This is accomplished by solving the optical

Bloch equations at each time step for each ion in the cell. The ions are approximated as two-level atoms dressed by a light field. The Hamiltonian of this system is

$$H = H_{atom} + H_{laser} \tag{B.4}$$

where H_{atom} is the Hamiltonian of the atom and H_{laser} is the Hamiltonian of the light field. Using the rotating wave approximation (RWA) we can write the total Hamiltonian as

$$H = \hbar\omega\sigma_-\sigma_+ + \frac{\hbar\Omega}{2}(\sigma_- + \sigma_+), \tag{B.5}$$

where ω is the detuning, Ω is the Rabi frequency, and the raising and lowering matrices are

$$\sigma_+ = \begin{pmatrix} 0 & 1 \\ 0 & 0 \end{pmatrix} \quad \sigma_- = \begin{pmatrix} 0 & 0 \\ 1 & 0 \end{pmatrix}. \tag{B.6}$$

Written in terms of matrices, the Hamiltonian is

$$H = \begin{pmatrix} 0 & 0 \\ 0 & -\hbar\omega \end{pmatrix} + \begin{pmatrix} 0 & \frac{\hbar\omega}{2} \\ \frac{\hbar\omega}{2} & 0 \end{pmatrix}. \tag{B.7}$$

The equation for the density matrix is given by the Liouville-Bloch equation with decay, found in Eq. (1) of Ref. [55]

$$\dot{\rho} = -\frac{i}{\hbar}[H(t), \rho] - \Gamma(t)\rho. \tag{B.8}$$

The density matrix ρ and its time derivative $\dot{\rho}$ are

$$\begin{aligned} \rho &= \begin{pmatrix} \rho_{ee} & \rho_{eg} \\ \rho_{ge} & \rho_{gg} \end{pmatrix} \\ \dot{\rho} &= \begin{pmatrix} \dot{\rho}_{ee} & \dot{\rho}_{eg} \\ \dot{\rho}_{ge} & \dot{\rho}_{gg} \end{pmatrix}. \end{aligned} \tag{B.9}$$

The term $\Gamma(t)\rho$ is the decay term, given by Eq. (3) of Ref. [55],

$$\Gamma\rho = \frac{\Gamma}{2}(\sigma_+\sigma_-\rho \; + \; \rho\sigma_+\sigma_-) - \Gamma\sigma_-\rho\sigma_+ \tag{B.10}$$

Written in terms of our Hamiltonian and the raising and lowering operators, the equation we get for the density matrix is

$$\begin{aligned}\dot{\rho} &= -i\omega(\sigma_+\sigma_-\rho - \rho\sigma_+\sigma_-) - i\frac{\Omega}{2}[(\sigma_+ + \sigma_-)\rho - \rho(\sigma_+ + \sigma_-)] \\ &+ \frac{\Gamma}{2}(2\sigma_-\rho\sigma_+ - \sigma_+\sigma_-\rho - \rho\sigma_+\sigma_-).\end{aligned} \tag{B.11}$$

If we insert Eq. B.6 and Eq. B.9 into this equation for the density matrix we get

$$\begin{pmatrix}\dot{\rho}_{ee} & \dot{\rho}_{eg} \\ \dot{\rho}_{ge} & \dot{\rho}_{gg}\end{pmatrix} = -i\omega\begin{pmatrix}0 & \rho_{eg} \\ -\rho_{ge} & 0\end{pmatrix} - \frac{i\Omega}{2}\begin{pmatrix}\rho_{ge}-\rho_{eg} & \rho_{gg}-\rho_{ee} \\ \rho_{ee}-\rho_{gg} & \rho_{eg}-\rho_{ge}\end{pmatrix} - \frac{\Gamma}{2}\begin{pmatrix}2\rho_{ee} & \rho_{eg} \\ \rho_{ge} & -2\rho_{ee}\end{pmatrix} \tag{B.12}$$

In a 2-level system, the components of the Bloch vector are expressed by the Pauli matrices:

$$\sigma_x = \begin{pmatrix}0 & 1 \\ 1 & 0\end{pmatrix} \quad \sigma_y = \begin{pmatrix}0 & -i \\ i & 0\end{pmatrix} \quad \sigma_z = \begin{pmatrix}1 & 0 \\ 0 & -1\end{pmatrix}. \tag{B.13}$$

If we remember that the expectation value of an operator is the trace of the operator times the density matrix, we can show that

$$\begin{aligned}\langle\sigma_x\rangle &= \mathrm{Tr}(\sigma_x\rho) = (\rho_{ge} + \rho_{eg}) \\ \langle\sigma_y\rangle &= \mathrm{Tr}(\sigma_y\rho) = i(\rho_{eg} - \rho_{ge}) \\ \langle\sigma_z\rangle &= \mathrm{Tr}(\sigma_z\rho) = (\rho_{ee} - \rho_{gg}).\end{aligned} \tag{B.14}$$

We are concerned with how the internal state of the atom changes with time. We therefore want to find the time derivative of the expectation values of σ_x, σ_y, and σ_z, which are components of the Bloch vector. Finding how they change in time tells us how the Bloch vector changes in time.

Taking the derivative of Eq. B.14 we get

$$\begin{aligned}
\frac{d\langle\sigma_x\rangle}{dt} &= (\dot{\rho}_{ge}+\dot{\rho}_{eg}) \\
\frac{d\langle\sigma_y\rangle}{dt} &= i(\dot{\rho}_{eg}-\dot{\rho}_{ge}) \\
\frac{d\langle\sigma_z\rangle}{dt} &= (\dot{\rho}_{ee}-\dot{\rho}_{gg})
\end{aligned} \tag{B.15}$$

From Eq. B.12 we have

$$\begin{aligned}
\dot{\rho}_{ee} &= -\frac{i\Omega}{2}(\rho_{ge}-\rho_{eg})-\Gamma\rho_{ee} \\
\dot{\rho}_{eg} &= -i\omega\rho_{eg}-\frac{i\Omega}{2}(\rho_{gg}-\rho_{ee})-\frac{\Gamma}{2}\rho_{eg} \\
\dot{\rho}_{ge} &= i\omega\rho_{ge}-\frac{i\Omega}{2}(\rho_{ee}-\rho_{gg})-\frac{\Gamma}{2}\rho_{ge} \\
\dot{\rho}_{gg} &= -\frac{i\Omega}{2}(\rho_{eg}-\rho_{ge})+\Gamma\rho_{ee}.
\end{aligned} \tag{B.16}$$

Putting it all together, the equations of motion, written in terms of Pauli matrices, are

$$\begin{aligned}
\frac{d\langle\sigma_z\rangle}{dt} &= \Omega\langle\sigma_y\rangle-\gamma(1+\langle\sigma_z\rangle) \\
\frac{d\langle\sigma_y\rangle}{dt} &= \omega\langle\sigma_x\rangle-\Omega\langle\sigma_z\rangle-\frac{\gamma}{2}\langle\sigma_y\rangle, \\
\frac{d\langle\sigma_x\rangle}{dt} &= -\omega\langle\sigma_y\rangle-\frac{\gamma}{2}\langle\sigma_x\rangle.
\end{aligned} \tag{B.17}$$

The fluorescence signal $f(t)$ depends on time as

$$f(t)=\frac{1}{2}[1+\langle\sigma_z(t)\rangle]. \tag{B.18}$$

We simulate decay from the excited state to the metastable dark $3d$ state by multiplying the total fluorescence rate by the branching ratio. This gives us the decay rate into the optically dark $3d\ ^2D_{3/2}$ state. We multiply this decay rate by the time step dt to find the probability that the ion has made a transition to this state. This probability is compared to a random number between 0 and 1. If the probability of decay is greater than this random number, the simulated ion transitions to the dark state and no longer fluoresces.

Appendix C

Density and temperature scaling of disorder-induced heating in ultracold plasmas

This appendix contains a reprint of Ref. [9] and is included in its entirety as a supplement to Sec. 4.2.

PHYSICAL REVIEW A **83**, 023409 (2011)

Density and temperature scaling of disorder-induced heating in ultracold plasmas

S. D. Bergeson,[1] A. Denning,[1] M. Lyon,[1] and F. Robicheaux[2]
[1]*Department of Physics and Astronomy, Brigham Young University, Provo, Utah 84602, USA*
[2]*Department of Physics, Auburn University, Auburn, Alabama 36849, USA*
(Received 22 September 2010; revised manuscript received 2 December 2010; published 11 February 2011)

We report measurements and simulations of disorder-induced heating in ultracold neutral plasmas. Fluorescence from plasma ions is excited using a detuned probe laser beam while the plasma relaxes from its initially disordered nonequilibrium state. This method probes the wings of the ion velocity distribution. The simulations yield information on time-evolving plasma parameters that are difficult to measure directly and make it possible to connect the fluorescence signal to the rms velocity distribution. The disorder-induced heating signal can be used to estimate the electron and ion temperatures ∼100 ns after the plasma is created. This is particularly interesting for plasmas in which the electron and ion temperatures are not known.

DOI: 10.1103/PhysRevA.83.023409 PACS number(s): 32.50.+d, 52.20.−j, 52.65.Rr, 37.10.De

I. INTRODUCTION

Strongly coupled neutral plasmas combine elements of atomic physics, plasma physics, and condensed-matter physics [1–6]. Many of the simplifying approximations used in these different fields can be tested in strongly coupled systems. For example, the number of particles per Debye sphere can be continuously adjusted over a wide range by changing the initial electron energy and plasma density. This makes it possible to study the transition from an ideal plasma to a strongly coupled Coulomb system in a regular and highly controlled manner.

Ultracold neutral plasmas are created by photoionizing laser-cooled atoms [7–12]. Although the initial ion temperature is typically 1 mK, it rapidly increases by a few orders of magnitude due to Coulomb interactions with neighboring ions [5,10–13]. The strong coupling parameter is thereby limited to $\Gamma \approx 2$, where $\Gamma = e^2/4\pi\epsilon_0 a_{ws} k_B T$ is the ratio of nearest-neighbor potential energy to kinetic energy, $a_{ws} = (3/4\pi n)^{1/3}$ is the Wigner-Seitz radius, and n is the density. This heating mechanism, raising the ion temperature from essentially zero to near the correlation temperature

$$T_c = \frac{2}{3}\,\frac{e^2}{4\pi\epsilon_0 a_{ws} k_B}, \tag{1}$$

is called "disorder-induced heating" (DIH). This is a nonequilibrium, ultrafast relaxation, similar to what occurs in high-density laser-produced plasmas and laser-driven fusion plasmas, as well as many other systems [14]. Interestingly, for the case of ultracold neutral plasmas, if the initial spatial distribution of ions was highly ordered and periodic this heating would not occur [5,15]. This suggests that DIH measurements could be used to measure disorder in systems such as BEC Mott insulators [16] and Rydberg crystals [17].

Plasma ions reach T_c approximately when $t\omega_p \sim 1$ [10,18–20], where $\omega_p = \sqrt{ne^2/m_i\epsilon_0}$ is the ion plasma frequency and m_i is the ion mass. This is a quasiuniversal behavior of dense plasma systems including Z-pinch and high-intensity laser ablation experiments when the the initial electrical potential energy is greater than the kinetic energy. The initial ion motion is dominated by nearest-neighbor interactions [18] when the ions push on each other. Even though single-particle motion in a plasma is tightly coupled to collective modes, collective motion does not begin until approximately one ion plasma period (ω_p^{-1}) after DIH begins. Studies of DIH therefore necessarily explore the cross-over time that spans the transition from nearest-neighbor interactions to collective behavior.

Electrons screen interactions between ions in neutral plasmas. The typical screening distance is the Debye screening length, $\lambda_D = \sqrt{k_B T\epsilon_0/ne^2}$. When the Debye length λ_D is comparable to the distance between ions a_{ws}, screening reduces the ion-ion potential energy, slows the ion motion during the DIH phase, and reduces the final ion temperature.

The influence of electron screening on the ion temperature has been studied [10,18–20]. For systems in thermodynamic equilibrium, simulations of Yukawa fluids have found interaction energies and self-consistent temperatures displaying this effect [15,21–23]. Experimentally, studies have been published showing that the ion temperature scales with density as shown in Eq. (1) and that the DIH rise time scales as ω_p^{-1}. Figure 3 of [20] may suggest a change in the DIH time scale with density and temperature. However, no definitive studies or measurements of changes in the DIH process with electron screening appear to have been published.

In this paper we present a study of the density and temperature dependence of DIH in ultracold neutral plasmas. We measure this time using experimental measurements and computer simulations. Fluorescence is excited by passing a narrowband cw probe laser beam through the plasma. It is detuned a few linewidths from the ion resonance transition. The fluorescence signal is sensitive to the wings of the velocity distribution. We observe oscillations in the width of the ion velocity distribution and from this determine the time scale for the DIH process to occur. From the simulations we determine relationships between the electron screening parameter and the ion temperature and the rms velocity width. At high density and low temperature the observed DIH time scale departs from the expected $n^{-1/2}$ density scaling, and the role of electron screening in lengthening the DIH time scale is measured. We show how measuring the DIH time scale at known plasma density makes it possible to determine both the electron and ion temperatures 50 to 200 ns after the plasma is created.

II. METHODS

By combining experimental measurements with simulations we are able to relate observed signals to the details of

the ion velocity distribution. The details of the experiment and simulation are described in this section.

A. Experiment

In the experiment, 2×10^7 ^{40}Ca atoms are laser-cooled and trapped in a magneto-optical trap (MOT) [12]. The trap density is approximately $n(r) = n_0 \exp(-r^2/2\sigma^2)$, where $n_0 \leqslant 10(5) \times 10^{10}$ cm^{-3} and σ is 0.3 mm. Atoms in the trap are photoionized using pulsed lasers at 423 nm (the $4s^2\,{}^1S_0 \rightarrow 4s4p\,{}^1P_1$ transition) and 390 nm ($4s4p\,{}^1P_1 \rightarrow$ continuum) with pulse durations of 3 ns. The initial electron energy is typically determined by the wavelength of the 390-nm laser and is equal to the difference between the combined laser photon energy of the ionizing lasers and the atomic ionization potential. However, when the photon energy of the 390-nm pulsed laser ionizes the calcium atoms right at threshold the initial electron energy is determined by the bandwidth of the laser to approximately 1 cm$^{-1} \sim 0.5$ K.

After the plasma is generated, plasma ions are excited using a standing-wave cw probe laser beam detuned about four linewidths (a total of 90 MHz) below the $4s\,{}^2S_{1/2} \rightarrow 4p\,{}^2P_{1/2}$ transition at 397 nm. The probe laser beam is collimated to a Gaussian waist of 0.62 mm, making the rms size of the probe laser beam somewhat larger than the initial rms size of the ultracold plasma. The maximum probe laser beam intensity is approximately $s_0 = I/I_{\rm sat} = 2$ times the saturation intensity, where $I_{\rm sat} = 46$ mW/cm^2. Fluorescence at 397 nm is collected using a lens, isolated using a optical band-pass interference filter, detected using a 1-GHz bandwidth photomultiplier tube, and recorded using a 1-GHz bandwidth digital oscilloscope.

Sample fluorescence data are shown in Fig. 1. Ion fluorescence is plotted as a thin black line. The plasma is generated at time $t = 0$. The ground-state ions begin to scatter photons from the probe laser beam. A strongly damped Rabi oscillation in the ion population is visible near 7 ns. The time at which this signal maximizes depends on the probe laser beam detuning and intensity. This peak is followed by a broader shoulder in the fluorescence signal at 70 ns. The time at which this shoulder appears depends primarily on the plasma density and also on the electron temperature. This signal arises from broadening of the ion velocity distribution due to DIH, increasing the number of ions Doppler-shifted into resonance with the probe laser beam. At later times, the ion velocity distribution is further broadened by the outward radial acceleration and expansion of the plasma. This broadening gives rise to the very broad peak in the fluorescence signal at times near 1 μs, again depending on density and temperature.

The data analysis method is also shown in Fig. 1. The visibility of the DIH shoulder is increased by fitting the fluorescence signal in the 100-to-300-ns range to a straight line. This is shown as the dashed line in Fig. 1. The DIH peak in the background-subtracted signal, shown as the inset in Fig. 1, is fit using a parabola. The maximum of this parabolic fit is called t_0. It is an indicator of the time at which the width of the DIH-broadened velocity distribution reaches a maximum. As is shown in Sec. III, this time t_0 is offset a few percent from the time at which the velocity distribution reaches a local maximum.

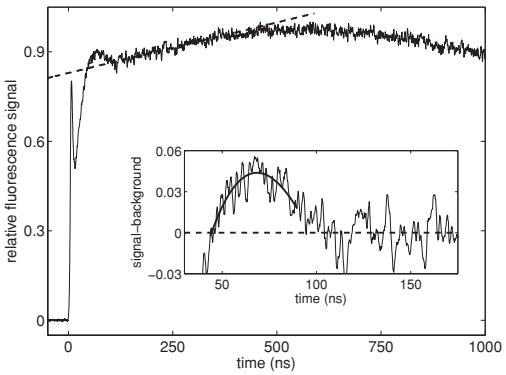

FIG. 1. Typical fluorescence signal and analysis, $T_e = 20$ K, $n_0 = 5 \times 10^{16}$ m^3, $\Delta f = -90$ MHz, and $s_0 = 1.7$. The fluorescence signal is plotted as a thin black line. The strongly damped Rabi oscillation gives a peak near 7 ns. The shoulder on the data near 70 ns is due to DIH broadening of the velocity distribution. The much broader signal peak near 600 ns is due to the accelerated expansion of the plasma. The heavy dashed line is a linear fit to the fluorescence signal between 100 and 300 ns. The inset shows the signal with this linear fit subtracted. The DIH signal now appears as a peak above a flat background. The heavy solid line shows a parabolic fit to the background subtracted data near the DIH peak. The time at which this fitted curve reaches its maximum is the characteristic DIH time, t_0.

B. Yukawa simulation

To better understand the experimental data and to test our data analysis, we simulate the fluorescence signal from the plasma. The simulation is described in Ref. [24]. It is performed by integrating the optical Bloch equations for a collection of ions in a cell. The ions interact via the Yukawa potential. The potential on ion j can be written as $\phi_Y = \sum_i e \exp(-r_{ij}/\lambda)/(4\pi\epsilon_0 r_{ij})$, where r_{ij} is the distance between plasma ions i and j, and the sum runs over all the ions in the cell with $i \neq j$. This treatment inherently assumes an isothermal electron distribution which is valid at early times as long as $\Gamma_e < 1$ [25].

Plasma ions are randomly distributed over a cubic cell with wrapped boundary conditions. The cell dimension is much smaller than the rms size of the plasma but larger than the Debye screening length. The ions move under the influence of the screened Coulomb force of the other ions in the cell. The force on ion j is $\vec{F}_j = -e\nabla_{ij}\phi_Y$, where the divergence is calculated with respect to the distance r_{ij}. This part of the simulation is similar to that of Ref. [18].

At each time step, we solve the optical Bloch equations for each ion in the cell. The fluorescence signal is proportional to the excited-state fraction. This fraction depends on the detuning of the laser beam from the 397-nm resonance transition for each ion. The detuning depends on the initial offset of the probe laser beam from the 397-nm resonance transition, on the ion motion due to DIH through the Doppler shift, and also on the overall accelerated plasma expansion. It has been shown that the plasma expansion at late times is

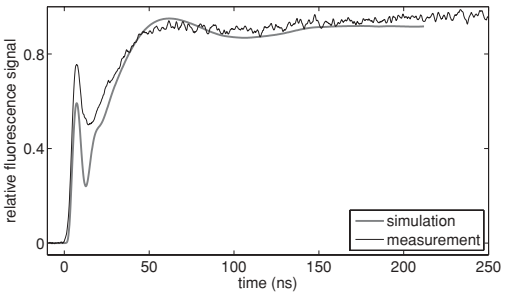

FIG. 2. A comparison of the simulated fluorescence signal (thick gray line) and the experimentally measured one (thin black line). Both signals show the heavily damped Rabi oscillation, the DIH shoulder, and the broad background due to the plasma expansion. For this plot the peak density is $n_0 = 5(3) \times 10^{10}$ cm^{-3}.

nontrivial when the initial electron temperature approaches T_C (or when the electron $\Gamma \approx 1$) [25].

However, as the details of the plasma expansion play a minor role during the first few hundred ns and we are careful to ensure the electron $\Gamma \ll 1$ in our simulation, the details of the expansion are relatively unimportant to our analysis. During the earliest part of the calculation we use $v(r,t) = r(2k_B T_e/m\sigma^2)t$ to calculate the velocity of the cell, where r is the radial coordinate of the cell. For times longer than ~50 ns we find the radial acceleration by solving the Gaussian expansion equations [26]. In this case, the size of the plasma σ increases with time.

A comparison of the simulated fluorescence data and the experimentally measured fluorescence data is shown in Fig. 2. Both signals show the heavily damped Rabi oscillation, the DIH shoulder, and the broad background due to the plasma expansion. The apparent height of the Rabi oscillation relative to the other fluorescence depends on the laser intensity and inhomogeneities in the experimental setup. However, the times at which these features appear agree well in the simulated and measured data over a wide range of density and temperature.

Using the simulation we can extract information about the plasma that is not easy to measure directly. This includes the details of the ion velocity distribution, the ion temperature as a function of time, and the influence of screening on ion equilibration.

III. DENSITY AND TEMPERATURE SCALING OF DIH IN A GAUSSIAN PLASMA

The temperature and density dependence of the DIH time t_0 is plotted in Fig. 3. Previous work has shown that the DIH time is proportional to the inverse of the nominal plasma frequency. Therefore, one would expect to find the relationship $t_0 \propto n^{-1/2}$. We see this density dependence at high temperatures and low densities, where the electron temperature is much greater than the correlation temperature T_C [see Eq. (1)] and the screening length λ_D is much greater than the mean distance between particles, a_{ws}. However, as the density increases and as the electron temperature approaches T_C, the time t_0 departs from the expected $n^{-1/2}$ density scaling. This departure is more

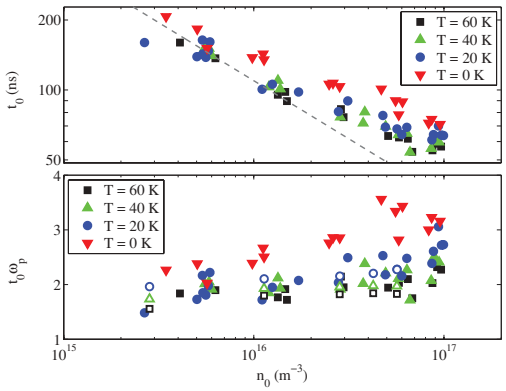

FIG. 3. (Color online) Experimental data. (Top) The time at which the DIH fluorescence peak occurs. The gray dashed line shows the expected time in the absence of screening effects. (Bottom) Scaled DIH peak time (data from the top panel) with t_0 corrected using Eq. (2). Open symbols are from the simulation. This data would all fall on a flat line if there was no screening.

apparent in the bottom panel of Fig. 3, where the quantity $t_0\omega_p$ is plotted as a function of density. If there was no screening effect, all of the data would fall on the same horizontal line near $t_0\omega_p \sim 1.5$.

It would be most valuable to connect the time t_0 to velocity distribution so that this time can be directly related to the true heating mechanism in the plasma. In the expanding Gaussian plasma simulation, we compare t_0 to the time at which the rms velocity distribution reaches its first maximum. We observe a small time difference. This difference, Δt, depends most strongly on density as

$$\Delta t = 22\,\text{ns} - (a_{ws})(7.7\ \text{ns}/\mu\text{m}). \quad (2)$$

For the densities in this study, this corresponds to a $\leqslant 15\%$ correction in the measured DIH peak time. This is much smaller than the factor of ~2 increase we see in the scaled time $t_0\omega_p$. We also see a dependence of Δt on the initial electron temperature. For the $T = 20$, 40, and 60 K data in this study, the temperature correction is an additional few percent. The correction in Eq. (2) is related to the difference between the width of the rms velocity distribution and the number of ions Doppler shifted into resonance with the probe laser beam. If the velocity distribution was exactly Gaussian, there would be no correction. However, the additional ions in the high-velocity tail of the distribution increases the fluorescence signal faster than the rms velocity distribution broadens. This difference is discussed briefly in Sec. IV A and Fig. 4.

The data in the top panel of Fig. 3, shows our measured t_0 as a function of density for a range of temperatures. In the bottom panel of Fig. 3 we plot the DIH peak time with the correction described in Eq. (2) applied and then multiplied by the nominal ion plasma frequency. The data clearly departs from a horizontal line as the temperature decreases and as the density increases. This observation shows the onset of many-body interactions in the ultracold plasma as the description of

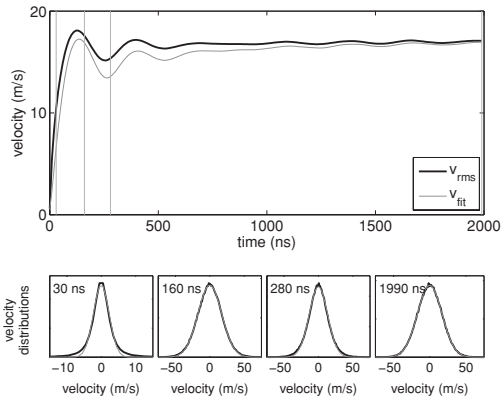

FIG. 4. Velocity distributions and their evolution with time. The top panel shows the rms velocity for $n = 4.0 \times 10^9$ cm^{-3} and an electron temperature of 60 K, plotted in the solid black line. Also plotted is the rms width of a Gaussian fit to the velocity distribution. High-energy ions in the wings of the distribution tend to make the rms width greater than the Gaussian width. The four vertical thin gray lines mark times at which the velocity distribution is plotted in the bottom four panels. The width changes in time, and the wings of the distribution show variations compared to the Gaussian fit. In these bottom four plots the black line is the distribution from the simulation and the gray lines are the best Gaussian fit to the distributions.

the ion motion changes from nearest-neighbor to many-body physics.

The data in Fig. 3 show t_0 measurements in plasmas with the initial $T_e = 0$ K. The DIH time lengthens out more in this case compared to the higher-temperature plasmas. This lowest possible initial temperature corresponds to ionizing the MOT atoms right at threshold. The electrons themselves experience DIH during the first few electron plasma periods, equilibrating to the correlation temperature. They slowly heat up during the next few hundred ns due to three-body recombination and electron-Rydberg scattering [26–28]. This is an interesting case because the density alone determines the electron and ion temperatures and even the plasma time scales.

Because the electron temperature is determined by the density through T_C the *electron* Γ_e should be about 1 for all densities [13,27]. A constant and density-independent value of the electron Γ_e also means that the inverse scaled screening length $\kappa = a_{ws}/\lambda_D \sim n^{1/6}/T^{1/2} \sim \sqrt{\Gamma_e}$ should be constant. In light of Eq. (7) (see Sec. IV D) one would therefore expect the scaled ion DIH time $t_0\omega_p$ to be constant. However, it is apparent that $t_0\omega_p$ is density-dependent. Future research is needed to determine if the observed changes in t_0 are intrinsic to the relaxation of the plasma ion velocity distribution or if they are related to effects described in Eq. (2).

IV. SIMULATIONS IN A UNIFORM-DENSITY PLASMA

To gain some insight into the relaxation of the plasma without the potentially confounding influence of the Gaussian spatial distribution and the accelerated plasma expansion, we present some data in this section from our simulation of a uniform plasma. The ions are still generated with random initial positions and interact via the Yukawa potential. Only the spatial distribution and plasma expansion are changed in this simulation.

A. Ion velocity distribution

First we present the evolution of the ion velocity distribution. During the DIH phase, the ion velocity distribution is non-Gaussian [18]. The initial ion motion is due to the electrostatic interaction of the (screened) ions. The nearest-neighbor distribution in the plasma gives rise to a nonthermal initial velocity distribution. This distribution relaxes over time and approaches a Boltzmann distribution.

A plot of the ion velocity distribution is shown in Fig. 4. The initial velocity distribution is Gaussian, corresponding to a thermal distribution at the 1 mK neutral atom temperature before the atoms are ionized. This distribution is quickly broadened due to DIH. Ions that are nearer to their neighbors experience greater initial accelerations and reach relatively high velocities. Compared to a thermal distribution, these ions overpopulate the wings of the distribution and contribute to a relatively high rms velocity. As shown in the top panel of Fig. 4, these high-velocity wings damp out on the time scale of 1000 ns as the ion velocity distribution thermalizes.

The bottom four panels of Fig. 4 show distributions at 30, 160, 280, and 1990 ns after the plasma is formed. The width of the distribution oscillates at early times. It is apparent from these plots that the rms velocity is skewed by the relatively few high-velocity ions. The oscillations in the distribution decay on the time scale of an oscillation period. However, some oscillations persist at long times. These oscillations can be used to extract the plasma frequency as discussed in the following paragraphs.

B. Plasma frequency and dispersion

In our uniform-density-plasma simulations, oscillations in the velocity distribution are visible at times beyond 1000 ns (as shown in the top panel of Fig. 4). These oscillations are a remnant of the initial hardening of the ion-ion potential that occurred when the plasma was created. It is as though the photoionization step gave a δ-function impulse to the system. The velocity oscillations at late times are a manifestation of the normal modes of the system.

One might expect the oscillation frequency to be equal to the nominal ion plasma frequency, $\omega_p = \sqrt{ne^2/m_i\epsilon_0}$. However, the ion-ion interaction is moderated by the electron screening. A simple one-dimensional model suggests how this screening might change the ion oscillation frequency. One can imagine two ions fixed in space at locations of $\pm a_{ws}$ on the x axis. A test charge of the same sign is also placed on the x axis, displaced a small distance x from the origin. In this model, the particles interact via the Yukawa potential with screening length λ_D, and the particles are constrained to move only along the x axis. The potential energy is quadratic for small displacements and has the form

$$U(x) = \frac{e^2}{4\pi\epsilon_0 a_{ws}^3}\left(1 + \kappa + \frac{\kappa^2}{2}\right)\exp(-\kappa)\, x^2, \qquad (3)$$

where $\kappa \equiv a_{ws}/\lambda_D$ is the inverse scaled screening length. The oscillation frequency of this harmonic oscillator is

$$\omega_{\text{model}} = \omega_p f(\kappa), \tag{4}$$

where $f(\kappa) = \sqrt{2/3}(1 + \kappa + \kappa^2/2)\exp(-\kappa)$, ω_p is the ion plasma frequency, and the relationships between a_{ws}, n, and ω_p have been invoked. It is not expected that this oversimplified one-dimensional model will quantitatively predict the ion oscillation frequency. However, it hints at some of the important physics in the system and suggests that the frequency will get smaller as κ gets larger (corresponding to λ_D getting smaller).

We pursue the ion oscillation frequency just a little further here because it will help illustrate an important point about the DIH time t_0. We show that the ion oscillation frequency measured in our simulations agrees with previously published work under appropriate conditions. We also show that the characteristic DIH time t_0 in our simulations depends on κ but is *not* simply proportional to ω_p^{-1}.

The residual oscillations in the ion velocity distribution can be calculated using the dispersion relation. The dispersion relation gives the ion oscillation frequency as a function of screening length and mode wavelength. Dispersion relations for strongly coupled plasmas are reported in Ref. [29] for a wide range of ion and electron temperatures and plasma densities. Equation (7) in that paper,

$$\omega(q,\kappa) = \omega_p \left(\frac{q^2}{q^2+\kappa^2} + \frac{q^2}{\Gamma} - \frac{\eta^{*2} q^4}{4} \right)^{1/2}, \tag{5}$$

gives the real part of the ion plasma frequency and is appropriate for our plasmas. In this equation, $q \equiv k a_{ws} = 2\pi a_{ws}/\lambda$ is the scaled wave vector of the ion acoustic wave. Measurements probing the long-wavelength limit of the dispersion relation have recently been reported [30].

In our experiment, when an ultracold plasma is generated by ionizing the entire plasma, a wave packet is launched through the plasma. The average mode frequency can be obtained by averaging over an appropriate range of q values in Eq. (5). In essence, q becomes a fit parameter for our data, and Eq. (5) tells us how the average ion oscillation frequency changes with the screening length, κ.

These results are compared to Eq. (5) in Fig. 5. We use the ion temperature from in the simulation at times later than 1000 ns to calculate the ion Γ. We use the initial electron temperature and density to calculate κ. The best match of the data to the dispersion curve occurs with $q = 0.55$. We find a similarly good match by averaging Eq. (5) when q ranges from 0 to about 1.

C. t_0 and the ion oscillation frequency

With the average ion oscillation frequency in hand, we can show that the DIH time t_0 is not related either to this frequency or to the ion plasma frequency ω_p. The first DIH maximum in the ion velocity distribution width occurs when the initially stationary ions accelerate away from each other and before they collide with other neighboring ions. If this was a plasma oscillation, one could calculate the oscillation frequency ω by assuming that $t_0\omega = \pi/2$. In Fig. 5 the frequency obtained in this manner is plotted as a function of κ, represented as open symbols.

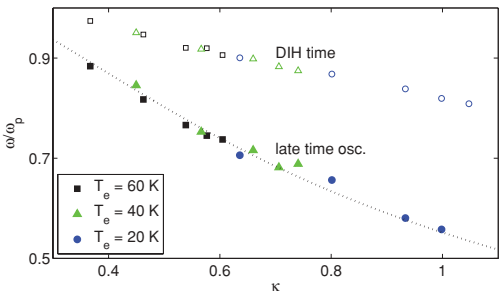

FIG. 5. (Color online) The ion oscillation frequency as a function of the inverse scaled screening length κ in a uniform (simulated) plasma. The solid symbols show the frequency determined from late-time ion velocity oscillations. The dashed line is Eq. (5) with $q = 0.55$. The open symbols show the ion oscillation frequency calculated by assuming that the DIH peak occurs $\frac{1}{4}$ through the oscillation period.

This frequency is clearly not the ion plasma frequency $\sqrt{ne^2/m_i\epsilon_0}$ because our observed "frequency" depends on κ. It is also clearly not the average mode frequency. There are no physically relevant values of either Γ or q that reproduce the observed dependence on κ.

This is perhaps not surprising. The relaxation of the plasma begins when there is no true thermodynamic equilibrium. As the system thermalizes, the plasma mode description becomes more appropriate. Interestingly, the changes in DIH time predicted by nearest-neighbor models is much weaker than what we observe in Fig. 5. It is clear, therefore, that the DIH time spans the crossover from a regime in which nearest-neighbor interactions dominate ion motion to one in which many-body physics is appropriate.

D. Ion temperature and DIH time in a uniform-density plasma

In the simulations, the equilibrium ion temperature depends on κ. In the simulation we can extract the rms ion velocity at times beyond 1000 ns after the initial transient oscillations have damped out. From this we can determine the ion temperature. We observe that the equilibrium ion temperature depends on the electron screening parameter as

$$\Gamma = 2.490 + 0.929\kappa + 0.785\kappa^2. \tag{6}$$

The DIH time t_0 also depends on on κ. The relationship is

$$t_0\omega_p = 1.445 + 0.467\kappa. \tag{7}$$

These equations are valid for $0.3 < \kappa < 1$.

In a plasma with known density, the DIH time can be measured and Eqs. (6) and (7) can be used to first determine κ and then to determine Γ. Both the electron and the ion temperature can be determined by measuring only t_0. Because the ion velocity distribution does not change significantly after t_0, this determination gives the temperatures at early times in the plasma, as short as 50 ns after the plasma is generated. Future work could test whether this continues to be true when the electrons become strongly coupled or when three-body

recombination and electron-scattering become important in very-low-temperature (or high-density) plasmas.

V. CONCLUSION

In conclusion, we have presented measurements and simulations of laser-induced fluorescence from ultracold neutral plasmas. We measure the time scale over which DIH occurs for a range of densities and temperatures. The DIH time departs from the expected $n^{-1/2}$ density scaling at high densities. It also depends on temperature. We use a simulation to determine the relationship between the observed DIH time and the first maximum in the rms velocity distribution. The DIH time depends on the electron screening length and it spans the transition from a nearest-neighbor to a many-body description of the system. Understanding this dynamic nonequilibrium transition may provide insights into other transient phenomena in laser physics and other applications.

Our simulation shows that the DIH time can be used to calculate the electron and ion temperatures in ultracold neutral plasmas approximately 100 ns after the plasma is created. This reduces the earliest time measurements of electron temperature for these systems. Further research could test these relationships [Eqs. (6) and (7)] when $\kappa > 1$ where recombination and scattering effects may be important at these early times. Additional research is also required to study the relationship between the fluorescence signal, which probes the wings of the velocity distribution, and the first maximum in the width of the velocity distribution. These future studies will require full molecular dynamics simulations because the Yukawa approximation is expected to be invalid in this regime.

ACKNOWLEDGMENTS

This work is supported in part by the National Science Foundation (Grant No. PHY-0969856) and the Chemical Sciences, Geosciences, and Biosciences Division of the Office of Basic Energy Sciences, US Department of Energy.

[1] T. C. Killian and S. D. Bergeson, Phys. World, February 2003, p. 37.
[2] T. C. Killian, Science **316**, 705 (2007).
[3] S. L. Rolston, Physics **1**, 2 (2008).
[4] T. C. Killian and S. L. Rolston, Phys. Today **63**, 46 (2010).
[5] T. Killian, T. Pattard, T. Pohl, and J. Rost, Phys. Rep. **449**, 77 (2007).
[6] M. Bonitz, C. Henning, and D. Block, Rep. Prog. Phys. **73**, 066501 (2010).
[7] T. C. Killian, S. Kulin, S. D. Bergeson, L. A. Orozco, C. Orzel, and S. L. Rolston, Phys. Rev. Lett. **83**, 4776 (1999).
[8] S. Kulin, T. C. Killian, S. D. Bergeson, and S. L. Rolston, Phys. Rev. Lett. **85**, 318 (2000).
[9] T. C. Killian, M. J. Lim, S. Kulin, R. Dumke, S. D. Bergeson, and S. L. Rolston, Phys. Rev. Lett. **86**, 3759 (2001).
[10] Y. C. Chen, C. E. Simien, S. Laha, P. Gupta, Y. N. Martinez, P. G. Mickelson, S. B. Nagel, and T. C. Killian, Phys. Rev. Lett. **93**, 265003 (2004).
[11] C. E. Simien, Y. C. Chen, P. Gupta, S. Laha, Y. N. Martinez, P. G. Mickelson, S. B. Nagel, and T. C. Killian, Phys. Rev. Lett. **92**, 143001 (2004).
[12] E. A. Cummings, J. E. Daily, D. S. Durfee, and S. D. Bergeson, Phys. Rev. Lett. **95**, 235001 (2005).
[13] S. G. Kuzmin and T. M. O'Neil, Phys. Rev. Lett. **88**, 065003 (2002).
[14] M. S. Murillo, J. Phys. A **42**, 214054 (2009).
[15] M. S. Murillo, Phys. Rev. Lett. **87**, 115003 (2001).
[16] M. Greiner, O. Mandel, T. Esslinger, T. W. Hansch, and I. Bloch, Nature (London) **415**, 39 (2002).
[17] T. Pohl, E. Demler, and M. D. Lukin, Phys. Rev. Lett. **104**, 043002 (2010).
[18] M. S. Murillo, Phys. Rev. Lett. **96**, 165001 (2006).
[19] S. Laha, Y. C. Chen, P. Gupta, C. E. Simien, Y. N. Martinez, P. G. Mickelson, S. B. Nagel, and T. C. Killian, Eur. Phys. J. D **40**, 51 (2006).
[20] J. Castro, P. McQuillen, H. Gao, and T. C. Killian, J. Phys. Conf. Ser. **194**, 012065 (2009).
[21] R. T. Farouki and S. Hamaguchi, J. Chem. Phys. **101**, 9885 (1994).
[22] S. Hamaguchi, R. T. Farouki, and D. H. E. Dubin, J. Chem. Phys. **105**, 7641 (1996).
[23] S. Hamaguchi, R. T. Farouki, and D. H. E. Dubin, Phys. Rev. E **56**, 4671 (1997).
[24] A. Denning, S. D. Bergeson, and F. Robicheaux, Phys. Rev. A **80**, 033415 (2009).
[25] P. Gupta, S. Laha, C. E. Simien, H. Gao, J. Castro, T. C. Killian, and T. Pohl, Phys. Rev. Lett. **99**, 075005 (2007).
[26] F. Robicheaux and J. D. Hanson, Phys. Rev. Lett. **88**, 055002 (2002).
[27] S. G. Kuzmin and T. M. O'Neil, Phys. Plasmas **9**, 3743 (2002).
[28] S. Mazevet, L. A. Collins, and J. D. Kress, Phys. Rev. Lett. **88**, 055001 (2002).
[29] H. Ohta and S. Hamaguchi, Phys. Rev. Lett. **84**, 6026 (2000).
[30] J. Castro, P. McQuillen, and T. C. Killian, Phys. Rev. Lett. **105**, 065004 (2010).

Bibliography

[1] J. H. Malmberg and J. S. deGrassie, "Properties of Nonneutral Plasma," Phys. Rev. Lett. **35,** 577–580 (1975).

[2] J. J. Bollinger and D. J. Wineland, "Strongly Coupled Nonneutral Ion Plasma," Phys. Rev. Lett. **53,** 348–351 (1984).

[3] *NRL Plasma Formulary* (Naval Research Laboratory, Washington, DC, 2011), p. 40.

[4] T. C. Killian, S. Kulin, S. D. Bergeson, L. A. Orozco, C. Orzel, and S. L. Rolston, "Creation of an Ultracold Neutral Plasma," Phys. Rev. Lett. **83,** 4776–4779 (1999).

[5] S. G. Kuzmin and T. M. O'Neil, "Numerical Simulation of Ultracold Plasmas: How Rapid Intrinsic Heating Limits the Development of Correlation," Phys. Rev. Lett. **88,** 065003 (2002).

[6] M. S. Murillo, "Using Fermi Statistics to Create Strongly Coupled Ion Plasmas in Atom Traps," Phys. Rev. Lett. **87,** 115003 (2001).

[7] C. E. Simien, Y. C. Chen, P. Gupta, S. Laha, Y. N. Martinez, P. G. Mickelson, S. B. Nagel, and T. C. Killian, "Using Absorption Imaging to Study Ion Dynamics in an Ultracold Neutral Plasma," Phys. Rev. Lett. **92,** 143001 (2004).

[8] E. A. Cummings, J. E. Daily, D. S. Durfee, and S. D. Bergeson, "Fluorescence measurements of expanding strongly coupled neutral plasmas," Phys. Rev. Lett. **95,** 235001 (2005).

[9] S. D. Bergeson, A. Denning, M. Lyon, and F. Robicheaux, "Density and temperature scaling of disorder-induced heating in ultracold plasmas," Phys. Rev. A **83,** 023409 (2011).

[10] M. Lyon and S. D. Bergeson, "The influence of electron screening on-induced heating," Journal of Physics B: Atomic, Molecular and Optical Physics **44,** 184014 (2011).

[11] T. C. Killian, M. J. Lim, S. Kulin, R. Dumke, S. D. Bergeson, and S. L. Rolston, "Formation of Rydberg Atoms in an Expanding Ultracold Neutral Plasma," Phys. Rev. Lett. **86,** 3759–3762 (2001).

[12] R. S. Fletcher, X. L. Zhang, and S. L. Rolston, "Using Three-Body Recombination to Extract Electron Temperatures of Ultracold Plasmas," Phys. Rev. Lett. **99,** 145001 (2007).

[13] S. D. Bergeson and F. Robicheaux, "Recombination Fluorescence in Ultracold Neutral Plasmas," Physical Review Letters **101,** 073202 (2008).

[14] J. Castro, P. McQuillen, and T. C. Killian, "Ion Acoustic Waves in Ultracold Neutral Plasmas," Phys. Rev. Lett. **105,** 065004 (2010).

[15] T. C. Killian, P. McQuillen, T. M. O'Neil, and J. Castro, "Creating and studying ion acoustic waves in ultracold neutral plasmasa)," Physics of Plasmas (1994-present) **19,** – (2012).

[16] S. Kulin, T. C. Killian, S. D. Bergeson, and S. L. Rolston, "Plasma Oscillations and Expansion of an Ultracold Neutral Plasma," Phys. Rev. Lett. **85,** 318–321 (2000).

[17] F. Robicheaux and J. D. Hanson, "Simulated expansion of an ultra-cold, neutral plasma," Phys. Plasmas **10,** 2217–2229 (2003).

[18] S. Laha, P. Gupta, C. E. Simien, H. Gao, J. Castro, T. Pohl, and T. C. Killian, "Experimental Realization of an Exact Solution to the Vlasov Equations for an Expanding Plasma," Physical Review Letters **99,** 155001 (2007).

[19] R. S. Fletcher, X. L. Zhang, and S. L. Rolston, "Observation of collective modes of ultracold plasmas," **96,** 105003 (2007).

[20] K. A. Twedt and S. L. Rolston, "Electronic Detection of Collective Modes of an Ultracold Plasma," Phys. Rev. Lett. **108,** 065003 (2012).

[21] T. Pohl, T. Pattard, and J. M. Rost, "Kinetic modeling and molecular dynamics simulation of ultracold neutral plasmas including ionic correlations," Phys. Rev. A **70,** 033416 (2004).

[22] Y. C. Chen, C. E. Simien, S. Laha, P. Gupta, Y. N. Martinez, P. G. Mickelson, S. B. Nagel, and T. C. Killian, "Electron Screening and Kinetic-Energy Oscillations in a Strongly Coupled Plasma," Phys. Rev. Lett. **93,** 265003 (2004).

[23] S. Laha, Y. C. Chen, P. Gupta, C. E. Simien, Y. N. Martinez, P. G. Mickelson, S. B. Nagel, and T. C. Killian, "Kinetic energy oscillations in annular regions of ultracold neutral plasmas," Eur. Phys. J. D pp. 51–56 (2006).

[24] H. M. Van Horn, "Dense Astrophysical Plasmas," Science **252,** 384–389 (1991).

[25] S. Ichimaru, "Strongly coupled plasmas: high-density classical plasmas and degenerate electron liquids," Rev. Mod. Phys. **54,** 1017–1059 (1982).

[26] M. S. Murillo, "Ultrafast phase-space dynamics of ultracold, neutral plasmas," Journal of Physics A: Mathematical and Theoretical **42,** 214054 (2009).

[27] M. Lyon, S. D. Bergeson, and M. S. Murillo, "Limit of strong ion coupling due to electron shielding," Phys. Rev. E **87,** 033101 (2013).

[28] S. L. Rolston, "Ultracold neutral plasmas," Physics **1,** 2–2–1 (2008).

[29] E. E. Salpeter, "Electrons Screening and Thermonuclear Reactions," Australian J. Phys. **7,** 353 (1954).

[30] E. E. Salpeter and H. M. V. Horn, "Nuclear Reaction Rates at High Densities," Astrophys. J. **155,** 183 (1969).

[31] M. J. Jensen, T. Hasegawa, J. J. Bollinger, and D. H. E. Dubin, "Rapid Heating of a Strongly Coupled Plasma near the Solid-Liquid Phase Transition," Phys. Rev. Lett. **94,** 025001 (2005).

[32] F. Anderegg, D. H. E. Dubin, T. M. O'Neil, and C. F. Driscoll, "Measurement of Correlation-Enhanced Collision Rates," Phys. Rev. Lett. **102,** 185001 (2009).

[33] M. E. Glinsky, T. M. O'Neil, M. N. Rosenbluth, K. Tsuruta, and S. Ichimaru, "Collisional equipartition rate for a magnetized pure electron plasma," Phys. Fluids B **4,** 1156–1166 (1992).

[34] D. H. E. Dubin, "Measurement of Screening Enhancement to Nuclear Reaction Rates using a Strongly Magnetized and Strongly Correlated Non-neutral Plasma," Phys. Rev. Lett. **94,** 025002 (2005).

[35] S. G. Kuzmin and T. M. O'Neil, "Numerical simulation of ultracold plasmas," Phys. Plasmas **9,** 3743–3751 (2002).

[36] F. Robicheaux and J. D. Hanson, "Simulation of the Expansion of an Ultracold Neutral Plasma," Phys. Rev. Lett. **88,** 055002 (2002).

[37] P. Gupta, S. Laha, C. E. Simien, H. Gao, J. Castro, T. C. Killian, and T. Pohl, "Electron-temperature evolution in expanding ultracold neutral plasmas," Phys. Rev. Lett. **99,** 075005 (2007).

[38] E. A. Cummings, M. S. Hicken, and S. D. Bergeson, "Demonstration of a 1-W injection-locked continuous-wave titanium:sapphire laser," Appl. Opt. **41,** 7583–7587 (2002).

[39] K. W. Holman, R. J. Jones, A. Marian, S. T. Cundiff, and J. Ye, "Intensity-related dynamics of femtosecond frequency combs," Opt. Lett. **28,** 851–853 (2003).

[40] T. Brabec, C. Spielmann, P. F. Curley, and F. Krausz, "Kerr lens mode locking," Opt. Lett. **17,** 1292–1294 (1992).

[41] U. Schünemann, H. Engler, R. Grimm, M. Weidemüller, and M. Zielonkowski, "Simple scheme for tunable frequency offset locking of two lasers," Review of Scientific Instruments **70,** 242–243 (1999).

[42] D. R. Walker, T. Udem, C. Gohle, B. Stein, and T. W. Hänsch, "Frequency dependence of the fixed point in a fluctuating frequency comb," Applied Physics B - Lasers and Optics **89,** 535–538 (2007).

[43] C. Degenhardt, T. Binnewies, G. Wilpers, U. Sterr, F. Riehle, C. Lisdat, and E. Tiemann, "Photoassociation spectroscopy of cold calcium atoms," Phys. Rev. A **67,** 043408 (2003).

[44] E. J. Salumbides, V. Maslinskas, I. M. Dildar, A. L. Wolf, E.-J. van Duijn, K. S. E. Eikema, and W. Ubachs, "High-precision frequency measurement of the 423-nm Ca i line," Phys. Rev. A **83,** 012502 (2011).

[45] M. S. Murillo, "Ultrafast Dynamics of Strongly Coupled Plasmas," Phys. Rev. Lett. **96,** 165001 (2006).

[46] S. Hamaguchi and R. T. Farouki, "Thermodynamics of strongly coupled Yukawa systems near the one component plasma limit. I. Derivation of the excess energy," The Journal of Chemical Physics 101 (1994).

[47] R. T. Farouki and S. Hamaguchi, "Thermodynamics of strongly-coupled Yukawa systems near the one-component-plasma limit. II. Molecular dynamics simulations," The Journal of Chemical Physics **101,** 9885–9893 (1994).

[48] S. Hamaguchi, R. T. Farouki, and D. H. E. Dubin, "Phase diagram of Yukawa systems near the one-component-plasma limit revisited," The Journal of Chemical Physics **105,** 7641–7647 (1996).

[49] S. Hamaguchi, R. T. Farouki, and D. H. E. Dubin, "Triple point of Yukawa systems," Phys. Rev. E **56,** 4671–4682 (1997).

[50] M. W. C. Dharma-wardana and M. S. Murillo, "Pair-distribution functions of two-temperature two-mass systems: Comparison of molecular dynamics, classical-map hypernetted chain, quantum Monte Carlo, and Kohn-Sham calculations for dense hydrogen," Phys. Rev. E **77,** 026401 (2008).

[51] P. Seuferling, J. Vogel, and C. Toepffer, "Correlations in a two-temperature plasma," Phys. Rev. A **40,** 323–329 (1989).

[52] M. S. Murillo, "Ultrafast dynamics of neutral, ultracold plasmas," Physics of Plasmas **14,** 055702 (2007).

[53] F. H. Stillinger and T. A. Weber, "Packing Structures and Transitions in Liquids and Solids," Science **225,** 984 (1984).

[54] A. Kramida, Yu. Ralchenko, J. Reader, and and NIST ASD Team, NIST Atomic Spectra Database (ver. 5.1), [Online]. Available: [redacted] [2014, May 30]. National Institute of Standards and Technology, Gaithersburg, MD., 2013.

[55] K. Mølmer, Y. Castin, and J. Dalibard, "Monte Carlo wave-function method in quantum optics," J. Opt. Soc. Am. B **10,** 524–538 (1993).